Characterization of the fluorescence protein FP635 for *in vivo* imaging and establishment of a murine multiple myeloma model for non-invasive imaging of disease progression and response to therapy

Charakterisierung des Fluoreszenzproteins FP635 für die *in vivo* Bildgebung und Etablierung eines Maus Modells für die nicht invasive Bildgebung des Krankheitsverlaufes und Ansprechen auf Therapien im Multiplen Myelom

Doctoral thesis for a doctoral degree

at the Graduate School of Life Sciences,

Julius-Maximilians-Universität Würzburg,

Section of Infection and Immunity

Submitted by

Simone Stefanie Riedel

from

Ulm, Germany

Würzburg, 2013

Submitted on:

Office stamp

## Members of the *Promotionskomitee*:

Chairperson:             Prof. Dr. Thomas Hünig

Primary Supervisor:       Dr. Andreas Beilhack

Supervisor (Second):      Prof. Dr. Hans-Martin Jäck

Supervisor (Third):       Prof. Dr. Thomas Müller

Supervisor (Fourth):      Prof. Dr. Hermann Einsele

Date of Public Defence:

Date of receipt of Certificates:

# Acknowledgement

# Table of Content

# List of Figures

# List of Tables

## Abstract

Optical *in vivo* imaging methods have advanced the fields of stem cell transplantation, graft-versus–host disease and graft-versus-tumor responses. Two well known optical methods, based on the transmission of light through the test animal are bioluminescence imaging (BLI) and fluorescence imaging FLI. Both methods allow whole body *in vivo* imaging of the same animal over an extended time span where the cell distribution and proliferation can be visualized. BLI has the advantages of producing almost no unspecific background signals and no necessity for external excitation light. Hence, BLI is a highly sensitive and reliable detection method. Yet, the BLI reporter luciferase is not applicable with common microscopy techniques, therefore abolishing this method for cellular resolution imaging. FLI in turn, presents the appealing possibility to use one fluorescent reporter for whole body imaging as well as cellular resolution applying microscopy techniques. Currently, there are still major limitations when working with fluorescently labeled cells within animals. The general autofluorescence of surrounding tissues results in high background signals. Additionally, the excitation light as well as the emitted fluorescence are attenuated by the surrounding tissue. The absorption of light occurs mainly due to melanin and hemoglobin in wavelengths up to 650 nm. Therefore, the wavelength range beyond 650 nm may allow sensitive optical imaging even in deep tissues. For this reason, significant efforts are undertaken to isolate or develop genetically enhanced fluorescent proteins (FP) in this spectral range. "Katushka" also called FP635 has an emission close to this favorable spectrum and is reported as one of the brightest far-red FPs. We tested FP635 as a sensitive single reporter for the detection of immunological processes from whole body to single cell imaging. Our results suggest that although FP635 ranges in a favorable wavelength the advantage in skin signal attenuation was not distinctive compared to eGFP and DsRed-Monomer. We found that it was not possible to sensitively detect FP635 transgenic splenocytes in the setting of graft-versus-host disease. Though, non-invasive detection of rather superficially growing FP635 tagged tumor cells was accomplished. Our experiments also clearly showed the superiority of BLI for whole body imaging over FLI. Currently, if whole body to single cell imaging is desired a "dual approach" should be considered. Spectrally distinguishable luciferases allow sensitive whole body multicolor imaging and the additional labeling with selected FPs facilitates microscopic single cell detection.

Based on these results we applied the superior BLI technique for the establishment of a pre-clinical multiple myeloma (MM) mouse model. MM is a B-cell disease, where malignant plasma cells clonally expand in the bone marrow (BM) of older people, causing significant morbidity and mortality. Chromosomal abnormalities, considered a hallmark of MM, are present in nearly all patients and may accumulate or change during disease progression. The diagnosis of MM is based on clinical symptoms, including the CRAB criteria: increased

serum **c**alcium levels, **r**enal insufficiency, **a**nemia, and **b**one lesions (osteolytic lesions or osteoporosis with compression fractures). Other clinical symptoms include hyperviscosity, amyloidosis, and recurrent bacterial infections. Additionally, patients commonly exhibit more than 30% clonal BM plasma cells and the presence of monoclonal protein is detected in serum and/or urine. With current standard therapies, MM remains incurable and patients diagnosed with MM between 2001 and 2007 had a 5-year relative survival rate of only 41%. Therefore, the development of new drugs or immune cell-based therapies is desirable and necessary. To this end we developed the MOPC-315 cell line based syngeneic MM mouse model. MOPC-315 cells were labeled with luciferase for *in vivo* detection by BLI. We validated the non-invasively obtained BLI data with histopathology, measurement of idiotype IgA serum levels and flow cytometry. All methods affirmed the reliability of the *in vivo* BLI data for this model. We found that this orthotopic MM model reflects several key features of the human disease. MOPC-315 cells homed efficiently to the BM compartment including subsequent proliferation. Additionally, cells disseminated to distant skeletal parts, leading to the typical multifocal MM growth. Osteolytic lesions and bone remodeling was also detected. We found evidence that the cell line had retained plasticity seen by dynamic receptor expression regulation in different compartments such as the BM and the spleen. We believe that interaction with surrounding cells and other outside stimuli induced the differential receptor expression. The cell line expresses receptors commonly found on human MM cells including programmed death 1 ligand (PD-L1) and CXC chemokine receptor 4 (CXCR4). Both receptors are targets for approved or phase I clinical trial drugs. We also showed that *in vivo* passaging through the BM compartment of MOPC-315 cells leads to exacerbation of disease progression and dissemination. *In vivo* passaged cells showed highly aggressive behavior evidenced by eventual extramedullary manifestation and fast disease recurrence after alkylating drug treatment, despite very good treatment response. Probably, *in vivo* BM selected cells represent the equivalent to human relapsed refractory or end stage MM. Unselected cells might rather reflect the early stage of human MM, evidenced by slower MOPC-315 cell proliferation and reduced dissemination *in vivo*. Yet, to prove this further experiments are needed, but this would clearly further enhance the versatility of this model for pre-clinical drug testing. As this MM mouse model is based on immunocompetent hosts it will be valuable to test drugs affecting the immune system, immune cell based therapies and graft-versus-myeloma experiments. Clear advantages over traditional models without imaging capability are the superior MM detection sensitivity and the spatiotemporal information on disease progression and localization. Therefore, this model will be highly useful for the evaluation of upcoming novel MM therapies.

## Zusammenfassung

Optische *in vivo* bildgebende Verfahren haben die Felder der Stammzelltransplantation, Graft-versus-Host Krankheit und Graft-versus-Tumor Reaktion vorangebracht. Zwei gut bekannte optische Methoden, die auf der transmission von Licht durch das Versuchtier basieren, sind die Biolumineszenz Bildgebung (BLI) und die Fluoreszenz Bildgebung (FLI). Beide Methoden erlauben die *in vivo* Ganzkörperbildgebung desselben Tieres über lange Zeit wärenddessen die Zellverteilung und Proliferation sichtbar gemacht werden kann. Vorteil der BLI ist, dass beinahe keine unspezifischen Hintergrundsignale erzeugt werden und keine Notwendigkeit für Anregungslicht besteht. Daher ist BLI eine hochsensitive und verlässliche Detektionsmethode. Jedoch erlaubt der BLI Reporter, die Luziferase, keine Anwendung mit gängigen Mikroskopieanwendungen und verhindert daher, dass diese Methode für die Bildgebung auf zellulärer Ebene genutzt werden kann. FLI wiederum bietet die attraktive Möglichkeit einen fluoreszenten Reporter sowohl für die Bildgebung des gesamten Körpers, als auch auf zellulärer Ebene durch die Anwendung von Mikroskopietechniken zu nutzen. Derzeit bestehen noch größere Einschränkungen bei der Arbeit mit fluoreszent markierten Zellen innerhalb eines Tieres. Die allgemeine Autofluoreszenz des umliegenden Gewebes führt zu hohen Hintergrundsignalen. Zusätzlich werden sowohl das Anregungslicht als auch die emittierte Fluoreszenz durch das umliegende Gewebe abgeschwächt. Die Absorption des Lichtes geschieht hauptsächlich durch Melanin und Hämoglobin in Wellenlängen bis zu 650 nm. Daher könnte der Wellenlängenbereich über 650 nm sensitive optische Bildgebung auch in tief liegendem Gewebe ermöglichen. Aus diesem Grund werden erhebliche Anstrenungen unternommen um Fluoreszenzproteine (FP) in diesem spektralen Bereich zu isolieren oder genetisch verbesserte zu entwickeln. „Katushka" auch FP635 genannt hat eine Emission, die nahe an diesem günstigen Spektrum liegt und wurde als eines der hellsten dunkelroten FPs beschrieben. Wir untersuchten FP635 für die Anwendung als sensitiver Einzelreporter für die Detektion immunologischer Prozesse von der Ganzkörper- bis zur Einzelzellbildgebung. Unsere Ergebnisse deuten darauf hin, dass obwhol sich FP635 in einem günstigen Wellenlängenbereich befindet, der Vorteil der Signalabschwächung durch Haut nicht ausgeprägt besser war im Vergleich zu eGFP und DsRed-Monomer. Wir fanden heraus, dass es nicht möglich war FP635 transgene Splenozyten während der Graft-versus-Host Krankheit sensitiv zu detektieren. Jedoch war es möglich eher oberflächlich wachsende FP635 markierte Tumorzellen nichtinvasiv zu detektieren. Unsere Experimente zeigten auch deutlich die Überlegenheit der BLI über die FLI für die Ganzkörperbildgebung. Gegenwärtig sollte ein „dualer Ansatz" in Betracht gezogen werden wenn Ganzkörper- und Einzelzellbildgebung erwünscht sind. Spektral unterscheidbare Luziferasen bieten sensitive mehrfarbige Ganzkörperbildgebung und eine zusätzliche Markierung mit ausgewählten FPs erlaubt die mikroskopische Einzelzelldetektion.

Basierend auf diesen Ergebnissen setzten wir die überlegene BLI für die Etablierung eines präklinischen Mausmodells des Multiplen Myeloms (MM) ein. MM ist eine B-Zell Erkrankung wobei maligne Plasmazellen klonal im Knochenmark (BM) älterer Menschen expandieren und erhebliche Morbidität und Sterblichkeit verursacht. Chromosomale Abnormitäten gelten als Kennzeichen des MM, sind bei beinahe allen Patienten vorhanden und können sich während des Krankheitsverlaufes anhäufen oder verändern. Die Diagnose des MM basiert auf klinischen Syptomen inklusive der folgenden Kriterien: erhöhte Serum Kalzium Konzentration, Niereninsuffizienz, Anämie und Knochenläsionen (osteolytische Läsionen oder Osteoporose mit Kompressionsfrakturen). Weitere klinische Symptome beinhalten Hyperviskosität, Amyloidose und wiederkehrende bakterielle Infektionen. Zusätzlich zeigen Patienten verbreitet mehr als 30% klonale BM Plasmazellen und monoklonales Protein ist in Serum und/oder Urin detektierbar. Mit derzeitigen Standardtherapien bleibt MM unheilbar und Patienten, die zwischen 2001 und 2007 mit MM diagnostiziert wurden hatten eine relative 5-jahres Überlebensrate von nur 41%. Daher ist die Entwicklung neuer Medikamente und immunzellbasierten Therapien wünschenswert und notwendig. Zu diesem Zweck entwickelten wir das auf der Zelllinie MOPC-315 basierende syngene MM Mausmodell. Die MOPC-315 Zellen wurden für die *in vivo* Detektion mittels BLI mit Luziferase markiert. Wir validierten die nichtinvasiv gewonnenen BLI Daten mit Histopathologie, der Messung des idiotypen IgA Spiegels im Serum und Durchflusszytometrie. Alle Methoden bekräftigten die Zuverlässigkeit *in vivo* BLI Daten für dieses Modell. Wir stellten fest, dass dieses orthotope MM Modell einige Hauptmerkmale der menschlichen Erkrankung widerspiegelt. Die MOPC-315 Zellen wanderten effizient in das BM Kompartiment inklusive darauffolgender Proliferation. Ausserdem, streuten die Zellen in entfernte Teile des Skeletts aus was zum typischen multifokalen MM Wachstum führte. Wir stellten auch osteolytische Läsionen und Knochenumbau fest. Wir fanden Hinweise darauf, dass sich die Zelllinie Plastizität bewahrte was durch die dynamische Regulation der Rezeptorexpression in verschiedenen Kompartimenten, wie dem BM und der Milz, sichtbar wurde. Wir vermuten, dass die Interaktion mit umgebenden Zellen und anderer äusserer Stimuli die unterschiedliche Rezeptorexpression herbeiführte. Die Zellline exprimiert Rezeptoren, die häufig aud menschlichen MM Zellen festgestellt werden, beispielsweise Programmierter Zelltod 1 Ligand (PD-L1) und CXC Chemokinrezeptor 4 (CXCR4). Beide Rezeptoren sind Ziele zugelassener oder in der klinischen Versuchsphase I befindlicher Medikamente. Wir zeigten auch, dass die *in vivo* Passage von MOPC-315 Zellen durch das BM Kompartiment zu einer Verschlimmerung des Krankheitsverlaufes und der Dissemination führt. *In vivo* passagierte Zellen zeigten ein hochaggressives Verhalten das bewiesen wurde durch die gelegentlich auftretende extramedulläre Manifestation und die schnelle Krankheitsrückkehr nach Behandlung mit alkylierenden Medikamenten, trotz sehr gutem Ansprechen auf die Behandlung. Möglicherweise stellen die *in vivo* BM selektionierten Zellen das Äquivalent zum

menschlichen rezidiven refraktären oder im Endstadium befindlichen MM dar. Nicht selektionierte Zellen könnten eher die frühe MM Phase des Menschen darstellen, was durch die langsamere MOPC-315 Zellproliferation und verminderte Dissemination *in vivo* bekräftigt wird. Um dies allerdings zu beweisen sind weitere Experimente notwendig. Jedoch würde dies klar die Vielseitigkeit dieses Modells für die präklinische Erprobung von Medikamenten erweitern. Da dieses MM Mausmodell auf immunkompetenten Tieren beruht wird es auch für die Erprobung von Medikamenten, die auf das Immunsystem wirken, immunzellbasierten Therapien und Graft-versus-Myelom Experimenten nützlich sein. Klare Vorteile gegenüber traditionellen Modellen ohne Möglichkeit der Bildgebung, sind die überlegene Detektionssensitivität und die räumliche als auch zeitliche Information über den Krankheitsverlauf und die Lokalisation. Daher wird dieses Modell für die Erprobung kommender neuer MM Therapien höchst nützlich sein.

# 1 <u>Introduction</u>

## 1.1 *In vivo* optical imaging

Biological and biomedical research has the goal to better understand the biological processes underlying diseases, advance treatment strategies and to understand the interaction of cells, proteins and molecules involved in disease onset and progression. All these events are highly dynamic and in order to gain temporal information, conventional experimental strategies demand repeated chronological sacrifice of test animals throughout the experiment. This approach can highly increase the number of test animals, especially if a tight temporal monitoring of disease development or response to therapy is necessary. At the same time this approach decreases statistical power because each animal is only measured once and cannot serve as its own control[1,2]. The variability of biological processes involved in disease progression and response to therapy which occurs between test animals must be compensated by a higher number of animals[2].

A solution to these experimental challenges provide non-invasive imaging methods which allow real-time *in vivo* display of biological processes within the test animal. These techniques offer the opportunity to closely follow processes over time within the same animal where initial time points can serve as internal control[1]. This allows a comprehensive analysis of each individual animal over time instead of just having a single snapshot of a specific animal at a specific endpoint and thereby greatly reducing animal numbers[1].

Imaging modalities such as positron emission tomography (PET), magnetic resonance imaging (MRI), single photon emission tomography (SPECT) and X-ray computed tomography (CT) have potential clinical use and are therefore very appealing for translational studies. However, MRI is generally less sensitive than PET or SPECT and radiotracers used for PET and SPECT often produce unspecific signals from kidney, liver and bladder[3]. Moreover, these modalities are often extremely expensive, difficult to accommodate and do not provide the possibility of high throughput for routine imaging of larger cohorts or several animals at the same time[2].

On the other hand there are optical methods that are based on the transmission of light through the test animal, such as *in vivo* bioluminescence imaging (BLI) and fluorescence imaging (FLI). Both methods offer unique advantages that turn them into invaluable techniques for *in vivo* experimentation: Image acquisition times are comparatively short which facilitates the analysis of larger animal cohorts. The range of image resolutions is variable and ranges from the microscopic to the macroscopic scale. Moreover, optical imaging is independent from ionizing radiation and offers a broad range of reporters, dyes and specific animal models[1,3]. Lastly, signal-to-noise ratios for BLI are excellent and enable highly sensitive non-invasive detection[4,5].

### 1.1.1 Bioluminescence imaging (BLI)

The principle of bioluminescence imaging (BLI) is derived from a natural phenomenon seen in lower organisms such as beetles, bacteria, algae, crustaceans, annelids, mollusks and coelenterates. Those organisms possess enzymes called luciferases which catalyze in the presence of a specific luciferin substrate and oxygen, the light-producing chemical reaction in the living organism **(Figure 1)**. Light is emitted during the relaxation of the excited oxyluciferin to its ground state and the emitted photons can be sensitively detected by a cooled charge-coupled device (CCD) camera[6]. As this process is based on enzymatic activity there is no need for external excitation light unlike in fluorescence imaging, thus lowering the background signal and enhancing the signal-to-background ratio[7]. Additionally, the near absence of endogenous light from mammalian cells and tissues further reduces background signals and further increases the detection sensibility[8].
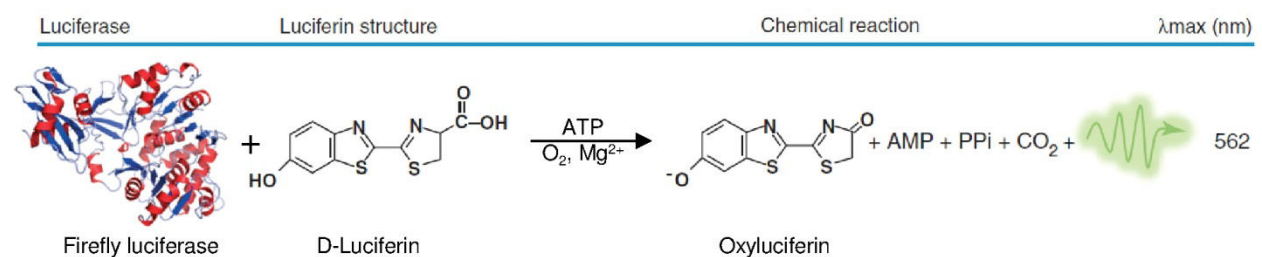


**Figure 1: Reaction of luciferase with luciferin resulting in light emission.** Shown is the firefly luciferase structure, the chemical structure of its reaction partner D-luciferin and the product oxyluciferin, and the peak light emission (adopted from[9,10]).

In biomedical research the firefly *Photinus pyralis* luciferase (Fluc), the sea pansy *Renilla reniformis* luciferase (Rluc) and the marine copepod *Gaussia princeps* luciferase (Gluc) are the most common reporters[9].

Gluc is not dependent on ATP and naturally secreted although engineered membrane bound forms exist and are in use. Therefore, Gluc can report from the cell itself as well as from blood or urine allowing highly sensitive *ex vivo* monitoring of biological processes *in vivo*[11–14]. Rluc exists membrane bound, is ATP independent and uses the same substrate as Gluc, the coelenterazine[15]. Rluc and Gluc both emit blue-green luminescence (peak emission 480 nm) within seconds after addition of the substrate[9,15]. Both, Fluc and Rluc are naturally cell-associated and need different substrates for luminescence which makes them the perfect candidates for combination as dual reporters for BLI. The substrate for Fluc, D-Luciferin, is usually injected intraperitoneally (i.p.), reaches the peak signal 10 min later and stays constant for 30 min[9]. Rluc needs coelenterazine as substrate, which is usually injected intravenously (i.v.), reaches the peak signal 10 s later and is vanished after 1 min[9,15]. These different kinetics allow a clear distinction between differently labeled cells in *vitro as* well as in

the same living animal. Moreover it has been shown that neither substrate reacts with the other luciferase[15,16]. To further enhance the signal intensity of Rluc and increase imaging sensitivity as primary reporter or in combination with Fluc a synthetic Rluc has been made[16]. Rluc and Gluc both produce a flash-type bioluminescence reaction[9] which means that animals need to be imaged seconds after injection. This could create difficulties if imaging of more than one animal at a time is desired or if the animal should be imaged from different angles requiring 2 or more exposures. Moreover, the short wavelength blue-green emission of Gluc and Rluc are not favorable for *in vivo* imaging. The primary absorbing molecules in tissues are hemoglobin and melanin which greatly absorb and scatter signals in wavelengths until 600 nm. Hence, the favorable imaging wavelengths are from 600 nm to 1100 nm where still scattering occurs but light is much more readily transmitted through tissues[1,5,17,18]. The broad emission spectrum of native Fluc includes a significant fraction above 600 nm (with peak emission at 562 nm)[9] making it the most commonly used gene for *in vivo* BLI [1,8]. Fluc was first reported in 1985[19] and since then has been improved for expression in mammalian cells by multiple genetic modifications[8,20]. These modifications include optimized mammalian codon usage and the removal of the peroxisome targeting site so Fluc can be highly expressed and localizes to the cytoplasm. There are also extensive efforts to change the emission spectrum of Fluc towards the red spectral region above 600 nm to further enhance the detection sensitivity[6,21–23]. Further advances have been made to combine Fluc with other luciferases in order to image two cell populations *in vivo* simultaneously. This has been accomplished by combining a green click beetle luciferase and a red-shifted Fluc. The emitted signals from both luciferases are separated by their spectral difference. As both luciferases offer similar reaction kinetics and use the same substrate the imaging procedure is greatly simplified[22].

Because of the mentioned advantages BLI has helped to gain new insights in all fields of biomedical research. It has been used to monitor processes in graft-versus-host disease (GVHD) and thus contributed to the elucidation of temporal and spatial dynamics of alloreactive T cells[24] and their activation pattern[25]. Moreover, BLI proofed as a useful tool to image early events of hematopoietic reconstitution[26], the bacterial burden of *Staphylococcus aureus* in chronic post-operative infections[27] as well as in models of parainfluenza virus infection[28]. Especially, cancer research has greatly benefited from the application of *in vivo* BLI by monitoring of tumor growth, metastasis[29] and immune cell based anti-tumor effects[30,31]. This has refined pre-clinical mouse models for the improvement of cancer treatment strategies including drug testing and immune therapies[10,32–34] because the treatment effects can be detected immediately in the anatomical context of the whole animal. Additionally, several studies have demonstrated the strong correlation between the non-

invasively detected BLI signal and the actual tumor load as specified by traditional methods as serum markers or histopathology[35,36].

A major drawback of BLI is the imaging limitation when approaching the microscopic scale as BLI signals cannot be detected with microscopic methods such as intravital laser scanning 2-photon microscopy (2PM) or confocal microscopy. To further enhance our understanding of biological processes it is not only important to detect cells in the anatomical context of the whole animal or organ but also to track processes on a cellular level. In order to achieve this broad spectrum of spatial scales, from whole body to the single cell, a different reporter and optical imaging modality is needed. This could be facilitated by using fluorescent proteins (FP) as reporters for 2PM cellular imaging as well as whole body fluorescence imaging (FLI) in the same animal which gives the exciting opportunity to visualize biological processes in various dimensions.

### 1.1.2  Fluorescence imaging (FLI)

The green fluorescent protein (GFP) was the first FP discovered and still remains the most prominent FP. GFP was isolated from the bioluminescent marine jellyfish *Aequorea victoria* and first cloned in 1992[37]. Since its first application for *in vivo* labeling to tag sensory neurons in the nematode[38] it became a unique tool for the visualization of structures and processes in living cells and organisms. Because GFP was so successful scientists became interested in the development of improved GFP versions that are brighter, cover a broad spectral range, exhibit high photostability and reduced oligomerization, are insensitive to pH and have fast maturation rates. The chromophore of original GFP was mutated and termed enhanced GFP (eGFP) which is 35 times brighter and additionally codon optimized for higher expression in mammalian cells[39]. Also modifications concerning the emission and excitation spectra were done resulting in variants emitting in the blue (blue fluorescent protein, BFP), cyan (cyan fluorescent protein, CFP) and yellow (yellow fluorescent protein, YFP) spectral regions[40–42]. Yet the orange, red and far-red regions of the spectrum were unachievable with GFP-like FPs and not unlocked until the discovery of the first red fluorescent protein (RFP) from a non-bioluminescent reef coral *Discosoma sp.* "red" also termed DsRed[43]. Because the obligate tetramerization, association of the tetramers into higher order aggregates and slow and incomplete maturation of the original DsRed[44] have hindered its use as a genetically encoded tag, further mutations were performed in order to create a stable monomeric RFP (mRFP1) with a red-shift of 25 nm. During this effort, important FP characteristics as extinction coefficient, fluorescence quantum yield and photostability decreased slightly[45]. Therefore, further mutagenesis approaches of DsRed variants were undertaken to increase FP characteristics and to broaden the spectral palette. Additionally, FPs from other animals

were isolated, such as the sea anemone *Entacmaea quadricolor*, and further mutated in order to red-shift the excitation and emission spectra and create preferentially bright stable monomers (m) or tandem dimers (td) **(Table 1,2)**.

**Table 1: DsRed and its most important mutated variants.**

DsRed[43] | DsRed.T1 (DsRed-Express)[47] | dimer2[45] | tdTomato[48] | mCherry, mOrange, mStrawberry[48] | mPlum[49] | mRFP1[45]

DsRed1, DsRed2[46]

DsRed.T3[47] | DsRed-MST[50]

DsRed.T4[47] | DsRed-M1 (DsRed-Monomer)[51]
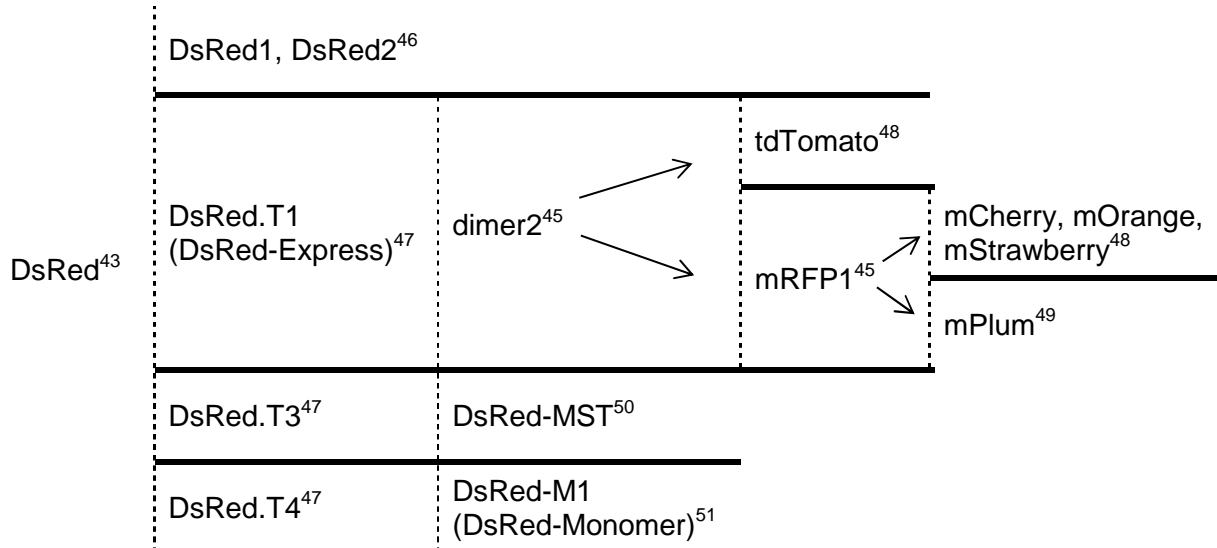
**Table 2: eqFP578 and its mutated variants.**

eqFP578[52] | TurboRFP[52] | TagRFP[52] | Katushka (FP635)[53] | mKate[53]
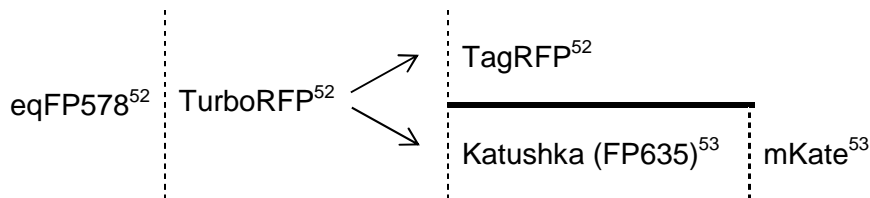
The recently developed FPs eqFP650, eqFP670[54], IFP1.4[55] and iRFP[56] even reach to the near-infrared spectrum.

**Table 3: Overview over important properties of selected fluorescent proteins.**

| Class | Protein | Ex (nm) | Em (nm) | Extinction Coefficient | Quantum Yield | Brightness (a.u.) | Oligomerization | Ref. |
|---|---|---|---|---|---|---|---|---|
| Near-infrared | iRFP | 690 | 713 | 85,000 | 0.059 | 5,015 | Dimer | 56,57 |
| | IFP1.4 | 684 | 708 | 54,700 | 0.077 | 4,212 | Monomer + Oligomers | 55,57 |
| | eqFP670 | 605 | 670 | 70,000 | 0.06 | 4,200 | Dimer | 54 |
| | eqFP650 | 592 | 650 | 65,000 | 0.24 | 15,600 | Dimer | 54 |
| Far-red | mPlum | 590 | 649 | 41,000 | 0.10 | 4,100 | Monomer | 49 |
| | FP635 | 588 | 635 | 65,000 | 0.34 | 22,100 | Dimer | 53 |
| | mKate | 588 | 635 | 45,000 | 0.33 | 14,850 | Monomer | 53 |
| Red | mCherry | 587 | 610 | 72,000 | 0.22 | 15,840 | Monomer | 48 |
| | DsRed-Monomer | 556 | 586 | 35,000 | 0.10 | 3,500 | Monomer | 51 |
| | tdTomato | 554 | 581 | 138,000 | 0.69 | 95,220 | Tandem Dimer | 48 |
| Green | eGFP | 488 | 507 | 56,000 | 0.60 | 33,600 | Weak Dimer | 58 |

All these efforts to shift FPs towards the red spectrum and to increase the intrinsic brightness are driven by several challenges that occur during fluorescence imaging. In wavelengths until 600 nm the tissue is comparatively opaque and the transmission of light is considerably scattered and absorbed, mainly from hemoglobin and melanin. Above 600 nm the so called "optical window" forms which is highly favorable for imaging in general[1,5,17,18] and has been already discussed for BLI in section 1.1.1 but for the detection of FPs wavelength-dependent factors play a more prominent role:

The detection of FPs in living cells relies upon the excitation of the fluorophore by external excitation light. This excitation light creates a considerable autofluorescence as it also unspecifically excites other cellular proteins or digested food within the gastrointestinal tract[5]. Therefore, FLI has to deal with a generally higher background than BLI. The specific emitted FP signal needs to be stronger than this background which decreases imaging sensitivity[4,7]. Especially in shorter wavelengths background fluorescence is a major challenge. Moreover, FLI has two sources of signal attenuation: 1) Excitation light: the absorption of the excitation light leads to limited tissue penetration. For this reason only FPs in a certain depth within the animal can be excited at all, others outside the excitation light remain dark. 2) Emission light: those FPs that were excited now emit light which is again absorbed and scattered on the way through the tissue.

FLI has been successfully applied in the context of GVHD to visualize eGFP tagged T cells homing into secondary lymphoid organs such as the spleen and Peyer's patches as well as their subsequent proliferation[59]. However, to perform *in vivo* imaging of internal organs for each imaging session mice were operated to expose the respective organs. Similarly, to visualize GVHD and the reaction to immunomodulatory reagents mice had to be opened for imaging of GFP tagged immune cells in the gastrointestinal tract and liver. Only superficial immune cells in the skin were non-invasively detectable on the ear pinna and a shaved skin area[60]. These surgical interventions clearly limit the number of imaging timepoints and can induce inflammatory artifacts in T cell migration especially in an inflammation affected model as GVHD.

Also for the detection of solid cancers and metastasis FLI proved to be useful. Dual color labeled human fibrosarcoma cells with eGFP tagged nuclei and RFP cytoplasm were used to investigate cancer metastasis after cyclophosphamide pretreatment of the recipient mice. Sensitive imaging was only possible on an opened skin flap which was closed after each imaging session[61]. Non-invasive cancer detection was shown to work with a model of RFP expressing colon cancer cells implanted into GFP expressing nude mice. The non-invasively imaged RFP cancer cells were growing on top of the colon tissue and formed large tumor aggregates, but in order to detect interactions between tumor and stroma, tissue had to be

excised[62]. Another model of RFP expressing orthotopic pancreas cancer allowed non-invasive imaging of the primary tumor and some metastases including infiltration into mesenteric lymph nodes (LN). Again, to detect tumor aggregates which are less superficial mice had to be opened[63]. Also, glioblastoma cells expressing mKate2 or mCherry were non-invasively imaged in the brain and it was proven that the measured signal intensity correlated with the actual tumor size[64]. FP635 expressing tumor cells were used in a subcutaneous model to monitor immunotoxin treatment, allowing sensitive non-invasive imaging because of the large and superficial tumor mass[65]. In mouse models using GFP expressing B16 melanoma and human colon cancer it was shown that a tumor aggregate of 59 µm diameter was detectable at a depth of 0.5 mm and in 0.6 mm depth the tumor diameter had to be at least 100 µm[66].

Besides the imaging of various tumor models FPs can also be used as markers for gene expression of vectors used for gene therapy. GFP expression induced by the injection of an adenoviral vector into the respective organ revealed detectable signals from brain, liver, pancreas, prostate and bone. Yet, the non-invasive imaging does not seem to be very sensitive[67]. Others have used a FP635 coding vector which was delivered into muscle and skin tissue by DNA electrotransfer with limited success in terms of sensitivity and expression duration[68,69].

Obviously, FLI of the whole animal or single organs is very appealing for biomedical research and the recent developments of red and far-red FPs has accelerated the use of fluorescently labeled tumor models. To add another spatial scale, cellular and subcellular resolution, microscopy techniques have to be applied.

### 1.1.3  Laser scanning 2-photon microscopy (2PM)

Traditional techniques such as fluorescence or confocal microscopy use linear absorption processes requiring one photon for the excitation of the FP. They are limited for usage near the tissue surface of generally less than 100 µm because deeper in the tissue strong and multiple light scattering blurs the images[70]. In contrast nonlinear microscopy uses two (or more) photons for the excitation of the FP. This technique offers special features that renders it less sensitive to scattering and therefore enable high resolution imaging in living tissues of up to one millimeter depth. The principle of 2PM are two long-wavelength photons that are simultaneously absorbed by an FP thus combining their energy and bringing the FP to its excited state[71,72]. This only happens in the tight light focus within the tissue which is generated by focusing a laser beam through a high numerical aperture objective thus avoiding out of focus signal generation[70] **(Figure 2)**. Because this technique can achieve better tissue penetration than conventional linear microscopy it is very appealing for *in vivo*

imaging. Therefore 2PM has been used to investigate processes in a variety of tissues such as lymphatic organs[73–77], kidney[78,79], heart[80,81], brain[82–84] and the eye[85] with intact tissues. Additionally, this technique is used to study the development, progression and treatment therapies of diseases such as cancer[86] and Alzheimer[82].

This powerful microscopy method in combination with whole body FLI allows the imaging of the whole spatial range from whole body to the single cell level and will advance the field of imaging studies in intact tissues as well as living animals.
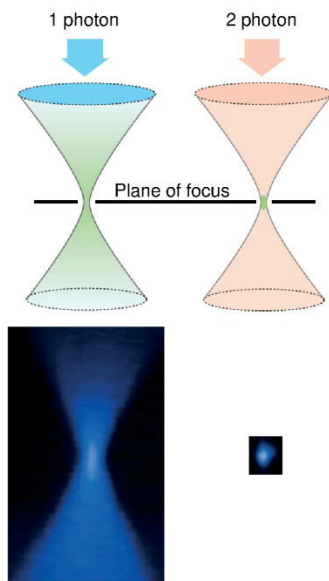


**Figure 2: Focal volume of linear 1 photon and non-linear 2 photon excitation.** For excitation short wavelength light in the visible spectrum (blue) is used for 1 photon microscopy whereas near-infrared (red) light is used in 2 photon microscopy. The whole illumination level is evoked (green) in 1 photon microscopy while the 2 photon excitation is spatially confined to a minute sub-femtoliter focal volume and only this focal spot is excited during imaging. Schematic view shown on top and actual view shown below (adapted from[70,85]).

## 1.2  Multiple Myeloma (MM)

### 1.2.1  Epidemiology and etiology

Multiple Myeloma (MM) is a B cell malignancy that causes significant morbidity and mortality worldwide. MM accounts for 1 % of all malignant tumors, among hematologic malignancies it comprises 10 -15 % and is the cause of 20 % of deaths related to cancers of the blood and bone marrow[87]. The disease mainly occurs in elderly people with a median age at diagnosis of 69 years (range 20 – 85+ years of age) in the US. 74,8 % of patients diagnosed with MM are between 55 and 84 years old[88]. In the US for 2012 it is estimated that 21,700 people are newly diagnosed with MM and 10,700 deaths as a result of the disease[89]. The age-adjusted incidence rate of MM per 100,000 is similar for White and Hispanic ethnicities with 6.9 and

6.3 (males) respective 4.1 and 4.7 (females). The incidence rate for Black US citizens is more than twice as high with 14.3 (males) and 10.1 (females) while in the Asian and American Indian / Alaska Native populations the incidence rate is only 4 – 5 (males) and 3 – 4 (females)[88]. If diagnosed in the US with MM between 2001 and 2007 the 5-year relative survival rate totals to 41 %[89]. In the European Union (EU) MM incidence number for 2008 was for males 16,400 and females 15,600 cases, this corresponds to an age standardized incidence rate of 5.4 for males and 3.9 for females per 100,000. The mortality added up to 10,400 for males and 10,500 for females corresponding to an age standardized mortality rate of 3.3 for males and 2.3 for females per 100,000[90]. The causes for the uneven racial and gender distribution of MM incidence are unknown so far.

### 1.2.2 Development and pathophysiology

MM is a B-cell neoplasia characterized by clonal expansion of malignant plasma cells in the bone marrow. Regular B cell differentiation occurs in early (antigen-independent) and late (antigen-dependent) stages, finally culminating in the generation of memory B cells and plasma cells (PC)[91,92]. During the antigen independent differentiation precursor B cells undergo VDJ rearrangement and mature into naïve, resting B cells that circulate in the blood and lymphoid tissues. After antigenic exposure with specificity for the immunoglobulin receptor combined with other signals, naïve B cells in the splenic marginal zone and circulating mature follicular B cells undergo proliferation and differentiation into low-affinity immunoglobulin M-secreting (IgM) PCs. These short lived PCs arising from the early extrafollicular response aggregate in germinal centers but have no somatically mutated immunoglobulin (Ig) genes yet. Antigen and antigen-specific T helper cells are necessary for those PCs to undergo proliferation, multiple rounds of somatic hypermutation of immunoglobulin heavy (IgH) and immunoglobulin light chain (IgL) V(D)J sequences as well as affinity maturation and class-switch recombination of Ig[93,94]. These processes finally produce memory B cells and terminally differentiated non-proliferating long-lived PCs producing high affinity IgG or IgA antibodies[95,96]. Classically such PCs home to the bone marrow (BM) compartment where they receive survival signals such as interleukin-6, produced by BM stromal cells, and reside there for several months to years[97]. MM and its precursor stages originate exclusively from post-germinal center B cells because the Ig sequences in MM PCs are somatically hypermutated and remain constant throughout the disease[98,99]. Chromosomal abnormalities are a hallmark of MM as they are present in nearly all MM patients[100]. It has been proposed that during early MM pathogenesis primary translocations occur while secondary translocations happen in the later stage of MM and are involved in disease progresssion[101]. Most primary Ig translocations are simple, reciprocal translocations that juxtapose an oncogene and one of the strong Ig enhancers. These

translocations result from errors in B-cell-specific DNA modification processes prevalently during IgH switch recombination, sometimes by somatic hypermutation during PC generation in germinal centers and seldom from VDJ recombination[98,100]. Translocations involving the IgH locus seem to be the most frequent genetic abnormality in MM[102] and are present in 50 - 60 % of tumors. Five recurrent primary translocations involving the IgH locus on chromosome 14q32 have been identified in 40 % of MM tumors resulting in the dysregulation of CYCLIN D1, CYCLIN D3, FGFR3/MMSET, c-MAF or MAFB[103]. Patients lacking IgH translocations show hyperdiploidy as the hallmark of their disease[100]. In contrast, secondary translocations are mediated by unknown processes as in PCs and PC tumors the B-cell-specific DNA modification mechanisms are inactive. The paradigm of secondary translocations is the dysregulation of c-MYC which is a late progression event associated with enhanced MM proliferation and probably found in more than 90 % of MM. Mostly, complex translocations juxtapose c-MYC to an Ig enhancer but about one third of MYC translocations seem to lack Ig enhancer sequences. This strongly suggests that also non-Ig regulatory elements are able to dysregulate MYC in MM[98,100,103]. Other secondary IgH translocations not involving MYC are found in approximately 20 % of MM cases[100] and the poorly characterized chromosomal partners seem to be non-recurrent or rare that can occur at any time during MM tumorigenesis[103].

MM never evolves *de novo* but is consistently preceded by a pre-malignant asymptomatic stage called monoclonal gammopathy of undetermined significance (MGUS)[104]. The diagnostic criteria for MGUS are a serum monoclonal protein level below 3 g/dl with clonal BM PCs less than 10 % and the absence of clinical symptoms[96]. MGUS is prevalent in over 4 % of the general population over 50 years of age with a risk of around 1 % per year for progression to MM with clinical symptoms[105]. The diagnosis for MM is based on clinical symptoms including the CRAB criteria: increased serum **c**alcium levels, **r**enal insufficiency, **a**nemia and **b**one lesions (osteolytic lesions or osteoporosis with compression fractures). Further clinical symptoms include hyperviscosity, amyloidosis and recurrent bacterial infections. Additionally, patients commonly show more than 30 % clonal BM PCs and monoclonal protein is detected in serum and/or urine[100,106].

Between MGUS and the development of active MM an intermediate entity called smoldering myeloma (SMM) is defined which is rather heterogeneous and was mainly created for clinical purposes[107,108]. SMM is defined by a serum monoclonal protein level above 3 g/dl and clonal BM PCs more than 10 % including the absence of clinical symptoms. Yet it is important to distinguish SMM from the also asymptomatic MGUS as SMM patients are at higher risk of progression to MM. The risk is 10 % per year for the first 5 years after diagnosis, decreasing to 3 % annually for the following 5 years, and then reaching 1 % as MGUS[109].

Little is known about the driving forces leading from the pre-malignant stages MGUS and SMM to active MM but obviously with progression of the disease the proportion of specific genetic abnormalities in clonal PCs is markedly enhanced[94,110]. So far, several intrinsic properties such as MYC abnormalities, RAS mutations or p53 mutations seem to distinguish active MM from its premalignant asymptomatic stages[100]. Activating RAS mutations, for example, have been found in 35 – 50 % of MM patients but appear to be with 12.5 % rare in MGUS. This suggests that this might be a molecular marker or even causative in the progression from MGUS to MM in those cases[100,111] **(Figure 3)**.

Currently, MGUS and SMM are not treated but a conservative "watch and wait" strategy is applied until active MM with clinical manifestations is diagnosed. The main reasons for this strategy are that until recently MM treatment options have been limited, toxic and no benefit was demonstrated for overall survival for early therapy in randomized trials[108,109].
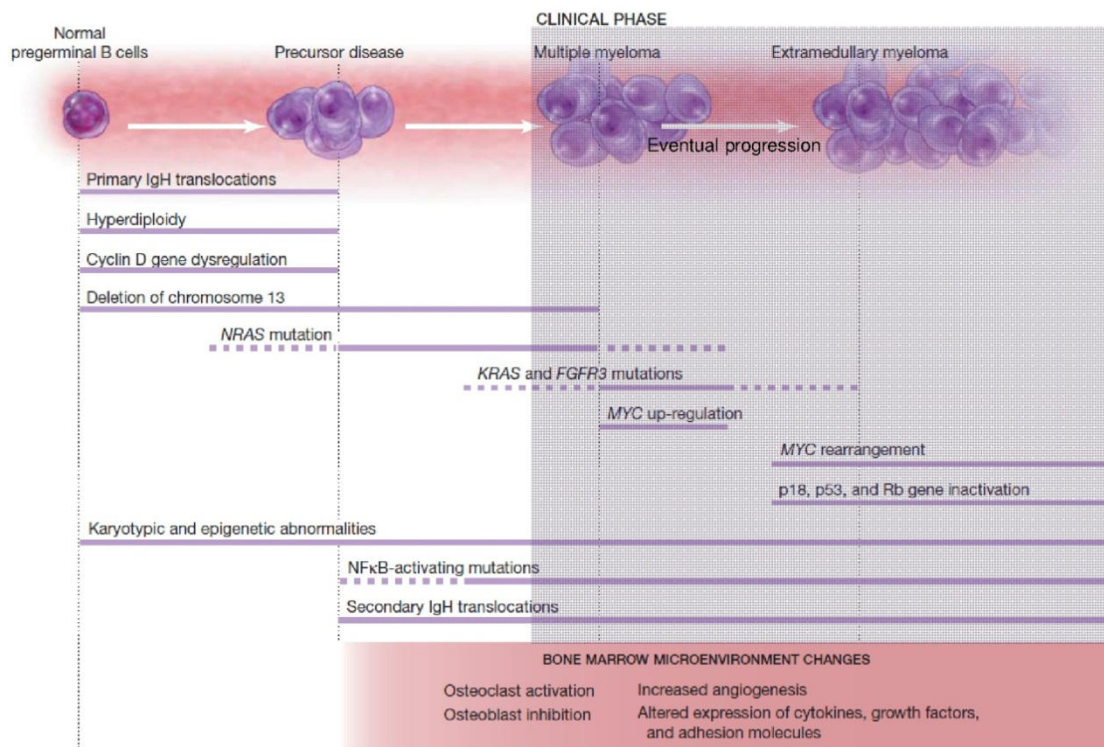


**Figure 3: Stages of the progression in multiple myeloma and several important associated biological events.** Several oncogenic events which do not all occur in each patient lead to the clonal post-germinal center B cell which always first evolves to the MM precursor disease monoclonal gammopathy of undetermined significance (MGUS) which is still clinically asymptomatic. MGUS can either progress to another asymptomatic precursor disease, smoldering myeloma, or directly evolve to active myeloma which is identified by appearing clinical symptoms. Obviously certain genetic abnormalities occur only in the later stage of multiple myeloma progression. Eventually multiple myeloma can progress to extramedullary sites. Solid lines indicate the period during which the respective event is likely to occur, dashed lines indicate less certainty in the timing (adapted from[109]).

### 1.2.3 Treatment strategies

**Alkylating agents, corticosteroids, and conventional chemotherapeutic agents**

In the 1940s the systematic study of agents for the therapy of MM started with reports on the use of urethane, an ethyl carbamate, suggesting a clinical benefit for patients treated with this agent[112,113]. Yet, a controlled clinical trial comparing urethane to placebo in MM diagnosed patients showed no significant improvement of any parameter indicative for MM, questioning the anti-MM effect of urethane[114]. During the 1960s alkylating agents such as melphalan and cyclophosphamide were applied for MM treatment. Those drugs inhibit cell growth by intercalating the DNA double strand helix resulting in double and single strand breaks especially in proliferating cells. Both drugs, melphalan and cyclophosphamide, were reported to have anti MM effects when administered as a single-agent[115–118]. During this time also prednisone, a corticosteroid, and several years later dexamethasone, were reported to have single-agent activity[119,120]. After the idea of combining drugs to improve treatment effects was introduced in cancer therapy, this concept was also adopted for MM therapy during the late 1960s[121]. In a pivotal study by Alexanian and colleagues compared melphalan alone to melphalan combined with prednisone (MP), where MP proved to be superior to melphalan alone. The combination therapy was associated with MM remission in approximately 40% of patients with a 2-year median duration of remission, additionally, a six-month improvement in overall survival (OS) was reported[122]. This led to the establishment of MP as a standard of care in MM treatment, remaining it for decades[96]. Efforts were undertaken to enhance the efficacy of MP with the addition of other chemotherapeutic drugs such as taxanes or anthracyclines leading to more intensive combination regimens. Typical combinations were vincristine, carmustine, melphalan, cyclophosphamide and prednisone (VBMCP)[123] or carmustine, melphalan, cyclophosphamide, and prednisone (BMCP)[124], later followed by vincristine, doxorubicin, and dexamethasone (VAD)[125]. For transplant-eligible patients with newly diagnosed MM VAD became a favored induction regimen because this combination was beneficial for the survival of stem cells. These newly introduced combinations such as VBMCP, BMCP, or VAD caused higher response rates than MP, yet neither remission nor OS were decisively prolonged[121,126].

**Stem cell transplantation**

For many years the standard of care for MM was the usage of conventional agents with stem cell transplantation applied only to selected patients. In 1983 McElwain and Powles reported for the first time the usage of a high-dose therapy using melphalan for the treatment of MM in 8 patients[127]. They reported a correlation of melphalan dosage with the magnitude of response of MM to the treatment but the high-dose melphalan led to severe neutropenia between 23 up to 56 days and multiple infections. These findings led to another study where

high-dose therapy was combined with autologous stem cell transplantation (ASCT) to avoid long periods of neutropenia[128]. Patients with MM refractory to multiple prior treatments were treated with high-dose melphalan followed by autologous bone marrow infusion which led to a prevention of serious infections in 6 out of 7 patients and no death due to bone marrow aplasia. Moreover this study showed the possibility to overcome MM drug resistance by dose escalation[128]. The promising results of high-dose therapy followed by ASCT in relapsed patients raised interest whether this therapy would be applicable in newly diagnosed MM as well. In 1996 a randomized clinical trial by the Intergroupe Français du Myélome with previously untreated MM patients compared the treatment outcome of either conventional therapy only vs high-dose therapy followed by ASCT[129]. This study showed for the first time that high-dose therapy + ASCT led to a higher response rate (81% vs 57%) including higher complete responses (22% vs 5%), better event-free survival for 5 years (28% vs 10%) and a better rate of survival for 5 years (52% vs 12%). Treatment related mortalities were similar with 3% in both regimens and a subsequent study from the UK[130] confirmed these findings.

Despite the beneficial treatment outcomes of ASCT, patients ultimately relapse, supposedly due to a combination of residual MM clones after high-dose therapy and contaminating MM cells within the BM infusion[121]. To avoid these complications after ASCT and prolong the remission duration and OS, tandem ASCT[131] or ASCT followed by a maintenance therapy with prednisone and interferon have been found beneficial[132]. Barlogie and colleagues have introduced a very intensive treatment concept named "Total Therapy 3" which consists of induction chemotherapy followed by tandem ASCT and maintenance with novel agents[133]. This treatment regimen provides comparably good response rates including a 2-year survival of more than 80% of patients yet the toxicity of this intense regimen remains challenging.

Besides ASCT also allogeneic stem cell transplantation could be considered to treat MM because of the advantage of MM load reduction by induction therapy including the unique graft-versus-myeloma effect. The allogeneic transplant setting seems to be associated with a tendency for better long-term survival and progression-free survival for patients alive 1 year after allo-transplant[134]. Nevertheless, a fully myeloablative high-dose chemoradiotherapy followed by allogeneic transplantation shows a transplant related mortality of up to 50% within the first 180 days strongly diminishing the possible benefits thus leading to reduced-intensity conditioning regimens[134,135]. The idea was to reduce toxicity while at the same time preserving the beneficial graft-versus-myeloma effect. Nevertheless, ASCT or tandem ASCT is still the preferred treatment regimen recommended by European experts for newly diagnosed eligible patients[136]. Several clinical trials failed to demonstrate significant advantages of nonmyeloablative allogeneic transplantation for OS or progression-free survival and is instead associated with severe graft-versus-host disease and high

transplantation related mortality[137–139]. Allogeneic stem cell transplantation in MM stays, outside clinical trials, therefore restricted to younger patients with HLA-identical siblings[121].

## Novel agents

The more recent introduction of novel agents such as the immunomodulatory drugs (IMiDs) thalidomide and its analogue lenalidomide and the proteasome inhibitor bortezomib have led to a clear improvement in survival of MM patients[106,140]. The incorporation of these novel agents into combination therapies for front-line therapy as well as in the treatment of relapsed patients is currently standard of care[136].

Thalidomide belongs to the class of IMiDs and inhibits TNF-α production as well as angiogenesis by the blockade of basic fibroblast growth factor and VEGF[141]. Moreover, *in vitro* studies showed a promoting effect on the adaptive and innate immune system. This effect seems to originate from the co-stimulation of T cells and an augmentation of NK and NKT cells[142]. Especially the antiangiogenic properties led to the consideration of the use for MM treatment as MM is associated with an increased level of VEGF and neovascularization in the BM[143]. Thereupon Barlogie and colleagues conducted a trial with patients of advanced and refractory MM treating them with single-agent thalidomide[144]. In 37% of patients a 25% myeloma protein reduction was obtained, the two-year event-free survival was 20% and the overall survival rates 48% proving that thalidomide was the first new drug with single-agent activity for over 3 decades. A 10 year follow up on the study reported from initially 169 enrolled patients, 17 alive and 10 are still event free[145]. Other studies using thalidomide in combination with conventional agents for the frontline treatment of newly diagnosed MM proved the beneficial effect of thalidomide and reported a response rate of 64%[146] and 72% including complete remission in 16%[147] of the patients. Thalidomide was also proven to overcome drug resistance to conventional agents in MM cells *in vitro*[148] as well as in a clinical trial[149]. The study included patients resistant to dexamethasone-based regimens (77%) and patients who had previously been treated with high-dose therapy (32%) where 55% achieved a partial response[149]. In search of thalidomide analogues with increased potency but less toxic side-effects the Celgene Corporation generated lenalidomide by adding an amino group to the phthaloyl ring of thalidomide[142]. Lenalidomide has proven its efficacy in several clinical trials[150,151] and is currently in routine use of MM treatment[136].

Another novel drug is bortezomib belonging to the class of peptide boronate proteasome inhibitors inhibiting the 26S proteasome activity. The ubiquitin-proteasome pathway is responsible for the breakdown of a large variety of cellular proteins and is thus essential for many cellular regulatory mechanisms. The pathway degrades cyclins and inhibitors of cyclin-dependent kinases which controls cell-cycle progression[152]. Indeed, bortezomib exerts marked antitumor activity and growth delays in several tumor models[153]. The ubiquitin-

proteasome pathway also degrades IKB which is the inhibitor of the transcription factor NF-KB[152]. It has been shown that NF-KB activation is responsible for drug resistance in MM cells and additionally regulates the expression of adhesion molecules on MM cells as well as on BM stromal cells thus regulating the interaction between both cell types. It also regulates the constitutive as well as the MM cell adhesion-induced cytokine transcription and secretion in BM stromal cells[152,154]. Because bortezomib blocks the degradation of IKB, NF-KB cannot translocate into the nucleus and therefore stays inactive. Indeed, *in vitro* studies on MM cell lines and primary human MM cells showed induction of apoptosis in drug resistant MM cells as well as downregulation of adhesion molecules on MM cells and BM stromal cells, the blockade of NF-KB-dependent cytokine secretion and inhibition of angiogenesis. Moreover, the inhibition of IL-6, on which MM cells depend, as well as a decline of MM cell proliferation has been reported[154]. The advantage of bortezomib treatment was also verified by an *in vivo* study using a MM mouse model which showed inhibition of MM growth associated with a prolonged survival of treated mice[155]. Based on these observations bortezomib became highly interesting for the clinical use to treat MM patients. An initial phase I clinical trial in patients with refractory hematologic malignancies, bortezomib showed significant activity against refractory MM[156]. A phase II trial followed, where of 193 patients 92% had been heavily treated previously and 91% were refractory to the last received therapy[157]. Patients were treated with bortezomib only except for patients with suboptimal response who were given additional dexamethasone. The rate of response to bortezomib was 35% (67 patients) including 19 patients with complete or near-complete response. For 12 patients among this group the response to bortezomib was superior to any response of previous treatments. Also drug-related side effects such as gastrointestinal toxicity and fatigue were largely manageable and other serious adverse events were uncommon[157]. Based on these promising results and a rather low toxicity of bortezomib in the patients it was also evaluated for use in newly diagnosed patients where an overall response rate across all dose levels of 77% with a 10% complete remission rate was reported[158]. Further studies for possible combinations of bortezomib with other novel or conventional agents for newly diagnosed as well as previously treated patients have been conducted consolidating the positive benefits of this drug for the therapy of MM[159]. Due to the success of bortezomib and the now recognized important role of proteasome inhibition for MM treatment, second-generation proteasome inhibitors, such as carfilzomib, marizomib or MLN9708, are currently under investigation in clinical trials[159].

**Emerging therapies**

To improve treatment of MM patients and an increased understanding of MM development and progression new drugs are under development. MM cells rely on the interaction with extracellular matrix proteins and BM stromal cells as well as other components of the BM

microenvironment. These factors are crucial for MM growth and survival, influence the migration of MM cells and can confer drug resistance. Therefore, novel agents have been targeted to interrupt or block these interactions as well as to specifically target the MM cell itself [160]. This includes, heat shock protein (HSP) 90 inhibitors, histone deacetylase (HDAC) inhibitors, farnesyl transferase inhibitors, several drugs targeting crucial surface molecules on MM cells, such as CD138 or VEGFR, and drugs targeting intracellular MM pathways, such as MEK/ERK, Jak2/STAT3 or PI3K/Akt, are currently under pre-clinical investigation or already in phase I clinical trials[160–162].

Despite all efforts and the variety of currently available drugs and treatment regimens, MM still remains incurable. This clearly demonstrates the urgent need for further drug development.

## 1.3 <u>Multiple myeloma mouse models</u>

To advance the development of new agents with anti-myeloma activity, pre-clinical testing and screening of possible candidates is very important and heavily relies on suitable mouse models. To date different MM mouse models are available that are based on subcutaneous xenografts, primary human MM cells, human cell lines, mouse cell lines or spontaneously developing MM mice.

The SCID-hu xenograft model relies on the subcutaneous implantation of fragments from human fetal femurs or tibias in immunodeficient mice[163]. Due to the immunocompromised host these bone fragments engraft and provide a human BM environment within the mouse. It was shown that this environment is favorable for primary human MM cells if injected directly into the bone graft[164]. This model is especially suited for the investigation of interactions between human MM cells and a human BM microenvironment. Because implantation of human fetal bones is ethically rather challenging and the question whether the fetal BM environment is really an adequate, "normal" environment for the primary MM cells the model was modified[165]. The human fetal bone was replaced by bones from 3-4 week old rabbits and the model called SCID-rab. The rabbit bone was chosen as rabbits are phylogenetically closer to primates than rodents[165]. It was shown that the created BM microenvironment allowed the growth of primary human MM cells exclusively inside the graft. Additionally, the MM cells were able to disseminate into another distantly implanted bone and MM cells from patients with extramedullary disease grew on the outer surface of the graft[165]. Despite the appealing possibility to study primary MM cells within a human-like BM environment these models rely on the measurement of human Ig levels to determine the tumor load. Additionally, the MM dissemination is only detectable by endpoint analysis and the graft setup is time consuming with 6-8 weeks until bone engraftment[165].

Another, similar approach avoids the usage of animal or human derived bones for implantation but relies on a scaffold-based technology to create a humanized bone environment in RAG-/-γc-/- mice[166]. The humanized environment was created with hybrid scaffolds consisting of three 2-3 mm biphasic calcium phosphate particles that were loaded with human mesenchymal stem cells (MSCs) and implanted s.c. into mice. The MSCs possess bone forming capacity and provide an environment similar to human BM which was demonstrated with the engraftment of human umbilical cord blood derived CD34^{+} as well as patient MM cells. Additionally, the authors showed that these primary MM cells can be labeled with luciferase before injection, therefore allowing the non-invasive detection of MM cell outgrowth. Nevertheless the model is again very time consuming with 8 weeks for proper bone formation on the scaffold[166] and the transduction of primary human MM cells might be not 100% which will lead to underestimation of MM growth upon BLI imaging.

These models might be very appealing, as they mimic the human BM environment and allow the outgrowth of MM cells directly derived from the patient. The drawback of these models is clearly the setup of the xenograft, which is rather laborious or ethically problematic. Additionally, they require a long time period of 6-8 weeks before MM cells can be injected, patient samples are only in limited numbers available and each patient sample contains MM cells with different properties.

Other MM mouse models use human MM cell lines that are injected into either RAG-/-γc-/-[167] or NOD/SCID[168] mice. Both mouse strains are immunocompromised, which allow engraftment of the human cell lines. In both cases mice are sublethally irradiated before MM cell injection and NOD/SCID mice are additionally CD122^{+} cell depleted to allow potent MM cell engraftment[168]. The usage of a MM cell line gives the opportunity to label the cells for non-invasive detection with subsequent sorting or limited dilution to achieve 100% labeled cells which is only hardly possible with primary MM cells due to their short survival under culture conditions. Non-invasive BLI of several human MM cell lines proved superior over the measurement of serum paraprotein[167] which is one of the few non endpoint analyses of tumor burden if cells are not labeled. This highlights the advantages of in this case, luciferase labeled MM cells for determining tumor growth and location.

The described models rely on immunocompromised hosts, which impairs the possibility to study effects of immune system-MM-drug interactions. Such interactions can be investigated when using syngeneic murine MM cell lines or spontaneously occurring MM models. In terms of murine MM cell lines, the 5TMM cell lines including further sub-cell lines are widely used. It was found that 0.5% of aging C57BL/KaLwRijHsd mice spontaneously develop a disease resembling MM. It was shown that these idiotypic paraprotein secreting cells did not grow *in vitro* but could be propagated by injection of the respective BM into younger healthy mice of

the same strain[169]. This model was described to resemble the human disease in several aspects such as the spontaneous occurrence, age related frequency of the disease, osteolytic lesions and detection of paraprotein[170]. The most extensively characterized cell lines for *in vivo* propagation are the 5T2MM and 5T3MM lines, where 5T2MM is described as the model representing the most common form of human MM including moderate growth and osteolytic lesions. The 5T33MM instead is highly aggressive with rapid tumor growth and additional liver involvement[171,172]. A subclone from the 5T33MM line, called 5TGM1, is also adapted for *in vitro* propagation. These 5TMM cells have been widely used to investigate for example the interaction between MM cells and the BM microenvironment[173,174], to better understand the selective initial BM homing *in vivo*[175], to block homing receptors and test novel treatment strategies[176–178], and to investigate the role of cancer stem cells[179]. The 5TGM1 cell line also has been applied for fluorescence imaging by GFP labeling yet with limited detection sensitivity regarding non-invasive imaging[180,181]. Despite these *in vivo* imaging approaches the main readout for tumor burden in these models remains the detection of paraprotein in the serum and histology[182]. However, these parameters are either determined after sacrificing the mice or do not offer information about tumor localization.

Another cell line based approach for a murine MM model is the MOPC-315 cell line which was established in 1968 by repeated injection of mineral oil into a BALB/c mouse[183]. This cell line has proven to be useful in studying immune-cell–tumor cell interaction or drug testing in mainly ectopic subcutaneous models[184–188] but also the intravenous usage[189,190] is reported. The readout for subcutaneous models is the measurable tumor size and for intravenous models a so called spleen colony assay was applied which relies on counting clonogenic colonies on spleens.

A different approach for MM mouse models are transgenic mice that spontaneously develop B-cell malignancies. Those models resemble the clinical situation in humans as they develop in aging mice, the disease progression is slow, typical clinical features such as osteolytic lesions occur and the disease is induced by typical translocations also found in humans. Several models have been established such as Vk∗MYC[191–193], Eμ-Xbp1[194], NPM-ALK[195], Eμ-Bcl2[196], Bcl-XL[197,198], iMyc/IL6[199], Eμ-v-abl/myc[200], IgH 3' LCR-Myc[201,202], Eμ-Ccnd1T286A[203], and iMycCα/Bcl-XL double TG mice[204,205]. In these models the disease onset for the individual animal is variable and the disease progression differs, additionally, in many models the exact disease subtype is unpredictable and needs to be verified for each mouse. Concerning the disease subtype, the Vk∗MYC model might be advantageous as the AID-dependent MYC activation in germinal center B cells allows 100% of the aging mice to develop MGUS with later progression to MM[191]. Therefore, this model was used for a large scale study on the efficacy of different drugs on MM growth including a comparison of the murine data with actual clinical data[192]. This study also showed the major drawbacks of those

spontaneous MM models. In order to provide the more than 200 mice for drug treatment huge breeding efforts were undertaken and all animals needed M-protein screening to detect the onset of their disease. In general, such mouse models only allow the determination of tumor load by the measurement of the secreted Ig which does not provide information on MM location or dissemination. Recently, this was addressed with the generation of the iGFP[5'Myc] mouse which is based on the Igh-Myc translocation upon which eGFP is expressed in malignant cells[206] but so far *in vivo* detection has not been demonstrated.

# 2 Questions and Specific Aims

*In vivo* imaging methods offer the appealing possibility to investigate the fate of different cell populations within the living organism. Thereby they provide real-time information about cell localization, trafficking and proliferation over extended periods. Therefore, these techniques are especially appealing for the investigation of dynamic processes such as immune responses or tumor growth and metastasis. The effect of interventions and manipulations during these events can be monitored immediately. BLI benefits from the practical absence of unspecific background resulting in high detection sensitivity. Yet the currently rather manageable color palette of available luciferases hampers the simultaneous imaging of different cell populations within the same animal. This shortcoming could be expanded by the application of fluorescent reporters with their steadily growing color palette. The addition of FLI to pre-existing and well established BLI models would greatly enhance their versatility. Multicolor imaging could greatly enhance our knowledge about the complex interplay between different immune cell populations of immune cell – tumor cell interactions. So far, non-invasive FLI suffers from considerable signal absorption. In addition with a high autofluorescent background the imaging sensitivity is rather low. The shift of FP excitation and emission towards the far-red or even infrared spectrum could overcome the current limitations. The application of non-invasive imaging modalities in MM mouse models would be valuable. The *in vivo* readout of effects by novel drug compounds would benefit as well as the evaluation of immune cell based therapies.

Therefore, we first investigated the applicability of the far-red fluorescent protein FP635 "Katushka" for *in vivo* imaging:

- Is FP635 a good candidate for whole body as well as single cell imaging?
- Are FP635 transgenic (tg) immune or tumor cells detectable *in vivo* and might be used concomitantly to luciferase tg immune cells?
- How is the detection sensitivity of FP635 in whole body FLI in comparison to BLI?

Finally, we applied our findings to the establishment of a murine MM model for non-invasive imaging of disease progression and response to therapy:

- Are obtained *in vivo* BLI data validated by other methods?
- Reflects the model typical features of human MM?
- Has the used cell line retained a certain plasticity and interacts with surrounding host cells
- How are the effects of clinically approved drugs on disease progression and is it comparable to clinical data?
- Is the model valid for reliable pre-clinical drug testing?

# 3   Material and Methods

## 3.1   Plasmids

### 3.1.1   Plasmids expressing fluorescent proteins and firefly luciferase

**FUGW:** Expresses the enhanced green fluorescent protein (eGFP) under the ubiquitin promoter (Addgene plasmid 14883)[207].

**FUGLW:** Expresses eGFP and firefly luciferase (luc) under the ubiquitin promoter. The vector uses the FUGW backbone where eGFP was replaced by the eGFP/luc fusion construct cloned from pJW.GFP-yLuc and ligated into FUGW via Pst I and Bam HI. pJW.GFP-yLuc was a kind gift from Dr. Michael H. Bachmann, Stanford University School of Medicine, Stanford, CA.

**pLVX-DsRed-Monomer-C1:** Expresses DsRed-Monomer under the human cytomegalovirus immediate early promoter ($P_{CMV\ IE}$) (Clontech – Takara Bio Europe, Saint-Germain-en-Laye, France)

**pTurboFP635-C:** Expresses FP635 "Katushka" under the $P_{CMV\ IE}$ promoter (Evrogen, Moscow, Russia).

**FUKW:** Expresses FP635 under the ubiquitin promoter. The vector is based on FUGW, where eGFP was replaced by FP635 from pTurboFP635-C. The vector was a kind gift from Marco Herold, Institute of Virology and Immunobiology, Würzburg University, currently at The Walter and Eliza Hall Institute of Medical Research, Molecular Genetics of Cancer, Australia.

### 3.1.2   3rd generation lentiviral packaging plasmids

**pRSV-Rev:** Expresses Rev cDNA where the joined second and third exons of HIV-1 rev are under the RSV U3 promoter (Addgene plasmid 12253)[208].

**pMDLg/pRRE:** The plasmid codes for the virion main structural proteins (gag) and pol which is responsible for retrovirus-specific enzymes. It also includes RRE, the binding site for the Rev protein responsible for RNA export from the nucleus (Addgene plasmid 12251)[208].

**pMD2.G:** This plasmid defines the virus envelope which is vesicular stomatitis virus (VSV) which shows high stability and broad tropism of its G protein (Addgene plasmid 12259).

### 3.1.3   Plasmid amplification and purification

Plasmids were amplified by transformation into TOP10 *Escherichia coli* (E. coli) (Invitrogen, Darmstadt, Germany) as follows: E. coli were thawed on ice, between 10 – 100 ng of the respective plasmid was gently added and mixed by stirring with the pipette tip. After 20 min

incubation on ice a 60 sec heat shock at 37°C in a water bath was performed. Then, quickly 250 µl sterile LB- Lennox medium (Carl Roth, Karlsruhe, Germany) was added and bacteria were incubated for 40 min, 37°C and 1200 rpm. Varying volumes of the cell suspension were plated onto LB-Lennox agar plates (Carl Roth, Karlsruhe, Germany) containing 100 µg / ml ampicillin (Sigma-Aldrich, Munich, Germany) and incubated overnight at 37 °C. On the next day single colonies were picked with a sterile pipette tip, 300 – 400 ml liquid LB-Lennox medium containing 100 µg / ml ampicillin was inoculated and incubated overnight at 37 °C, 1200 rpm.

The plasmids from the resulting bacteria suspension were purified using the Plasmid Maxi Kit (Qiagen, Hilden, Germany) following the manufacturer's instructions. Purified plasmids were dissolved in 250 – 300 µl DNAse/RNAse free water (Applichem, Darmstadt, Germany). Plasmid purity and concentration was determined on a NanoDrop UV-Vis Spectrophotometer (Thermo Fisher Scientific, Waltham, MA, USA) reporting high DNA purity without RNA or protein contamination. To check for genomic DNA contamination and verify plasmid identity restriction enzyme digestion was performed. 1 µg of the freshly purified plasmid and 1 µg already verified plasmid were simultaneously digested with appropriate enzymes and loaded onto a 1 – 1.5 % agarose-gel for electrophoresis. Plasmids were stored at -20 or -80 °C.

## 3.2   Cell culture

### 3.2.1   Cell lines

**293FT** cells (Life Technologies Invitrogen, Darmstadt, Germany) are human embryonic kidney cells transformed with the SV40 large T antigen.

**Mouse ovarian surface epithelial cells** (MOSEC) were a kind gift of Katherine F. Roby from the University of Kansas Medical Center.

**MOSEC FP635+:** MOSEC wildtype (wt) cells were lentiviral transduced using the FUKW vector. Resulting cells stably express FP635.

**MOPC-315.BM luc+:** The MOPC-315 mineral oil-induced plasmacytoma[183] was obtained as an in vitro-adapted cell line from ATCC (Manassa, VA, USA). The MOPC-315.4 cells were derived by repetitous subcutaneous (s.c.) injection in BALB/c mice. Subsequently, *in vivo* growing tumors cells were selected for enhanced tumor growth upon s.c. injection[209]. $2 \times 10^6$ MOPC-315.4 cells were injected i.v. into BALB/c mice. Tumor cells flushed from femurs of paraplegic mice were cultured *in vitro* and re-injected i.v. After 9 such *in vivo/in vitro* cycles a cell line with bone marrow tropism, MOPC-315.BM, was obtained. MOPC 315.BM cells were co-transfected with the pGL3-Control plasmid, which contains the firefly luciferase gene

(Promega), and the pcDNA 3.1 plasmid, which contains the gene for neomycin resistance (Invitrogen). Transfected cells were cloned by limiting dilution, resulting in the MOPC-315.BM luc[+] cell line[210,211].

**MOPC-315 FUGLW:** MOPC-315 cells were obtained from ATCC (Manassa, VA, USA) and lentiviral transduced as described with the FUGLW vector. Successfully transduced cells express eGFP and firefly luciferase and are subsequently called MOPC-315 FUGLW. Cells were FACS sorted twice on a FACSVantage (BD Biosciences, Franklin Lakes, NJ, USA) to obtain a homogenously eGFP expressing cell line. Firefly luciferase expression was confirmed by *in vitro* titration of sorted MOPC-315 FUGLW cells into 96 well plates and the subsequent measurement of emitted photons by bioluminescence imaging. Additionally, cells were *in vivo* passaged for selection of bone marrow homing cells. Therefore cells were injected i.v. into syngeneic BALB/c mice and tumor growth was monitored by BLI. The femur of a mouse with strong BLI signal was flushed and obtained cells re-injected i.v. After 4 repetitions the resulting cells were designated MOPC-315 FUGLW BMP4.

### 3.2.2 Culture conditions and cell culture media

293FT, all MOSEC and MOPC-315.BM luc^{+} cells were maintained in Dulbecco's modified Eagle's medium (DMEM) supplemented with 10% fetal bovine serum, 1% penicillin and streptomycin, 1% L-glutamine, 1:1000 β-Mercaptoethanol (25 µM) (Life Technologies Gibco, Darmstadt, Germany) and were grown at 37°C and 5% $CO_2$.

MOPC-315 and all MOPC-315 FUGLW variants were maintained in RPMI-1640 medium supplemented with 10% fetal bovine serum, 1% penicillin and streptomycin, 1% L-glutamine, 1:1000 β-Mercaptoethanol (25 µM) (Life Technologies Gibco, Darmstadt, Germany) and were grown at 37°C and 5% $CO_2$.

Fetal bovine serum used for cell culture was heat inactivated for 60 min at 56 °C.

Supplemented DMEM or RPMI media were subsequently called cDMEM or cRPMI.

### 3.3 Transient transfection of 293FT cells

293FT cells were transiently transfected with expression plasmids using the calcium-phosphate ($CaPO_4$) method[212].

$1x10^6$ cells were seeded in cDMEM into 10 cm culture dishes (Corning Inc., Corning, NY, USA) and grown for 24 h in the incubator. Simultaneously, cDMEM containing 25 mM HEPES (Carl Roth, Karlsruhe, Germany) was equilibrated overnight in the incubator. After 24 h 293FT cells were 40 – 50 % confluent and cDMEM was gently replaced by 10 ml equilibrated cDMEM +HEPES and left in the incubator for 4 h. Then 20 µg expression vector

was brought with sterile aqua dest. to 250 µl in a 15 ml plastic tube (Greiner Bio-One, Germany) and 250 µl 0.5 M $CaCl_2$ (Applichem, Darmstadt, Germany) was added. Then, 500 µl 2x HeBS (0.28 M NaCl, 0.05 M HEPES, 1.5 mM $Na_2HPO_4$ in aqua dest. with pH 7.0) was added in drops of 50 µl using a multistepper pipette while the mixture was vortexed. After 15 - 20 min incubation at room temperature 1 ml was added per cell culture dish and slightly swung to achieve thorough distribution. After 6 h the medium was changed with 12 ml cDMEM and cells harvested 45 – 50 h thereafter.

### 3.4  Stable transduction of cell lines

For lentivirus production to stably transduce cell lines a $3^{rd}$ generation system was used[213,214]. Here, lentiviral particles are produced by co-transfecting the expression vector with three helper vectors into the packaging cell line using the $CaPO_4$ method[212].

Therefore, $2.5 \times 10^6$ 293FT cells were seeded in 10 cm cell culture dishes (Corning Inc., Corning, NY, USA) and grown for 24 h in the incubator. Simultaneously, cDMEM containing 25 mM HEPES (Carl Roth, Karlsruhe, Germany) was equilibrated overnight in the incubator.

After 24 h 293FT cells were 70 – 80 % confluent and cDMEM was gently replaced by 10 ml equilibrated cDMEM +HEPES and left in the incubator for 4 h. Then 20 µg expression vector, 10 µg pMDLg/pRRE, 6 µg pMD2.G and 5 µg pRSV-Rev were brought with sterile aqua dest. to 250 µl in a 15 ml plastic tube (Greiner Bio-One, Germany) and 250 µl 0.5 M $CaCl_2$ (Applichem, Darmstadt, Germany) was added. Then, 500 µl 2x HeBS (0.28 M NaCl, 0.05 M HEPES, 1.5 mM $Na_2HPO_4$ in aqua dest. with pH 7.0) was added in drops of 50 µl using a multistepper pipette while the mixture was vortexed. After 15 - 20 min incubation at room temperature, 1 ml was added per cell culture dish and slightly swung to achieve thorough distribution and 6 – 8 h later medium was changed with 6 ml cDMEM.

48 h later the virus containing supernatant was harvested and passed through a 0.45 µm filter. Cells to be transduced were seeded in 6 well plates, medium removed and instead 3 -4 ml virus supernatant was added in presence of 8 µg / ml Polybrene (Hexadimethrine bromide, Sigma-Aldrich, Munich, Germany) and placed overnight in the incubator. Then the virus containing medium was replaced by the respective medium suitable for the cell line.

## 3.5 <u>Mice</u>

### 3.5.1 Commercially available mice

**C57BL/6J (B6):** Wild type mouse, black coat color, H-2$^b$ haplotype.

**B6.Cg-Tg(CAG-DsRed*MST)1Nagy/J (B6.DsRed)[50]:** Express DsRed-MST constitutively under the CAG promoter, black coat color, H-2$^b$ haplotype.

**B6.129S7-Rag1$^{tm1Mom}$/J[215]:** Homozygous mice produce no mature T cells or B cells, black coat color, H-2$^b$ haplotype.

**CByJ.Cg-*Foxn1$^{nu}$*/J (nude mouse)[216]:** Homozygous mice are athymic, consequently mice lack mature T cells and show a partial defect in B cell development, hairless and without pigmentation, H-2$^d$ haplotype.

**NOD.Cg-Prkdc$^{scid}$ Il2rg$^{tm1Wjl}$/SzJ[217]:** Also known as NOD severe combined immunodeficiency syndrome, common gamma chain deficient (NSG) mouse. Mice are deficient in mature T and B cells, serum Ig is not detectable and natural killer (NK) cell cytotoxic activity is extremely low. Albino (white) coat color, H-2$^{g7}$ haplotype.

**BALB/c:** Wild type mouse, albino (white) coat color, H-2$^d$ haplotype.

Mice were purchased from Jackson Laboratories (Bar Harbor, ME, USA), Charles River (Sulzfeld, Germany) or Harlan (Rossdorf, Germany) or bred in the ZEMM mouse facility.

For all multiple myeloma experiments female BALB/c mice 8 – 10 weeks old were used.

### 3.5.2 Non-commercial transgenic mice
**B6.FP635**

Transgenic mice expressing FP635 under the ubiquitin promoter in the genetic C57BL/6 background were generated as follows: (generation of mice was done by/with Marco Herold)

For lentiviral production, HEK-293T cells were transiently transfected with 10 µg FUKW vector DNA and the three helper plasmids (5 µg pMDLg/pRRE, 2.5 µg pRSV-Rev and 3 µg pMD2.G) by standard CaPO$_4$ method as described above. 48 h later viral supernatant was harvested, passed through a 0.45 µm filter and concentrated by ultracentrifugation in a swinging bucket for 90 min at 83000 g. The viral precipitate was resuspended in 20 – 30 µl of PBS / 0.1 % BSA and titrated by serial dilutions on HeLa cells. Average viral titers were around 3 – 6 x10$^8$ IU/ml. Subsequently, 10 pico liter of the FUKW lentivirus were injected into the perivitilline space of fertilized single cell stage oocytes obtained from superovulated C57BL/6J female mice[207]. The injected zygotes were cultured overnight and embryos at the two-cell stage were transferred into the oviduct of pseudopregnant CD1 outbred females the

next morning. Transgenic mice were selected upon FLI of new borns and measured signal intensities of leukocyte populations by flow cytometry in the PerCP-Cy5.5 channel.

**B6.Luc**

C57BL/6 L2G85 mice were generated by backcrossing FVB/N-L2G85 luciferase transgenic mice to the C57BL/6J background for more than 14 generations[26,218].

**B6.eGFP-Luc**

To generate luciferase transgenic and eGFP transgenic mice, C57BL/6 L2G85 mice at generation 12 were intercrossed with eGFP transgenic C57BL/6-Tg(ACTbEGFP)Osb/J mice. Subsequently these mice (designated C57BL/6 L2G85.eGFP) were bred with C57BL/6 L2G85 mice. As eGFP in the C57BL/6 L2G85.eGFP line is lethal if homozygous, mice were maintained at hemizygosity for eGFP. C57BL/6 L2G85.eGFP mice hemizygous for eGFP and homozygous for luciferase were used for imaging experiments.

**B6.DsRed-Luc**

C57BL/6 L2G85 were bred with B6.Cg-Tg(CAG-DsRed*MST)1Nagy/J resulting in B6.DsRed-Luc mice. Homozygous mice were used for the experiments.

Animal protocols were approved by the Institutional Animal Care and Use Committee at Stanford University and Würzburg University.

### 3.6 Laser scanning 2-photon microscopy (2PM)

A laser scanning multi-photon microscope with a single and multifocal scan head (TrimScope, Lavision Biotec, Bielefeld, Germany) was used as previously described[219] and additionally equipped with an optical parametric oscillator (OPO; APE, Berlin, Germany) necessary to reach excitation wavelengths of 1100 nm and beyond. Excitation wavelength for DsRed and FP635 was 1100 nm using a 605/70 filter for emission detection and 930 nm for eGFP using a 535/50 filter.

### 3.7 Photobleaching experiments

eGFP, DsRed-Monomer and FP635 transfected living 293FT cells were used for MPM photobleaching experiments. For this purpose laser output power on living 293FT cells was adjusted to 100 mW for all measurements. The scan frequency was set to 800 Hz and at a format of 512x512 pixels, acquiring 1 image per second. After 900 sec the bleaching series

were ended. Obtained timeseries were analyzed using Volocity 5 (PerkinElmer, Waltham, MA, USA) and Prism 5 (GraphPad, La Jolla, CA, USA).

## 3.8 Imaging of mice and cells

### 3.8.1 Fluorescence imaging (FLI)

FLI of mice, organs and cells was done on two different systems, in either case mice were anesthetized prior to imaging with a mixture of Ketamine (100 mg/kg) and Xylocaine (10 mg/kg) in PBS, i.p..

Maestro imaging system (CRi, Woburn, MA, USA): eGFP was detected with the blue filter set (excitation range 435-480 nm, emission filter 490 nm longpass), DsRed with the green filter set (excitation range 503-548 nm, emission filter 560 nm longpass) and FP635 with the yellow filter set (excitation range 576-621 nm, emission filter 635 nm longpass).

IVIS spectrum (Caliper-Xenogen, Alameda, CA, USA): FP635 was detected with 570 nm excitation and 640 nm emission filters.

To determine the absorption rate of skin for different FPs, $2.5 \times 10^6$ eGFP, DsRed-Monomer or FP635 transfected 293FT cells were seeded into 96 well plates. Signal intensities of uncovered cells were measured using the Maestro imaging system. Then, wells were covered with skin from either BALB/c pinnae (melanin poor) or C57BL/6 (melanin rich) pinnae and signal intensities were measured again.

For *in vivo* detection $1 \times 10^6$ MOSEC cells (FP635 or wt) were injected i.p. into female NSG recipients in a volume of 1ml PBS. For regular FLI as indicated, the peritoneal area was shaved and mice were fed with alfalfa-free rodent food to minimize background autofluorescence.

### 3.8.2 Bioluminescence imaging (BLI)

BLI of mice and cells was performed on an IVIS spectrum (Caliper-Xenogen, Alameda, CA, USA) as previously described[26]. Mice were anesthetized prior imaging as described in the FLI section, additionally 150 mg/kg D-luciferin (Biosynth, Staad, Switzerland) was coinjected and exactly 10 minutes after luciferin injection BLI measurements were started.

### 3.8.3 Data analysis

Resulting data was analyzed using Maestro 2.8.0 (CRi, Woburn, MA, USA) or Living Image 4.0 (Caliper-Xenogen, Alameda, CA, USA) and Prism 5 (GraphPad, La Jolla, CA, USA).

### 3.9 Induction of acute graft-versus-host disease and reconstitution

To induce aGVHD, CByJ.Cg-*Foxn1*$^{nu}$/J (H-2$^d$) nude mice were selected as recipients due to their albino and hairless phenotype which would provide greater sensitivity in the following FLI and BLI measurements. Recipient mice were lethally irradiated with 8 Gy followed by intravenous injection of 5x10$^6$ C57BL/6J WT (H-2$^b$) bone marrow cells and 2x10$^7$ whole splenocytes. Splenocytes were either from B6.DsRed, B6.DsRed-Luc or B6.FP635 (all H-2$^b$) donor mice.

B6.129S7-Rag1$^{tm1Mom}$/J (H-2$^b$) mice were syngeneic reconstituted by intravenous injection with either 5x10$^6$ eGFP B cells and 5x10$^6$ DsRed MST T cells or 5x10$^6$ eGFP B cells and 5x10$^6$ FP635 T cells (H-2$^b$). B cells were purified with MACS streptavidin beads, T cells with MACS CD4 and CD8 beads (Miltenyi Biotec GmbH, Bergisch Gladbach, Germany) according to manufacturer's instructions. Reconstituted mice were monitored once a week for engraftment of the transferred cells. For this reason mice were bled and PBMCs analyzed by flow cytometry. After 7 weeks mice were sacrificed and spleens used for 2PM.

### 3.10 Organ preparation

#### 3.10.1 Isolation of whole splenocytes

Anesthetized mice were sacrificed by cervical dislocation, the spleen removed and harvested in PBS (PAN-Biotech GmbH, Aidenbach, Germany). The spleen was cut on a prewetted 70 μm cell strainer (BD Biosciences, Bedford, MA, USA) and squeezed through using a syringe plunger. The sieve was washed with 10 ml lysis buffer and incubated for 2 min at room temperature to lyse erythrocytes. After addition of 10 ml PBS cells were centrifuged for 5 min at 1200 rpm, supernatant removed until 3 ml and passed through a second cell strainer to remove cell aggregates resulting, in a single cell suspension of whole splenocytes.

#### 3.10.2 Isolation of bone marrow cells

Anesthetized mice were sacrificed by cervical dislocation and hind legs (femur and tibia) were removed in undamaged condition to avoid contamination of the bone marrow. Femur and tibia were exposed and cut open on both sides using a sterile blade. The bone marrow was flushed with PBS using an Omnifix Duo 100 syringe (Braun, Melsungen, Germany) and subsequently passed through a 70 μm cell strainer to receive a single cell suspension.

### 3.11 Flow cytometry

### 3.11.1 Antibodies and detection

Primary mouse antibodies

**Table 4: Primary mouse antibodies used for flow cytometry detection.**

| Antigen | Clone | Conjugate | Isotype | Company |
|---------|-------|-----------|---------|---------|
| CD3ε | 145-2C11 | FITC | Armenian Hamster IgG | Biolegend |
| CD4 | GK1.5 | FITC | Rat IgG2b, κ | Biolegend |
| CD4 | RM4-5 | PE | Rat IgG2a, κ | Biolegend |
| CD4 | GK1.5 | APC-Cy7 | Rat IgG2b, κ | Biolegend |
| CD8α | 53-6.7 | FITC | Rat IgG2a, κ | Biolegend |
| CD8α | 53-6.7 | APC | Rat IgG2a, κ | Biolegend |
| CD19 | 6D5 | APC | Rat IgG2a, κ | Biolegend |
| CD44 | IM7 | PE | Rat IgG2b, κ | Biolegend |
| CD45R (B220) | RA3-6B2 | Biotin | Rat IgG2a, κ | Biolegend |
| CD49d (α4 integrin) | R1-2 | Alexa647 | Rat IgG2b, κ | Biolegend |
| CD62L | MEL-14 | APC-Cy7 | Rat IgG2a, κ | Biolegend |
| CD138 | 281-2 | Biotin | Rat IgG2a, κ | BD Pharmingen |
| CD183 (CXCR3) | CXCR3-173 | APC | Armenian Hamster IgG | Biolegend |
| CD184 (CXCR4) | 2B11 | PE | Rat IgG2b, κ | eBioscience |
| CD184 (CXCR4) | 2B11 | APC | Rat IgG2b, κ | eBioscience |
| CD192 (CCR2) | 475301 | APC | Rat IgG2b | R&D Systems |
| CD197 (CCR7) | 4B12 | APC | Rat IgG2a, κ | Biolegend |
| CD274 (PD-L1) | 10F.9G2 | APC | Rat IgG2b, κ | Biolegend |
| α4β7 (LPAM-1) | DATK32 | PE | Rat IgG2a, κ | Biolegend |

To detect biotinylated antibodies streptavidin Alexa647, Alexa750 (Invitrogen, Darmstadt, Germany) or eFluor 450 (eBioscience) was used and dead cells were excluded by propidium iodide staining.

All primary antibodies and secondary detection reagents were carefully titrated to avoid overstaining of cells.

Cells expressing eGFP were detected in the FITC channel and DsRed in the PE channel. FP635 was detected in the PerCP-Cy5.5 channel which is not ideal in terms of excitation and emission but still results in the best signal compared to the other detection channels.

Cells were measured on a FACS Canto II (BD, Heidelberg, Germany).

### 3.11.2 Fluorescence-activated cell sorting

To sort for CXCR4$^{high}$ and CXCR4$^{low}$ expressing MOPC-315.BM luc$^{+}$ cells, we stained the cells with CXCR4 APC (2B11). Sorting for the lowest 10 % and highest 10 % was performed on a FACS Aria III (BD, Heidelberg, Germany). Subsequently, 5x10$^5$ CXCR4$^{high}$ or CXCR4$^{low}$ sorted MOPC-315.BM luc$^{+}$ cells were injected i.v. into female BALB/c mice. After 10 days, mice were imaged with BLI, sacrificed, and spleen and femur/tibia marrow cells were extracted for FACS analysis to determine CXCR4$^{high}$ and CXCR4$^{low}$ expression. Additionally, cells from each sorted fraction of CXCR4$^{low}$ and CXCR4$^{high}$ cells were maintained in culture for 2 days, and then reanalyzed for CXCR4 expression with the same CXCR4 antibody that was used for cell sorting.

### 3.11.3 Data analysis

Analysis was done using FlowJo software (Tree Star, Ashland, OR, USA).

For all FACS analyses a compensation[220] matrix was applied. This is necessary as not all colors can be perfectly separated and spectrally close colors can leak into each other. This color overspill into other detection channels can lead to distorted positive-populations during analysis. Therefore, for each color measured during the experiment one sample was acquired where only this single color was stained. This sample contained a positive and a negative population as for each color one positive and one negative gate needed to be set. With these values FlowJo calculated the specific overspill of each color into other detection channels and corrected it.

Gates for positive populations were set according to the fluorescence minus one (FMO) method[220]. This method required a sample with all stainings except for the antibody to be analyzed. In this sample the gate was set in a way that almost 100% of the cells in the respective color channel belonged to the negative population. This gate was then applied to the sample where a complete staining with all antibodies was done.

To identify MOPC-315 cells we gated on CD138$^{+}$CD4$^{+}$ double positive cells. Within this gate the percentage of cells expressing the homing receptors or the fold change in mean fluorescence intensity (MFI) relative to the unstained sample was determined. The MFI was determined for surface markers on MM cells that displayed a gradual change in expression.

To distinguish α4β1$^{+}$ and α4β7$^{+}$ MOPC-315.BM luc$^{+}$ cells gates for the homing receptors α4β7 and α4 were set using the FMO method[220]. The simultaneous staining for α4β7 and α4 allowed to identify α4β1+ cells[221]. The α4 subunit only combines with either the β1 or the β7

integrin subunit to form a functional receptor. Therefore, if cells stained for α4 but not for α4β7, they were considered to be α4β1 positive.

### 3.12  Multiple myeloma (MM) mouse model

### 3.12.1  MM induction

MOPC cells were kept for a minimum of 9 days in culture and 24 h before injection cells were passaged to ensure exponential growth. $1\times10^5$ MOPC-315.BM luc$^+$, MOPC-315 FUGLW or MOPC-315 FUGLW BMP4 cells (H-2$^d$) in 100 µl phosphate buffered saline (PBS) were injected i.v. via the lateral tail vein into immunocompetent syngeneic BALB/c (H-2$^d$) mice.

### 3.12.2  Drug preparation and treatment

Melphalan (Alkeran, Clinical Pharmacy, Würzburg University) was dissolved in 100 % ethanol to a concentration of 20 mg / ml and further diluted with PBS to a final concentration of 5 mg / kg bodyweight. Mice were injected on days 0, 3, 7, 11 of treatment[222,223].

Cyclophosphamide (Sigma-Aldrich, Munich, Germany) was dissolved in PBS to a concentration of 10 mg / ml and further diluted with PBS to a final concentration of 50 mg / kg bodyweight. Mice were injected on days 0, 2, 4, 8, 11 of treatment[192].

Bortezomib (Clinical Pharmacy, Würzburg University) was already dissolved at a concentration of 1 mg / ml and further diluted with PBS to a final concentration of 1 mg / kg bodyweight. Mice were injected on days 0, 3, 7, 11 of treatment[192].

Vehicle control animals simultaneously received corresponding amounts of ethanol and untreated mice were not injected at all.

All drugs were applied i.p. with a total volume of 100 – 200 µl.

### 3.12.3  Bioluminescence imaging analysis

The BLI measurement on day 0 represented the last image taken when all animals were still untreated, representing the initial tumor burden before drug intervention. Therefore, BLI signals measured at this time point were set to 1 and all following BLI measurements were expressed as fold change of this initial signal.

Untreated or mock treated mice were analyzed on days 11, 19 and 33 after MOPC-315.BM luc$^+$ cell injection to determine average skeletal foci per mouse and the percentage of mice displaying liver and spleen signals. Individual skeletal spots as well as signals arising from spleen and liver were visually determined using the BLI images from ventral and dorsal view.

### 3.13 <u>Histology</u>

For histological examination samples were fixed in 4% neutral-buffered formalin and sotred at 4°C or embedded in Tissue-Tek OCT compound and frozen. Bones were subsequently decalcified for 72 h in formic acid (Merck, Darmstadt, Germany) and after that embedded in paraffin. 2 µm sections were stained with hematoxylin/eosin (HE) and reviewed by an experienced pathologist. In biopsies obtained from spleen and bone marrow the total percentage of tumor infiltration was determined whereas in the liver and lung samples the average amount of tumor cells was determined by evaluation of ten high power fields (HPF, magnification x400). Representative pictures were obtained using a DP26 camera (Olympus, Hamburg, Germany) and the cellSens Entry 1.5 Software version XV 3.5.

Frozen sections were acetone fixed and subsequently stained with CD31 Alexa647 (390, Biolegend), CD4 Alexa488 (RM4-5, Biolegend) and IgA Biotin (11-44-2, eBioscience) followed by Streptavidin Alexa546 (Invitrogen). Nuclei were stained with 4',6-diamidino-2-phenylindole (DAPI). Pictures were obtained using a AxioCamMR3 mounted on an Axio Imager.Z1 microscope (Carl Zeiss, Jena, Germany) with the AxioVision software. The used objectives were either a 20x/0.8 Plan-Apochromat or a 40x/1.30 oil EC Plan-Neofluar.

Frozen sections containing FP labeled cells were not acetone fixed. Instead, samples were kept overnight in a humidified chamber containing 4 % paraformaldehyde before staining.

### 3.14 <u>Enzyme-linked immunosorbent assay (ELISA)</u>

Serum samples for ELISA were obtained by bleeding mice from the tail vein. Blood was allowed to clot, then centrifuged, serum in the supernatant removed and stored at -80°C until further use.

### 3.14.1 M315 specific ELISA

This ELISA specifically detects IgA secreted by MOPC-315 cells and was done as follows:

Mouse blood samples were obtained from tail veins. After clotting, the blood was centrifuged, and the serum was removed and stored at -80°C until further use.

96 well EIA/RIA plates (Corning Inc., Corning, NY, USA) were coated with Ab 2.1-4 in PBS with 0.02 % sodium azide to 2.0 µg/ml and incubated over night at 4 °C.

Then coating solution was poured out and 200 µl blocking solution (PBS with 0.02 % sodium azide and 1 % BSA) per well was added and incubated for 30 min at room temperature.

100 µl sample diluted 1:100 or 1:10 000 in ELISA buffer (PBS with 0.002 % sodium azide, 0.1 % BSA, 0.1 % Tween 20) was added. M315 standard was started with 400 ng/ml and diltuted 2 fold for 10 steps followed by incubation at 37 °C for 2 h.

Three washes with ELISA wash buffer (Biolegend) were performed.

Biotin rat-anti-mouse IgA (clone C10-1, BD Pharmingen) was diluted in ELISA buffer to a concentration of 1 µg/ml, added 100 µl per well and incubated for 1 h at 37 °C.

Three washes with ELISA wash buffer were performed.

Then streptavidin alkaline phosphatase (GE Healthcare) was diluted 1:3000 in ELISA buffer, 100 µl per well added and incubated for 1 h at 37 °C.

Three washes with ELISA wash buffer were performed.

The phosphatase substrate (Sigma-Aldrich, Munich, Germany) was diluted in substrate buffer (97 ml diethanolamin, 800 ml distilled water, 101 mg $MgCl_2$ x $6H_2O$, 200 mg sodium azide, add 10 ml 37 % HCl and fill up with distilled water to 1 l) to 1 mg/ml and added 100 µl per well.

After 25 min at room temperature the absorbance was detected at 405 nm.

Between the steps wells were washed 3 times with ELISA wash buffer (eBioscience).

All samples were assayed in duplicates.

### 3.14.2  Data analysis

Resulting data was analyzed with Prism 5 (GraphPad, La Jolla, CA, USA).

The standard curve was created from the mean value of assayed standards by a point-to-point construction with 1000 points. Means from unknown samples were determined by interpolation from this standard curve.

### 3.15  Statistics

Statistical analysis was performed with InStat 3.00 or Prism 5 software (GraphPad, La Jolla, CA, USA). To determine tumor growth over time, at each timepoint, BLI data were compared among the mouse groups with a two way ANOVA and Tukey post test for multiple comparisons. Adjusted p values are stated. The Kruskal-Wallis test and Dunn post test were applied for comparisons among the three groups. A two tailed t-test was used to analyze the statistical significance of differences between two groups. Differences in survival time were calculated by a Log-rank (Mantel-Cox) test with Bonferroni correction. All measurements are expressed as the mean with standard deviation (SD), unless stated otherwise.

# 4 Results

## 4.1 Characterization of FP635

### 4.1.1 Signal attenuation

As we aimed to use FP635 as sensitive reporter for non-invasive whole body imaging we wanted to determine the signal attenuation characteristics of FP635. Therefore, we compared it to DsRed-Monomer, which emits in the red color spectrum and eGFP, the classical and widely used FP[42], emitting in the green spectrum. As besides hemoglobin, melanin is known to be one of the major light attenuators[18] we chose to test the signal attenuation of the three FPs with skin of different melanin content. We covered the wells containing cells expressing the different FPs with pinnae of BALB/c (melanin poor) and C57BL/6 (melanin rich) mice. As expected the signal of all FPs was stronger attenuated by melanin rich skin than melanin poor **(Figure 4A,B)**. Overall, we detected a signal absorption correlating with FP emission and excitation wavelength. FP635 was least attenuated by melanin rich skin with 87.7 % followed by DsRed-Monomer with 89.2 % and eGFP with 90.5 %. The same order was apparent with melanin poor skin, though signal absorption was generally lower. FP635 was attenuated by 76.8 %, DsRed-Monomer by 77.7 % and eGFP by 80.3 % **(Figure 4A,B)**. Obviously, the reduction of melanin leads to 10-11 % less signal attenuation in all three FPs measured. Nevertheless, although between the emission maxima of FP635 (635 nm) and eGFP (509 nm) are 126 nm the difference in signal absorption was only 2.8 % (melanin rich) and 3.5 % (melanin poor).
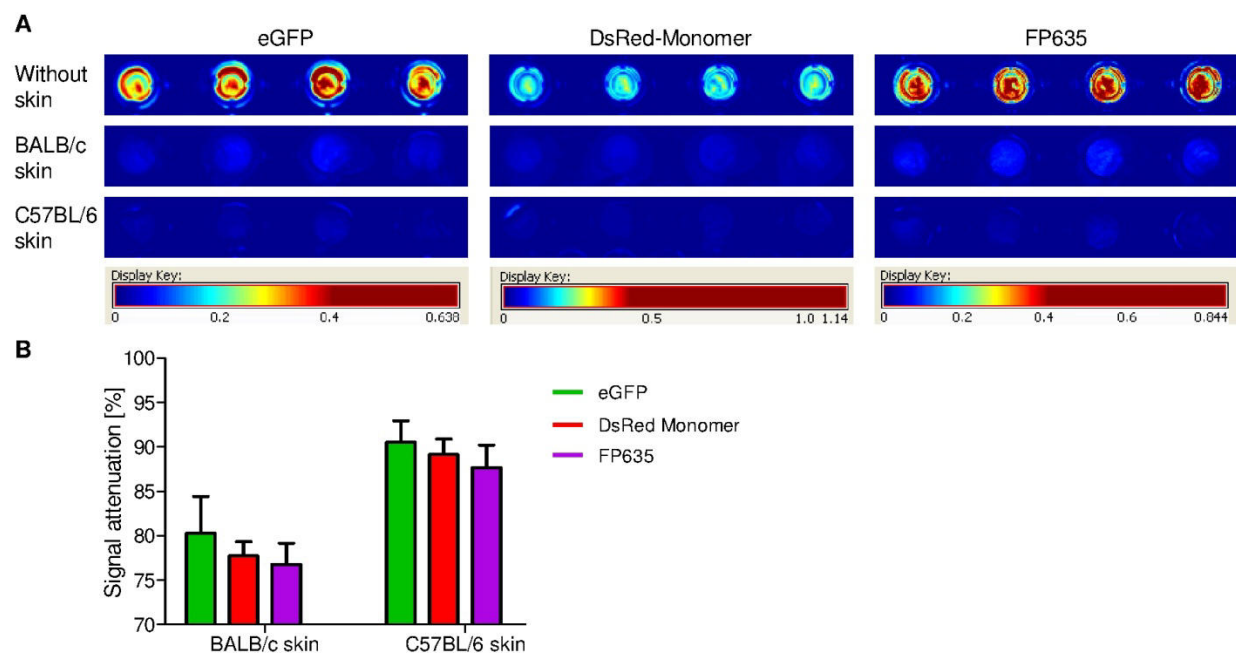


**Figure 4: Signal attenuation by skin tissue *in vitro* of eGFP, DsRed-Monomer and FP635.** 293FT cells were transfected with plasmids expressing either eGFP, DsRed-Monomer or FP635. **(A)** $2.5 \times 10^6$ cells were seeded in 96 well plates and signal intensities measured. Then wells were covered with

BALB/c skin (melanin poor) and C57BL/6 skin (melanin rich) respectively and signal intensities were measured again. **(B)** Quantification of skin absorption measurements, shown is the percentage (mean with SD) of absorbed signal. The experiment was done in quadruplicates.

### 4.1.2   2-photon photostability

Photostability of FPs is an important characteristic, especially if cells tagged with an FP should be tracked by microscopy over longer timespans. As we aimed to use FP635 also in applications of non-invasive microscopy using 2-photon excitation we compared the bleaching behavior of FP635 to eGFP and DsRed-Monomer. With the respective FP transfected 293FT cells were therefore bleached under similar conditions by using the same output laser power of 100 mW. eGFP performed best and the time to lose 50 % of the initial brightness was above 900 sec ($t_{1/2}$>900 sec) followed by DsRed-Monomer with $t_{1/2}$=411 sec and FP635 with $t_{1/2}$=108 sec. Especially during the first 200 seconds FP635 bleached remarkably fast compared to the two other FPs **(Figure 5)**.
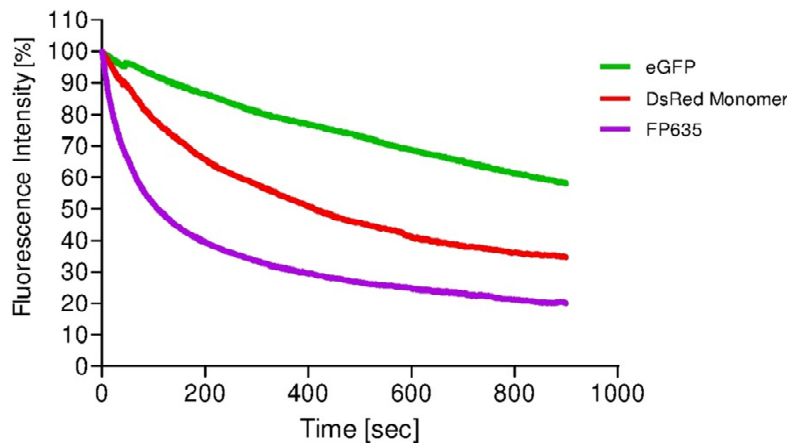


**Figure 5: 2PM bleaching of living 293FT cells in monolayers.** Output laser power on the cells was adjusted to 100 mW. Excitation wavelength and detection filters used: eGFP 930 nm, 535/50; DsRed-Monomer and FP635 1100 nm, 605/70. For 900 sec every second one image was acquired. Shown is the mean bleaching of on average 10 measured spots.

### 4.1.3   Generation and characterization of FP635 transgenic mice

In the next step we used a lentiviral construct to generate transgenic (tg) mice expressing FP635 under the ubiquitin promoter **(Figure 6A)**. By means of fluorescence imaging and flow cytometry of peripheral blood mononuclear cells (PBMCs) several possible founders were identified. Founder 3855 presented the best brightness of PBMCs in comparison to other possible founders **(Figure 6B)**. Additionally, the newborn founder 3855 exhibited strong FP635 expression detectable by whole body fluorescence imaging **(Figure 6C left)** while under the same conditions the C57BL/6 wt mouse was almost not detectable **(Figure 6C right)**.

As we intended to use the immune cells from this transgenic mouse line to study acute GVHD and adaptive immune responses against tumors such as multiple myeloma, we examined the FP635 expression of leukocyte subpopulations. PBMCs derived from founder 3855 clearly expressed FP635 in around 75 % of $CD3^+$, $CD4^+$ and $CD8^+$ immune cells as measured by flow cytometry **(Figure 6D)**. Moreover, whole splenocytes from two tg offspring mice showed by flow cytometry a clear shift compared to C57BL/6 wt cells **(Figure 6E)**. Additionally the brightness of these splenocytes was measured by fluorescence imaging. $1 \times 10^6$ splenocytes of these mice were twice above the background signal which was represented by C57BL/6 splenocytes **(Figure 6F)**.
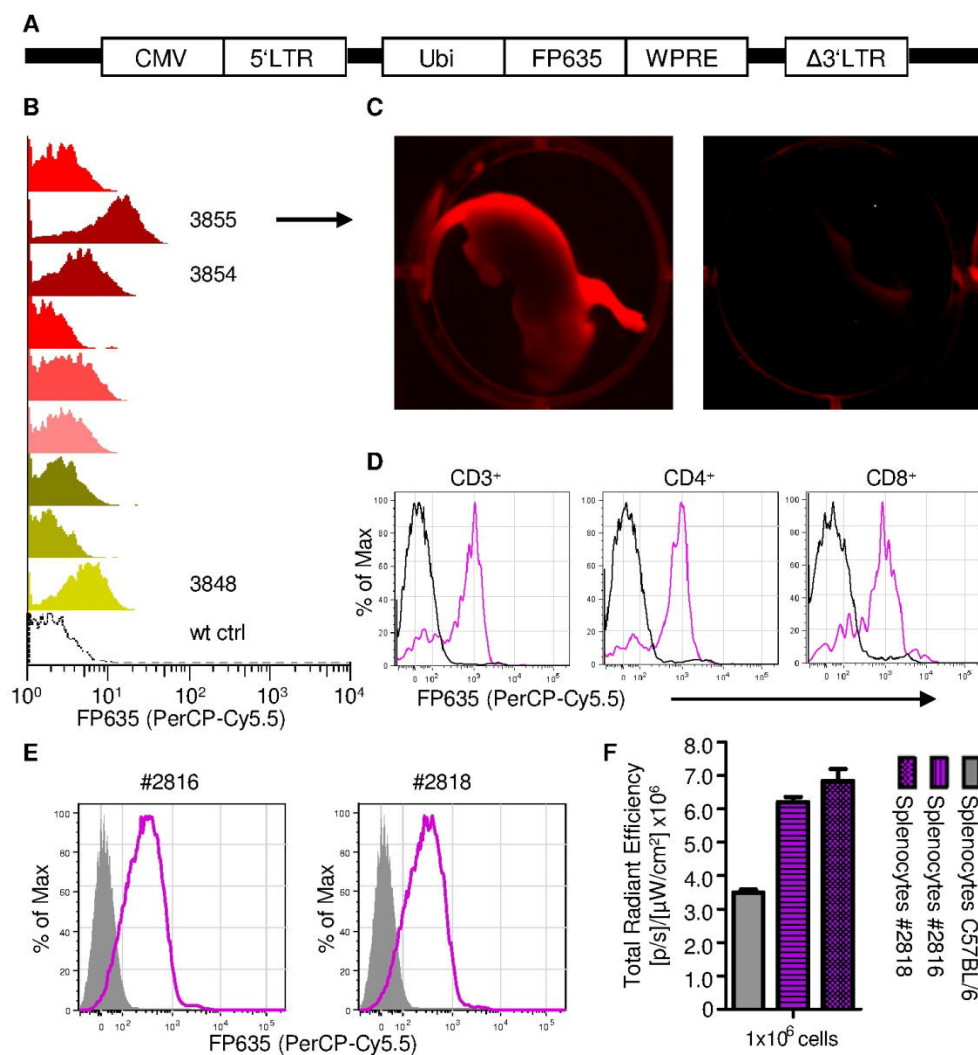


**Figure 6: Construct, selection of founder mouse and FP635 expression level of lymphocyte subsets. (A)** The lentiviral construct used for generating the transgenic mice contains a chimeric 5' long terminal repeat (CMV/5'LTR) and a self-inactivating 3' long terminal repeat (Δ3'LTR), the human ubiquitin promoter (Ubi) driving the expression of FP635, which is linked with the Woodchuck protein response element (WPRE) for stabilizing the mRNA. **(B)** PBMCs of newborns were analyzed by flow cytometry for FP635 expression. Shown is founder 3855 with high FP635 expression compared to other founder and the wildtype control. **(C)** Whole body imaging on a Perkin Elmer Fluorescence Imager of newborn 3855 founder (left) and C57BL/6 wildtype newborn (right) with excitation wavelength of 550 nm and emission detection at 650 nm with 30 sec exposure. Note that skin pigmentation of melanin rich areas on the back and head leads to signal attenuation. **(D)** PBMCs derived from founder 3855 were stained for CD3, CD4 and CD8 and analyzed by flow cytometry. A

gate around the lymphocyte population using SSC and FSC was set. Within this population cells were gated for either CD3$^+$, CD4$^+$ or CD8$\alpha^+$ as indicated and depicted in histograms. Black line shows C57BL/6 wildtype PBMCs, pink line shows PBMCs from 3855. **(E)** Splenocytes derived from two selected offspring of the 3855 founder line (2816 and 2818) analyzed by flow cytometry for FP635 expression, wt cells are shown in grey. **(F)** *In vitro* brightness measurement of transgenic splenocytes from two offspring and from C57BL/6 wildtype using the IVIS spectrum FLI option with filter settings 570 ex / 640 em.

### 4.1.4   Laser scanning 2-photon microscopy (2PM) deep tissue imaging

As described 4.1.1, we found slight advantages in signal attenuation of FP635 compared to eGFP and DsRed-Monomer. When challenging FP635 with melanin rich tissue we found 2.8 % less signal absorption compared to eGFP and 1.5 % less compared to DsRed-Monomer. Therefore, we asked in this experiment to what extent this advantage in signal attenuation is reflected when detecting cells in deep tissue by 2PM. To this end we chose an organ with high hemoglobin content, namely the spleen, for detection of single cells. We reconstituted B- and T-cell deficient B6.129S7-Rag1$^{tm1Mom}$/J mice (H-2$^b$) with either eGFP B cells and DsRed-MST T cells or eGFP B cells and FP635 T cells (all H-2$^b$). After 7 weeks the transferred cells were engrafted as shown by flow cytometry analysis of PBMCs **(Figure 7A,B)**. In mice reconstituted with DsRed-MST T cells and eGFP B cells, CD4$^+$ and CD8$^+$ cells exhibited clear DsRed-MST fluorescence that exceeded wt cells by 3.5 log. The detected CD19$^+$ or B220$^+$ eGFP$^+$ B cells were also clearly detectable and ranged around 3 log fold above wildtype cells **(Figure 7A)**. Mice reconstituted with FP635 T cells and eGFP B cells, showed similar measurements for eGFP expression in CD19$^+$ and B220$^+$ cells compared to mice with DsRed-MST co-transferred cells. Interestingly, detection of FP635 tg CD4$^+$ and CD8$^+$ cells was difficult and the T cells appeared dim did not clearly separate from wt cells **(Figure 7B)**. The cells from FP635 tg donor mice were not as bright as the immune cells from the original founder 3855 **(Figure 7D)** and the two measured offspring **(Figure 5E)**. In terms of CD4$^+$, CD8$^+$, CD19$^+$ and B220$^+$ both reconstituted groups showed similar numbers, indicating similar immune cell engraftment **(Figure 7A,B)**. Subsequently, mice were sacrificed, spleens removed and imaged by 2PM. To standardize measurements between the two groups and avoid bias by melanin rich regions in the spleen, eGFP B cells occurring in both groups were used as calibrator. The measured penetration depth of DsRed-MST and FP635 B cells was set in relation to the eGFP measurement.

Penetration depths of eGFP B cells were similar in both groups, with a mean of 67.7 µm and a maximum of 178.8 µm in the DsRed-MST group **(Figure 7C left)** and a mean of 65.1 µm and maximum 160.3 µm in the FP635 group **(Figure 7C right)**. DsRed-MST T cells were detectable deeper in the tissue than eGFP B cells, with an average depth of 99.7 µm and a maximum of 232.1 µm **(Figure 7C left)**. This is in accordance with the previous signal attenuation experiment, where the DsRed signal was less absorbed compared to eGFP **(Figure 4B)**. The measured penetration depth for FP635 T cells was comparable to the co-

transferred eGFP B cells, with a mean depth of 63.4 µm and a maximum of 141.4 µm **(Figure 7C right)**. This performance was not as expected from signal attenuation experiments, where FP635 fluorescence was least attenuated **(Figure 4B)**. In order to gain a good signal to background ratio we even needed to considerably increase MPM laser power to achieve a good detection of FP635 T cells.

The measured advantage in signal attenuation of DsRed-Monomer versus eGFP is reflected in this MPM tissue penetration experiment but not the attenuation advantage of FP635. During the MPM detection FP635 T cells occurred rather dim in comparison to eGFP B cells and DsRed-MST T cells. As we see in the flow cytometry analysis of PBMCs from reconstituted mice FP635 T cells do not clearly separate from wt cells. Therefore, we checked the brightness of the splenocytes from all three transgenic mouse lines used in the reconstitution experiment. By using the Maestro imaging system with the following filter sets it was possible to similarly efficiently excite the FPs and also detect the emission comparably. eGFP was detected with the blue filter set (excitation range 435-480 nm, emission filter 490 nm longpass), DsRed with the green filter set (excitation range 503-548 nm, emission filter 560 nm longpass) and FP635 with the yellow filter set (excitation range 576-621 nm, emission filter 635 nm longpass). The measurement clearly showed that eGFP and DsRed-MST tg splenocytes were similarly bright but FP635 tg cells were more than 5 fold less bright **(Figure 7D)**. This could be the reason, why FP635 T cells were likewise detectable to eGFP B cells and performed worse compared to the DsRed-MST T cells.
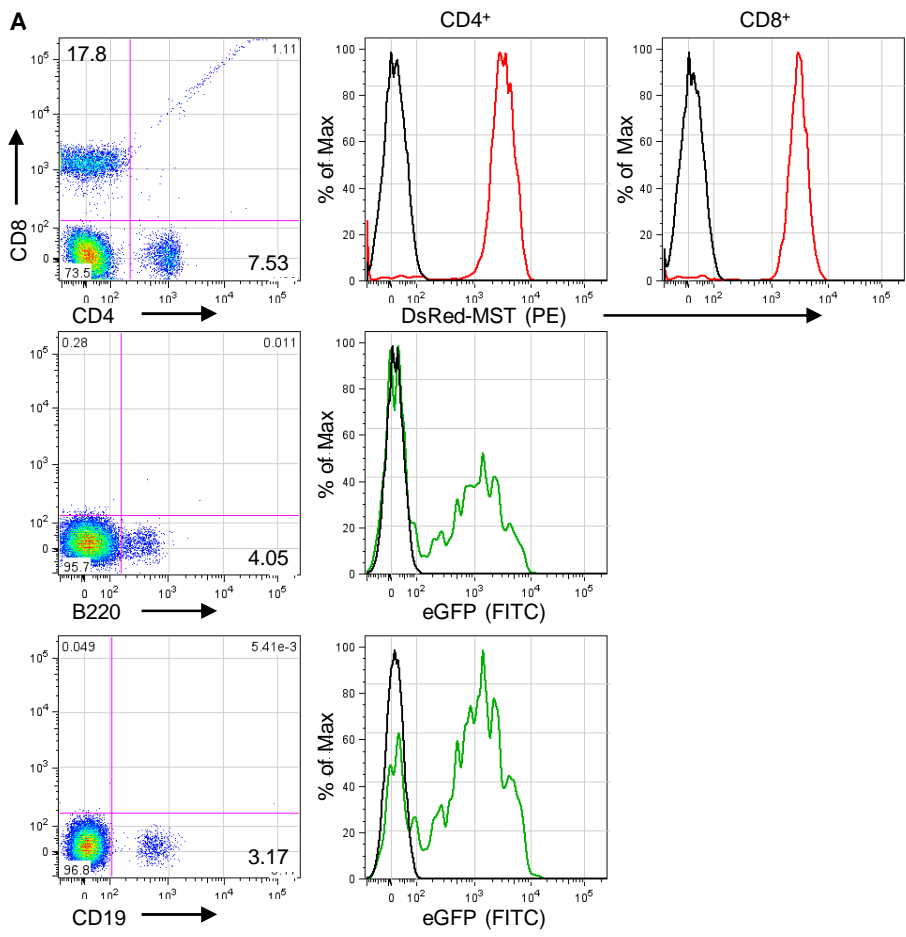
**A** — Reconstituted with: DsRed-MST+ T cells + eGFP+ B cells
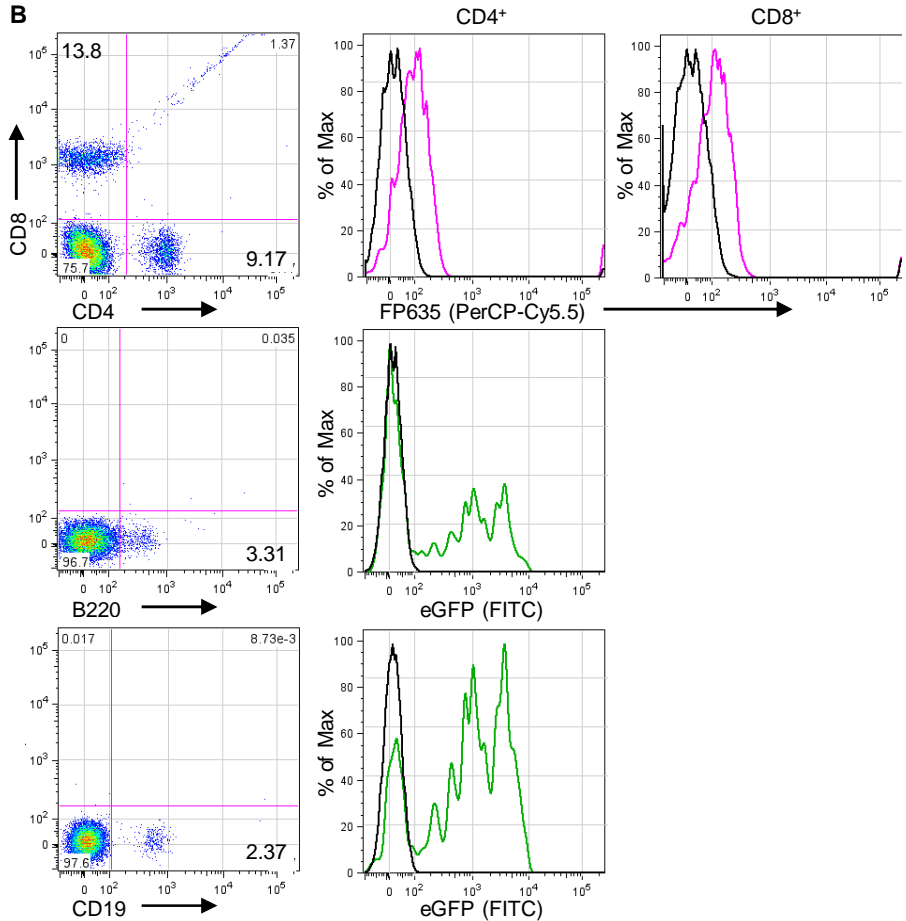
**B** — Reconstituted with: FP635+ T cells + eGFP+ B cells
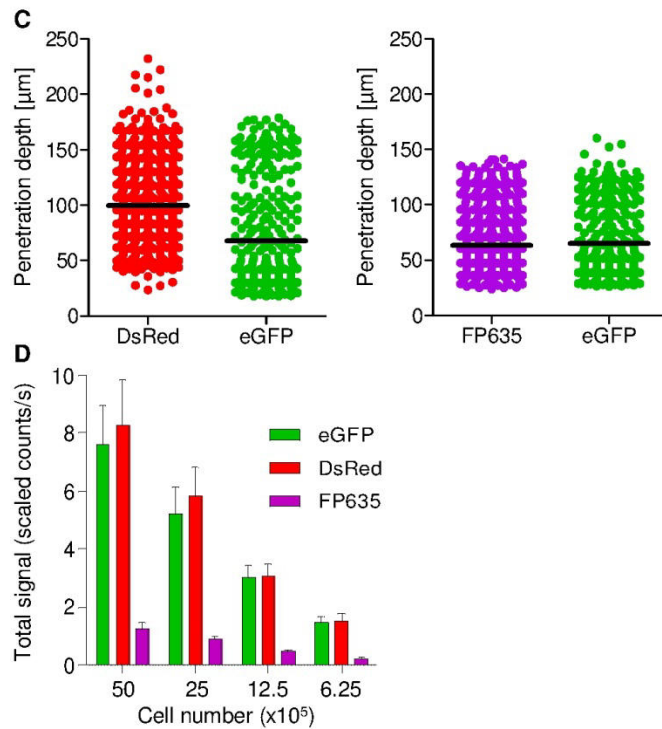
**Figure 7: Flow cytometry analysis of transferred cells in reconstituted mice and subsequent 2PM imaging of spleens.** Before 2PM, PBMCs of reconstituted mice (7 weeks) were analyzed by flow cytometry. A gate surrounding the lymphocyte population was set and subgated on CD4^{+}, CD8^{+}, CD19^{+} and B220^{+} cells (dot plots). Within those positive populations the degree of fluorescence protein expression was checked (histograms). **(A)** Representative mouse reconstituted with eGFP^{+} B cells and DsRed-MST^{+} T cells. **(B)** Representative mouse reconstituted with eGFP^{+} B cells and FP635^{+} T cells. **(C)** Later, mice were sacrificed and spleens imaged by 2PM. To keep measurements between mice comparable and avoid any bias, performance of DsRed-MST[+] and FP635^{+} cells was compared to eGFP^{+} cells as they were present in both groups. Used excitation wavelength for DsRed-MST and FP635 was 1100 nm using a 605/70 filter for emission detection and 930 nm for eGFP using a 535/50 filter. Each dot represents one measured cell. **(D)** Splenocytes from transgenic FP expressing mice as indicated were titrated in 96 well plates and the brightness of the cells measured. Mice from these strains were also used as donors for the reconstitution experiment. For the measurements the Maestro imaging system was used with blue filter set for eGFP, green filter set for DsRed-MST and yellow filter set for FP635.

## 4.2 Application of FP635 for *in vivo* imaging of acute GVHD and tumor cells

### 4.2.1 Imaging of acute GVHD induced with FP635^{+} or DsRed-MST[+] luc[+] splenocytes

Next, we asked whether FP635 tg splenocytes could be applied for non-invasive FLI detection of complex immune processes, such as acute GVHD. Sensitive *in vivo* detection of acute GVHD by BLI is established in the laboratory of A. Beilhack, therefore dynamics of the disease and spatiotemporal location of immune cells are known[24]. To include a control group with luciferase labeled splenocytes we used the DsRed-MST luciferase double transgenic immune cells. As these cells additionally express DsRed-MST we also had a direct FP competitor to FP635.

Because FP635 tg cells appeared dim in previous experiments (4.1.4) we transplanted more cells to enhance detection. From each tg donor we transplanted $2x10^7$ splenocytes while usually $4x10^6$ splenocytes suffice to induce lethal GVHD in recipient mice within 12 days[24]. To further enhance imaging sensitivity nude mice were used as recipients. It is expected that on day +2 and +3 after transplantation the transferred immune cells will accumulate in secondary lymphoid tissues where priming and proliferation takes place[24]. We confirmed this cell distribution pattern by BLI, and detected on d+2 distinct signals from cervical lymph nodes (cLN), axillary LNs (aLN), the spleen and mesenteric LNs (mLN) **(Figure 8C)**. Signals in secondary lymphoid organs increased by d+3 and signal localization was confirmed by *ex vivo* imaging **(Figure 8C)**. This distribution pattern of immune cells was not detectable when imaging the same mice by FLI although luc^{+} cells also expressed DsRed-MST **(Figure 8B)**. We could not detect the DsRed-MST signal non-invasively but upon *ex vivo* imaging we measured FP signals from cLNs, iLNs and weakly from Peyer's Patches (PP). Yet the spleen signal which was readily detected by BLI was not visible by FLI **(Figure 8B,C)**. Whole body FLI of FP635 transplanted mice did not yield any signal on d+2 or d+3 **(Figure 8A)**. *Ex vivo* imaging of the gastrointestinal tract and the spleen did also not exhibit specific FP635 signals. Probably weak signals were detected from cLNs and iLNs but the high background resulting from long exposure times should be noted **(Figure 8A, *ex vivo*, left panel)**. On day 5 after transplantation, when the effector phase of GVHD is taking place and the primed T cells leave the secondary lymphoid organs to infiltrate GVHD target organs gastrointestinal tract, liver and skin[24] we still could not detect any FP635 signal by non-invasive FLI **(Figure 8D)**. However, *ex vivo* FLI revealed weak signals from cLNs and iLNs but again, the high background resulting from long exposure times indicated only very dim signals. From the gastrointestinal tract we only detected gastric autofluorescence which is a well known challenge in whole body FLI[2,5] **(Figure 8D *ex vivo*)**. In contrast, *in vivo* imaging on d+5 of a DsRed-MST transplanted mouse revealed a clearly detectable signal from cLNs, aLNs and iLNs **(Figure 8E)**. *Ex vivo* imaging corroborated the signal localization and further allowed detection of DsRed-MST T cells in PPs and the mLNs **(Figure 8E, *ex vivo*)**. As already described in 4.1.4, DsRed-MST outperformed FP635 measured by 2PM in terms of sensitivity. The cause might be again the lacking brightness of FP635 immune cells in comparison to DsRed-MST cells. Overall we found the detection of luciferase expression by BLI to be way more sensitive than FP detection by FLI.
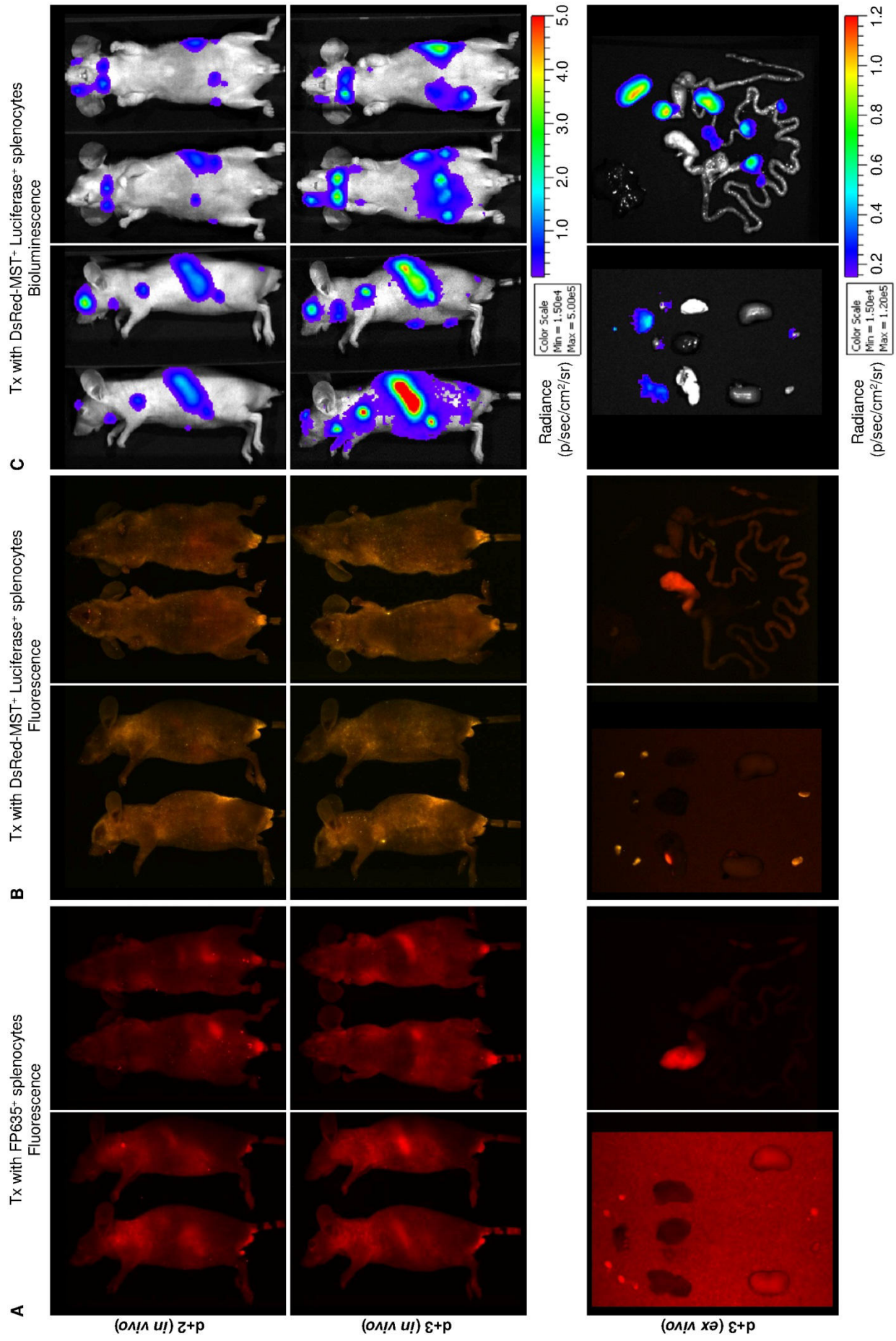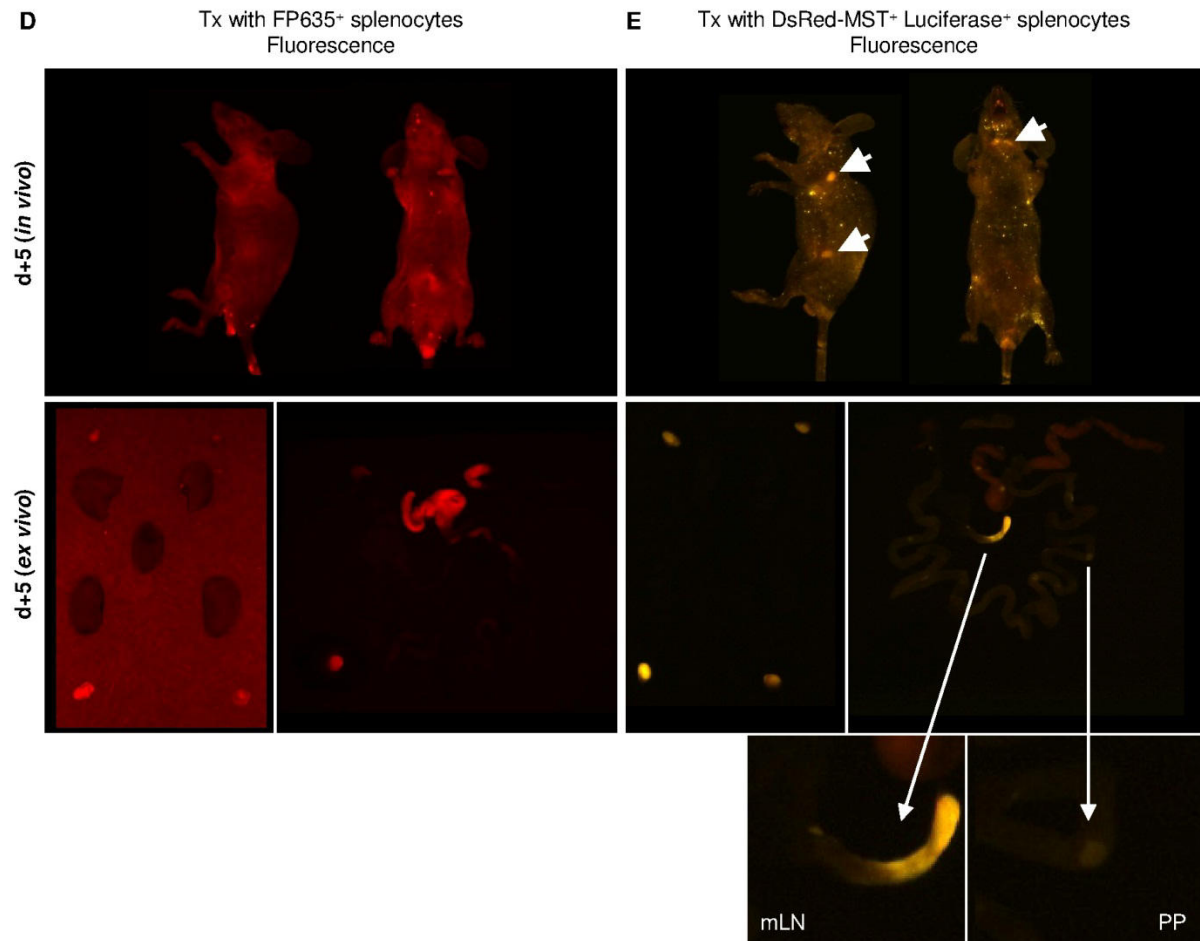
**Figure 8: Induction of aGVHD followed by BLI and FLI, *in vivo* and *ex vivo*.** Nude mice (CByJ.Cg-*Foxn1^{nu}*/J, H-2^{d}) were lethally irradiated with 8 Gy followed by intravenous injection of $5\times10^{6}$ C57BL/6J WT (H-2^{b}) bone marrow cells and $2\times10^{7}$ whole splenocytes from either DsRed-MST^{+} Luciferase^{+} or FP635^{+} (all H-2^{b}) donor mice. Recipients transplanted with double positive cells were imaged by bioluminescence and fluorescence detection to directly compare sensitivity. For *ex vivo* images mice were killed and organs prepared as follows (from top): left panel: cervical LNs, lungs, heart, kidneys, inguinal LNs; right panel: spleen, gastrointestinal tract, liver. **(A, B, C)** FLI and BLI of transplanted recipients as indicated on days 2 and 3 after HCT and *ex vivo* imaging on d+3. **(D, E)** FLI of transplanted recipients as indicated 5 days after HCT with subsequent *ex vivo* FLI. Arrowheads indicate cervical, axillary and inguinal LNs. Inserts show zoomed in mesenteric LNs (mLN) (left) and Peyer's patch (PP) (right).

## 4.2.2 FP635 expressing tumor cells for whole body FLI

From the two previous experiments we learned that not only the wavelength of excitation and emission of a respective FP but also the brightness of the labeled cells is key for non-invasive detection. The signal intensity of a given cell depends on several factors such as the intrinsic brightness of the used FP which relies on the extinction coefficient and the quantum yield[58]. Additionally, the FP expression level plays an important role. It is specified by the number of insertion sites, the used promoter and the metabolic activity of the cell. Therefore, we chose to lentiviral transduce MOSEC tumor cells. The lentiviral transduction usually leads to multiple insertion sites of the transgene, here the FP635, and tumor cells generally readily express the transgene. With these MOSEC FP635^{+} cells we aimed to establish a tumor

model which could easily be used complementary to luciferase labeled immune cells to study immune cell – tumor cell interactions.

We injected MOSEC FP635$^+$ or MOSEC wt cells i.p. into NSG mice and regularly monitored the mice by *in vivo* FLI. Around 16 days after tumor cell inoculation we were able to detect a specific FLI signal of MOSEC FP635$^+$ cells from the lower peritoneal area **(Figure 9A)**. In the course of the experiment the initial signal steadily increased inside the measurement region **(Figure 9C)**. Moreover, we observed tumor spread from the initial growth area to various parts of the peritoneum **(Figure 9A)**. To verify the signal localization, we sacrificed the mice after 62 days, removed the peritoneum, turned it inside out and performed *ex vivo* FLI **(Figure 9B)**. We found various small tumor nodules spread over the whole peritoneum and the areas of accumulation resulted in a strong *in vivo* as well as *ex vivo* FLI signal. Although the MOSEC cells had spread over the peritoneum and did not grow at a single spot, such as usual in subcutaneous tumor models, we still reliably detected tumor growth and spread *in vivo*. Therefore, we were interested in the actual brightness of the used MOSEC FP635$^+$ cells. We determined the brightness by *in vitro* FLI and flow cytometry. MOSEC FP635$^+$ cells turned out to be 90 fold above background (background corresponds to MOSEC wt cells) by *in vitro* FLI **(Figure 9D)**. In comparison, FP635 tg immune cells were only 2 fold above wt background signal under the same conditions **(Figure 6F)**. Flow cytometry further confirmed the high brightness of MOSEC FP635$^+$ cells that clearly separated from the wt MOSEC cells **(Figure 9E)**. Furthermore, we detected MOSEC FP635$^+$ cells by fluorescence microscopy. MOSEC FP635$^+$ cells were not only clearly spotted by their typical morphology and high nuclear density but also by high FP635 fluorescence **(Figure 10A)**. MOSEC wt cells in turn exhibited no autofluorescence using equal exposure times but showed the same growth pattern as MOSEC FP635$^+$ cells **(Figure 10B)**.
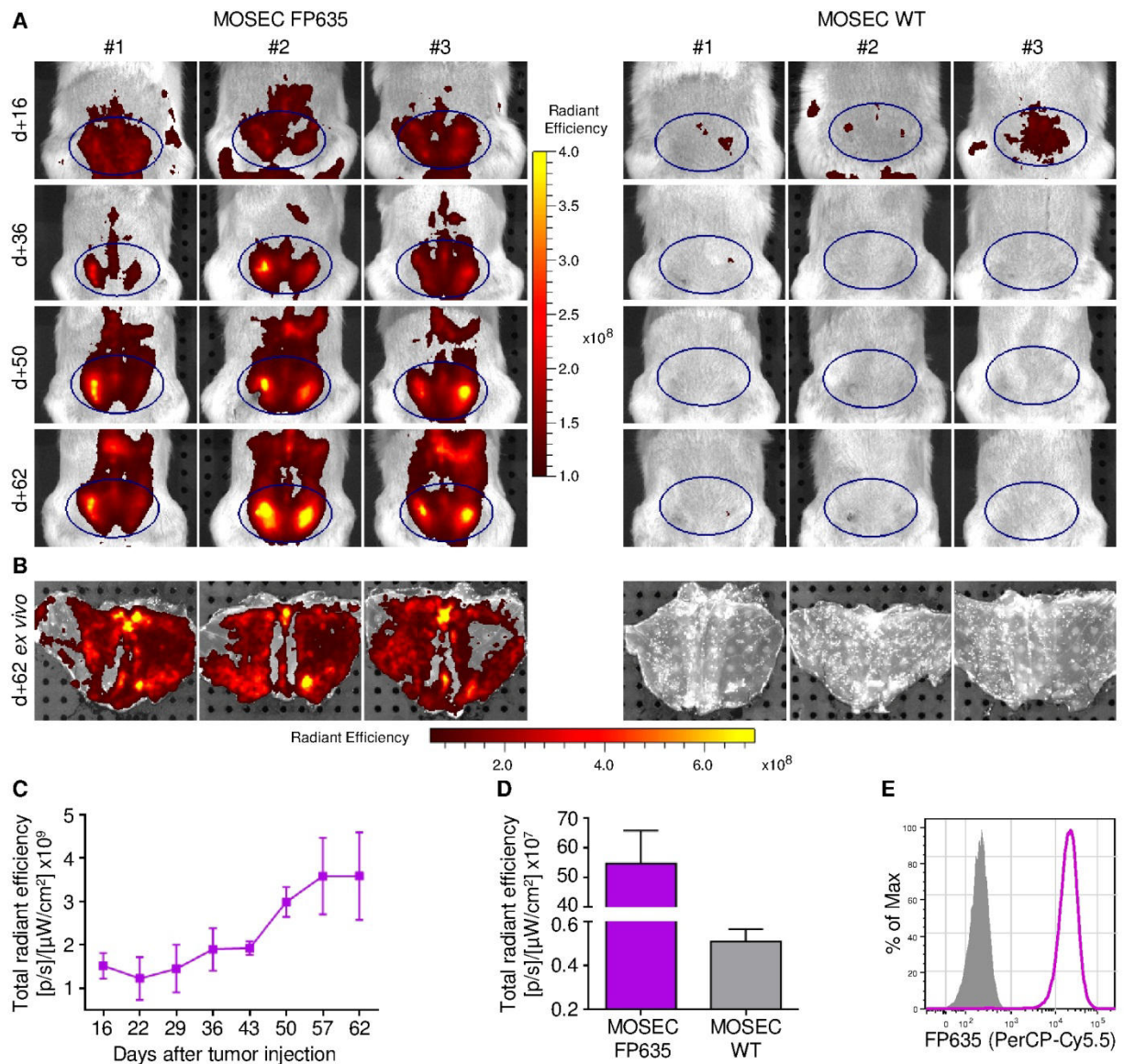
**Figure 9: *In vivo* FLI of MOSEC tumor cells and cell brightness measurements.** $1 \times 10^6$ MOSEC FP635^{+} or MOSEC wt cells were injected i.p. into female NSG mice. **(A)** Tumor growth was regularly observed by non-invasive FLI using the IVIS spectrum fluorescence imaging option (570 nm excitation and 640 nm emission filters). MOSEC wt injected animals were used as control for background autofluorescence. FLI signals increased over time, indicating tumor growth and spread. **(B)** After 62 days, animals were sacrificed, the peritoneal skin removed and flipped inside-out. Subsequent *ex vivo* FLI confirmed the *in vivo* detected tumor growth and localization. **(C)** Quantification of *in vivo* FLI signal measurements over time shows tumor mass increase (measurement regions, blue circles in **A**). Values shown are true FP635 signals calculated as follows: FP635 signal of each measurement region minus mean background of all three measurement regions from wt MOSEC mice. **(D)** *In vitro* cell brightness measurement of $1 \times 10^6$ MOSEC FP635^{+} cells in comparison to wt MOSEC cells using the IVIS spectrum with 570 nm excitation and 640 nm emission filters. **(E)** Flow cytometry analysis of MOSEC FP635^{+} (pink open histogram) and MOSEC wt (grey filled histogram).
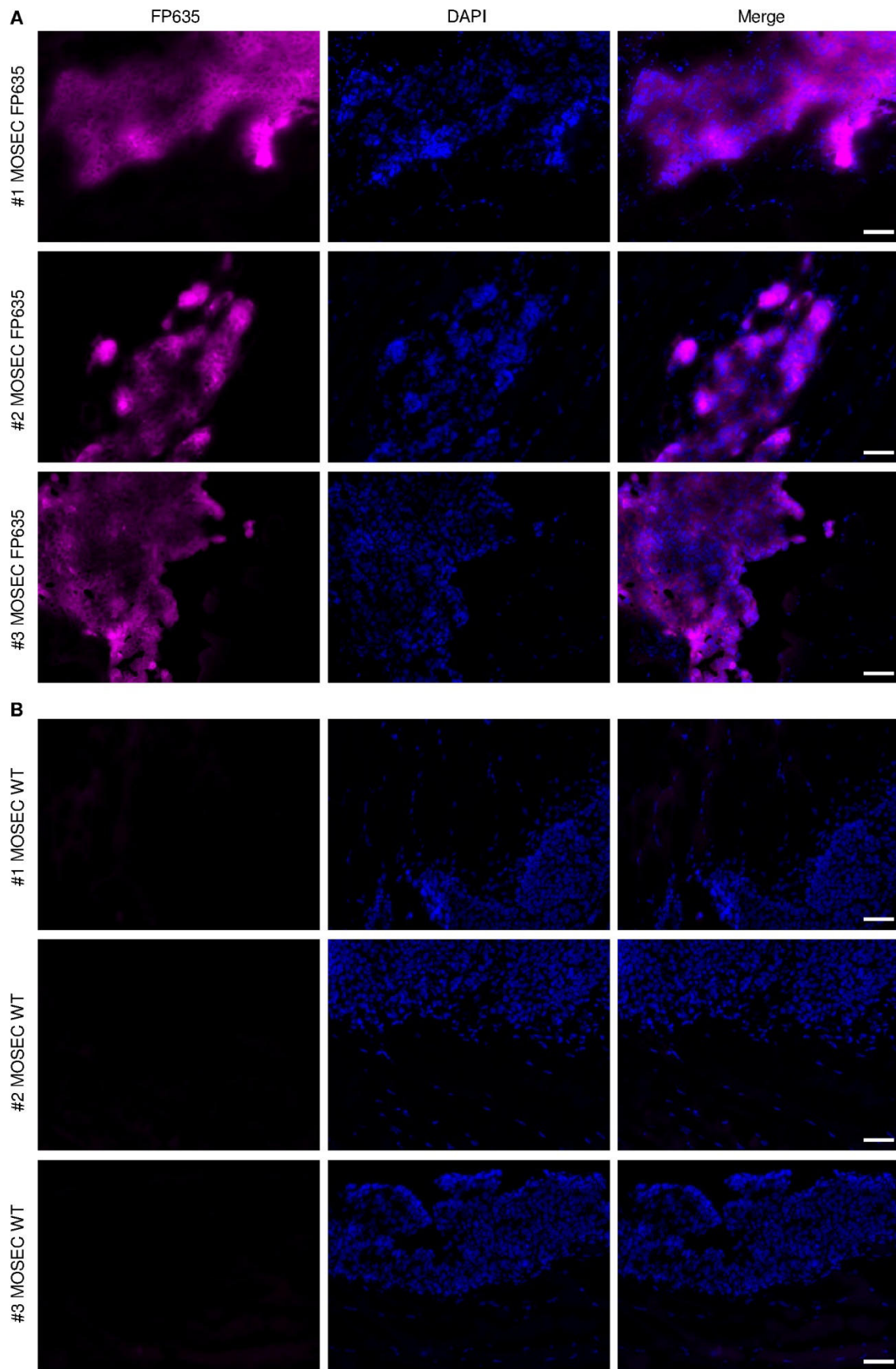
**Figure 10: Fluorescence microscopy of FP635$^+$ MOSEC cells.** Female NSG mice were injected with 1x10$^6$ **(A)** MOSEC FP635$^+$ or **(B)** MOSEC wt cells i.p. 62 days after tumor inoculation mice were sacrificed. Shown are representative DAPI stainings of the peritoneum from each group. Areas with accumulating nuclei always correlate with the presence of MOSEC cells. MOSEC FP635$^+$ cells are

clearly detectable. MOSEC wt cells show a similar growth pattern as depicted by DAPI[+] nuclei but do not exhibit mentionable autofluorescence. For direct comparison, all images were taken with the same exposure times. Scale bar is 20 μm for all sections (original magnification 200x / 0.8 NA). pink = FP635, blue = 4',6-diamidino-2-phenylindole (DAPI) stained nuclei.

## 4.3 Preclinical multiple myeloma mouse model

### 4.3.1 Effective migration of MOPC-315.BM luc$^+$ myeloma cells to hematopoietic compartments

To investigate the behavior and biology of MM cells in the context of the living organism we transferred i.v. light emitting luciferase expressing MOPC-315.BM luc$^+$ cells into BALB/c recipients. First, we addressed homing patterns, expansion and dissemination of MM cells by sequential non-invasive bioluminescence imaging (BLI). By day +11 after MM injection we detected discrete luciferase signals emitted by the MOPC-315.BM luc$^+$ cells in all recipients **(Figure 11A)**. Light emitting foci appeared most frequently at anatomical sites corresponding to the location of skull, vertebrae, sternum, femur, tibiae and other parts of the skeleton, on average 1.6 skeletal bioluminescent foci per mouse by day +11, **(Figure 11B)** and projected in 57% of the mice to the spleen **(Figure 11C)** (n = 51 on day +11, n = 56 on day +19 and n = 25 on day +33 from 3 independent experiments). Therefore, early homing sites of MOPC-315.BM luc$^+$ cells primarily comprised the hematopoietic compartment. From these initial proliferation hot spots the myeloma cells metastasized to other skeletal areas **(Figure 11A arrows)**. Between day +19 and day +33 the average number of skeletal MM foci increased from around 3 to over 10 per mouse **(Figure 11B)**. After day +19 almost all mice displayed signals from the spleen **(Figure 11C)**. Of note, signals from the liver appeared in 90% of mice on day +11 but unlike skeletal or splenic foci, liver signals did not increase and remained comparatively low throughout the experiment **(Figure 11A)**. To address whether initial focal tumor growth or rather disseminated multiple myeloma proliferation accounts for increased tumor burden, we marked 4 representative spots **(Figure 11A)** and measured the signal intensities over time **(Figure 11D)**. Spot 1 and 2 represent signals from the femur, spot 3 the spleen and spot 4 the skeletal part of the shoulder. Indeed, signals increased locally at these four defined spots over time **(Figure 11D)**. This initial persistent focal tumor growth and the subsequent spreading to distant skeletal parts finally resulted in a steady increase of luciferase signal **(Figure 11E)**. Bone remodeling and osteolytic lesions were detected in >35% of animals at 42 days after MM injection. For example, corticalis destruction was observed in the neck of the femur **(Figure 11F)**.
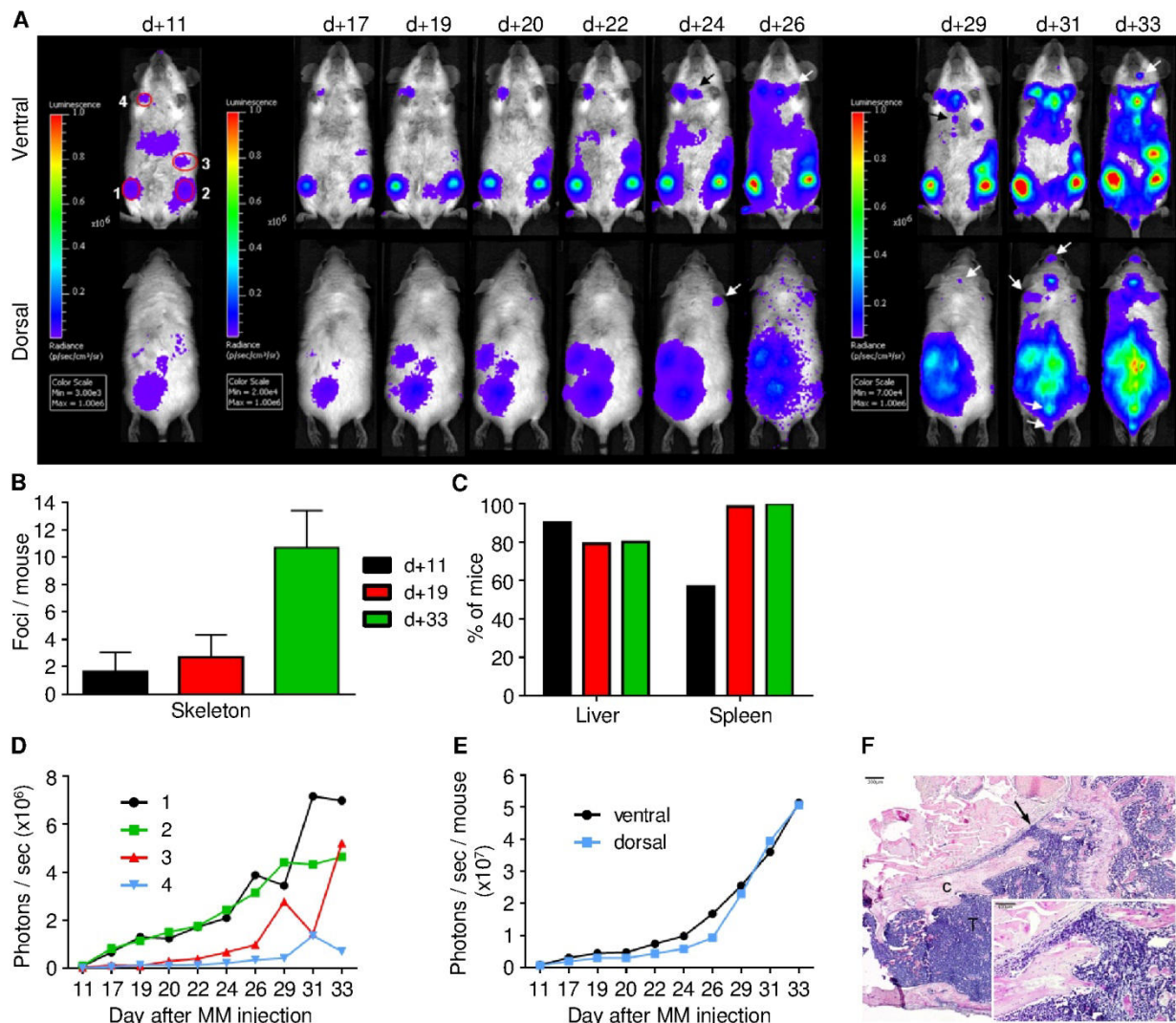
**Figure 11: Engraftment and growth dynamics of MOPC-315.BM luc$^+$ myeloma cells *in vivo*.** BALB/c wild type mice were injected with 1x10$^5$ MOPC-315.BM luc$^+$ cells via the tail vein. Tumor growth and spread was regularly monitored by BLI. **(A)** BLI images of one representative mouse at indicated time points after MM injection from ventral (top) and dorsal (bottom) view. Additional emerging tumor foci over time are marked with black or white arrows. **(B)** Number of skeletal spots per mouse on days +11 (n = 51), 19 (n = 56) and 33 (n = 25) and **(C)** percentage of mice presenting signals from liver and spleen. **(D)** Quantification of single tumor foci over time as marked in (A): 1 and 2 = BM compartment of femur/tibia, 3 = spleen, 4 = BM compartment of shoulder. **(E)** Absolute signal quantification by whole body BLI from ventral and dorsal views. **(F)** Representative osteolytic lesion in the neck of femur 42 days after MM injection. Corticalis is marked as c which is destroyed (arrow) by MOPC-315.BM luc$^+$ cells marked with T. Original magnification 400X, scale bar is 200 µm. Insert: original magnification 200X, scale bar is 100 µm.

## 4.3.2 MOPC-315.BM luc$^+$ cells express receptors for bone marrow homing and retention

Based on the observed strong tropism of MOPC-315.BM luc$^+$ myeloma cells towards the hematopoietic compartment we asked whether these cells are characterized by a particular homing receptor profile that allows efficient recruitment to bone marrow niches. To this end we tested a panel of surface markers on MOPC-315.BM luc$^+$ cells extracted from the BM and

spleen of untreated mice 42 days after MM injection (n = 10, two independent experiments) **(Figure 14A)** in comparison to MOPC-315.BM luc^{+} cells maintained in tissue culture (n = 3, 4 independent measurements). As described in the Material and Methods section, gates were set according to the FMO method **(Figure 12A,B)**.
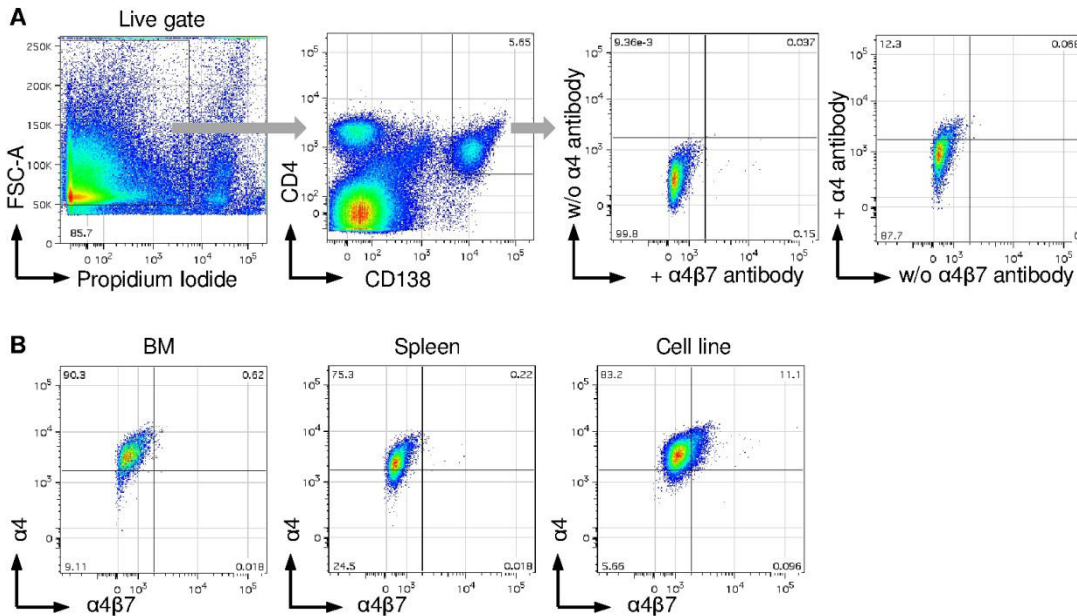


**Figure 12: Representative flow cytometry gating scheme according to the fluorescence minus one method (FMO). (A)** First, live cells were identified using propidium iodide staining. Within the live cells the gate for CD138^{+}CD4^{+} MM cells was set and applied to all samples within the measurement. Among those cells the quadrant gate for α4 and α4β7 was set according to the FMO method. The first FMO sample comprises all sampled antibodies except for α4 and the quadrant gate was set that α4 unstained cells appear in the α4 negative quadrant. This gate was applied to the FMO sample where only α4β7 staining is missing. The gate was adjusted that α4β7 unstained cells appeared in the respective negative quadrant. This FMO gate was applied to all further samples within the measurement. **(B)** Representative samples from BM, spleen and the cell line with applied FMO gates.

MOPC-315.BM luc^{+} cells as well as the original ATCC derived parental cell line MOPC-315 express constitutively the MM typical marker CD138 as well as CD4 **(Figure 13)** which is not found on normal B cells. This unique receptor combination was used to identify MOPC-315.BM luc^{+} cells.
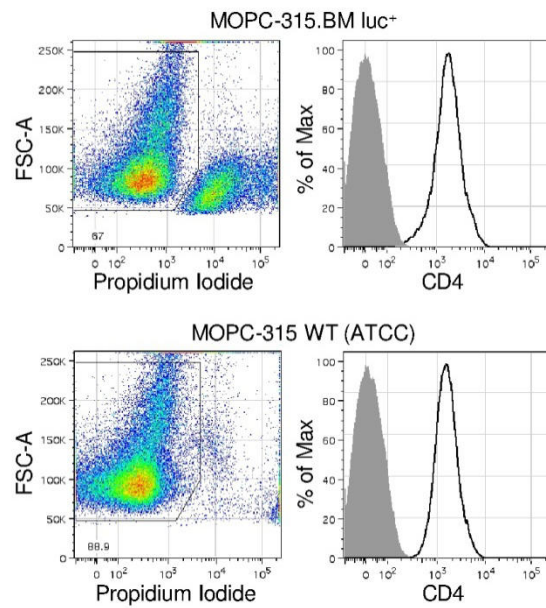
**Figure 13: CD4 expression of MOPC-315.BM luc⁺ and the wild type (WT) cell line.** MOPC-315.BM luc⁺ and MOPC-315 WT cells (obtained from ATCC) were stained for CD4. Only live cells as determined by propidium iodide staining were used for the analysis. Both cell lines clearly express CD4 to the same extent. Therefore, the constitutive CD138 and CD4 co-expression can be considered as a hallmark to uniquely identify these cells. Grey tinted histogram shows unstained luc⁺ or WT cells respectively, black histogram shows CD4 stained cells.

While 80 % of the original parent MOPC-315.BM luc⁺ cell line expressed α4β1 integrin, 91% of the MOPC-315.BM luc⁺ cells that homed and later were reisolated from the bone marrow and 73% of the cells reisolated from the spleen expressed α4β1 integrin ($p<0.05$) **(Figure 14B)**. The CXC chemokine receptor 4 (CXCR4) /SDF-1 interaction can lead to the upregulation of the integrin α4β1 which facilitates the transendothelial migration of MM cells into the BM[224,225]. CXCR4 has been identified as the sole receptor for SDF-1 which is constitutively produced by BM stromal cells. Through CXCR4 MM cells are attracted to the BM and retained there[225]. Of note, MOPC-315.BM luc⁺ cells down regulate CXCR4 in the spleen in comparison to MOPC-315.BM luc⁺ cells from BM ($p<0.05$) and cell culture ($p<0.01$) **(Figure 14C)**. Another surface marker associated with BM homing is CD44. This receptor mediates MM cell binding to hyaluronic acid on the BM endothelium supporting BM homing and invasion[226,227]. The overall expression of CD44 was found to be high in MOPC-315.BM luc⁺ cells *in vitro* or in different compartments *in vivo*. Yet, MOPC-315.BM luc⁺ cells in the BM expressed significantly higher CD44 levels than splenic MOPC-315.BM luc⁺ cells ($p<0.01$) **(Figure 14D)**.

CXCR4^{low} and CXCR4^{high} expressing MOPC-315.BM luc+ cells were tested for preferential homing to the spleen or the BM, which might explain the result shown in **Figure 14C**. We injected $5\times10^5$ of either CXCR4^{low} or CXCR4^{high} FACS sorted MOPC-315.BM luc⁺ cells into syngeneic mouse recipients (n = 4 each). Interestingly, when these two distinct populations

of CXCR4 expressing MOPC-315.BM luc$^+$ cells were maintained for 2 days in cell culture, both populations regained the initial CXCR4 expression profile **(Figure 14E)**. Consistent with that finding, after 10 days *in vivo*, non-invasive BLI **(Figure 14F)** showed that signals for both sorted populations were detected in both, the spleen and the BM compartment. Thus, the CXCR4 expression level of i.v. injected cells did not govern homing to the spleen or BM. However, *in vivo* BLI showed that the CXCR4$^{low}$ MOPC-315.BM luc$^+$ cells proliferated more than the CXCR4$^{high}$ cells. After BLI, animals were euthanized, and cells from the spleen, left femur/tibia bones, and right femur/tibia bones were harvested separately for flow cytometry analysis. The percentage and the absolute numbers of CD138$^+$CD4$^+$ were determined for each femur/tibia (= BM) and the spleen. The ratios of spleen/BM signals showed no difference in homing preference between CXCR4$^{low}$ and CXCR4$^{high}$ MOPC-315.BM luc$^+$ cells **(Figure 14G)**. This corroborated the *in vivo* BLI results. We also compared the MFIs of freshly sorted CXCR4$^{low}$ and CXCR4$^{high}$ MOPC-315.BM luc$^+$ cells with the MFI of MM cells extracted from femur/tibia and from the spleen 10 days after injection **(Figure 14H)**. Apparently, the CXCR4 expression at the time of i.v. injection is dynamically changed after residing 10 days in the hematopoietic compartment of the host mouse.

Other homing receptors were studied such as α4β7 integrin and we found it expressed on around 10% of MOPC-315.BM luc$^+$ cells *in vitro* but not on cells *in vivo* **(Figure 15A)**. Moreover, as MOPC-315.BM luc$^+$ cells homes efficiently into the spleen we tested the expression of CD62L and CCR7 as those receptors are important for homing into secondary lymphoid organs. CD62L expression while not expressed on the MOPC-315.BM luc$^+$ cells prior to injection was found to be increased in cells from the spleen but not on BM cells **(Figure 15B)**. Yet, CCR7 was not expressed **(Figure 15C)**. CXC chemokine receptor 3 (CXCR3) and CC chemokine receptor 2 (CCR2) were reported to be important for MM progression and dissemination[228] as well as BM homing[229]. However, these receptors were not found on the cells analyzed **(Figure 15D,E)**.
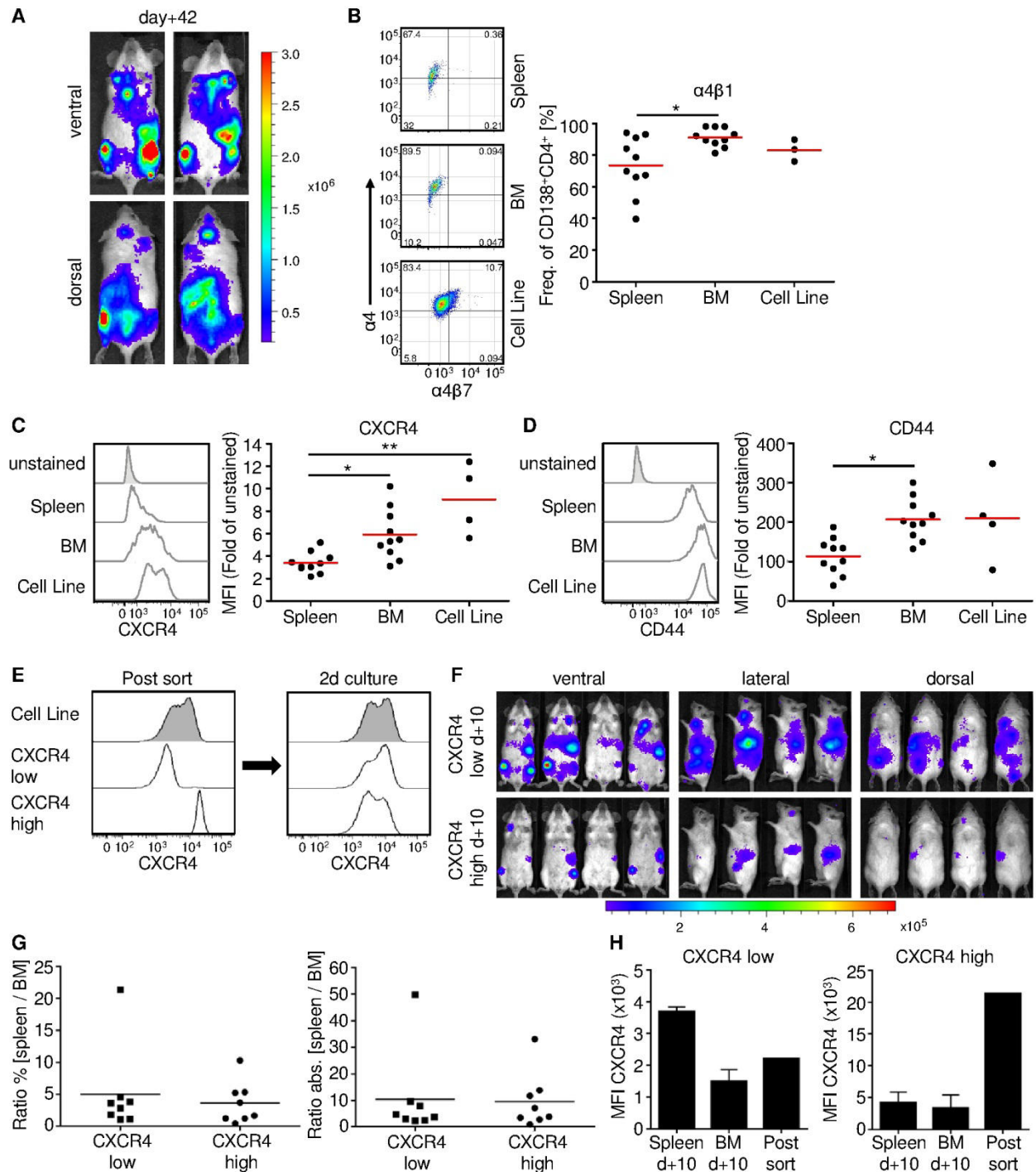
**Figure 14: Flow cytometry measurement of surface receptors associated with BM homing and infiltration of myeloma cells.** BALB/c wild type mice were injected with 1x10^{5} MOPC-315.BM luc^{+} cells via the tail vein. **(A)** 42 days after MM injection mice showed high BLI signals from hematopoietic compartments such as femur/tibia and spleen. Shown are two representative mice from ventral and dorsal view immediately before cells from BM and spleens were harvested for flow cytometry. **(B-D)** Besides BM and spleen derived MM cells, we also analyzed MOPC-315.BM luc^{+} cells from culture. Dead cells were excluded by propidium iodide staining and MOPC cells identified as CD138^{+}CD4^{+} double positive cells. **(B)** α4β1 integrin positive MOPC-315.BM luc^{+} cells were identified by flow cytometry as α4^{+} (CD49d^{+}) and α4β7^{-}. Shown are representative FACS plots and the corresponding graph stating the frequency within CD138^{+}CD4^{+} MOPC-315.BM luc^{+} cells expressing α4β1. For CXCR4 **(C)** and CD44 **(D)** representative histograms for each organ and cell line, including unstained fluorescence minus one (FMO) sample are displayed. Corresponding graphs state the fold difference in mean fluorescence intensity (MFI) related to the unstained FMO sample. BM and spleen: two independent experiments, n = 10, cells from cell culture: n = 4 for CXCR4 and CD44, n = 3 for α4β1. * indicates p<0.05 and ** indicates p<0.01 as determined by Kruskal-Wallis test with Dunn post test. **(E)**

MOPC-315.BM luc^{+} cells were sorted for CXCR4^{low} and CXCR4^{high} expression. After 2 days in cell culture sorted cells regained the original CXCR4 expression level of the cell line. **(F)** $5 \times 10^5$ sorted cells were i.v. injected into 4 female BALB/c mice each and BLI from ventral, lateral and dorsal was performed 10 days later. Sorted CXCR4^{low} as well as CXCR4^{high} CXCR4 cells readily homed to the BM compartment as well as to the spleen. **(G)** After BLI the mice were sacrificed, cells from left and right femur/tibia (separately) and the spleen extracted, and % as well as absolute numbers for CD138^{+}CD4^{+} MM cells determined. From these values a ratio of spleen / BM was calculated to determine the homing capacity of the sorted populations. **(H)** Comparison of CXCR4 expression levels of low and high sorted cells immediately before injection and MM cells from BM and spleen after 10 days *in vivo* reveals a dynamic CXCR4 regulation.
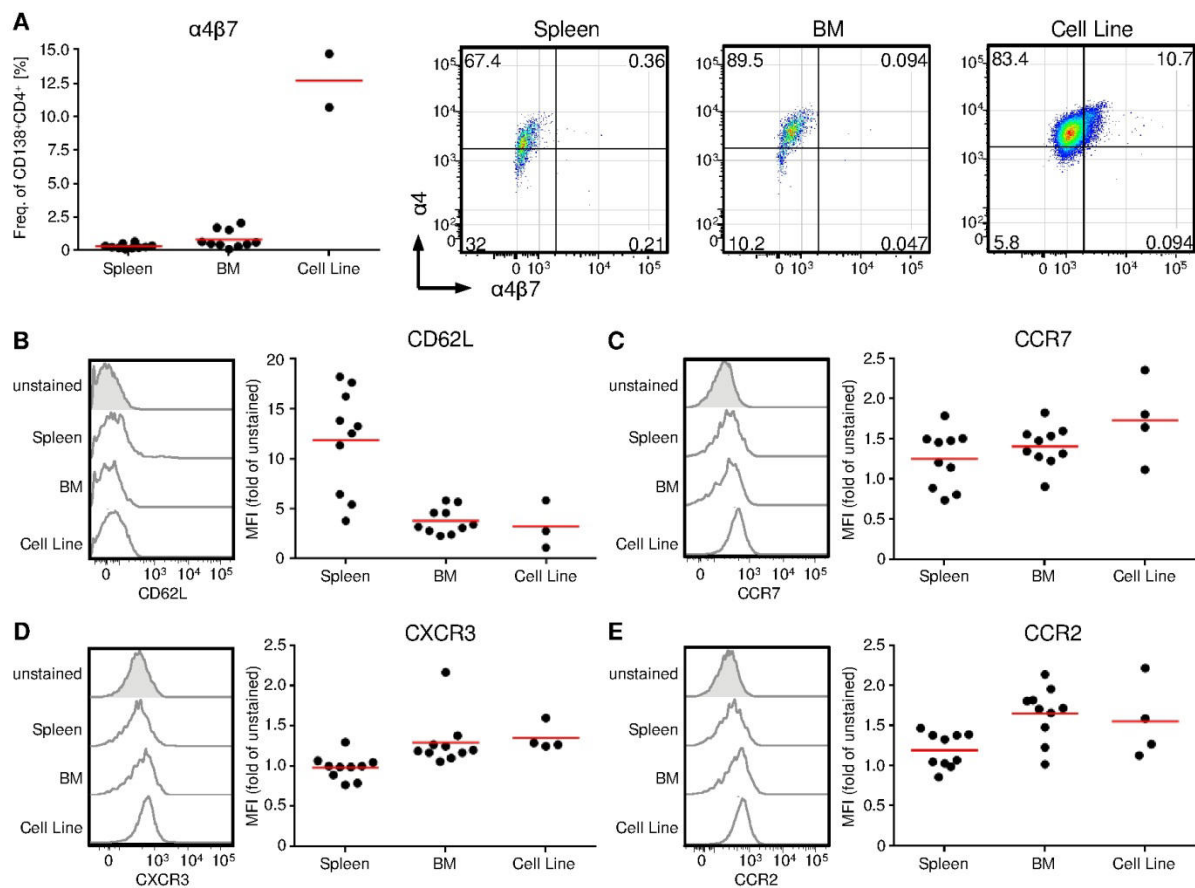


**Figure 15: Flow cytometry measurement of surface receptors associated with BM homing and infiltration of myeloma cells.** MOPC-315.BM luc^{+} myeloma cells were either directly taken from cell culture or extracted from BM and spleen as indicated and identified as CD138^{+}CD4^{+} double positive cells. α4β7 integrin positive MOPC-315.BM luc^{+} cells were identified by flow cytometry as α4^{+} (CD49d^{+}) and α4β7^{+} double positive. Representative quadrant gates or histograms for each organ and cell line, including unstained fluorescence minus one (FMO) sample are shown. Graphs state the frequency within CD138^{+}CD4^{+} MOPC-315.BM luc^{+} cells expressing α4β7 **(A)** or fold difference of mean fluorescence intensity (MFI) values of CD62L **(B)**, CCR7 **(C)**, CXCR3 **(D)** or CCR2 **(E)** in relation to the unstained FMO sample.

### 4.3.3 Attenuation of myeloma disease progression in mice treated with melphalan

To test if changes in tumor load can be reliably detected by *in vivo* imaging in this mouse model, we decided to treat tumor bearing mice with the alkylating agent melphalan, which is a well established treatment for patients with MM[136,230]. Since the melphalan was dissolved in ethanol we included a vehicle control group (ethanol only) in addition to untreated controls. We started the treatment 19 days after the MOPC-315.BM luc$^+$ cell injection when disease was fully established in all animals. This time point was designated as day 0 of treatment. Mice were consecutively treated with melphalan on days 0, 3, 7 and 11 and sacrificed for histology on day 14 **(Figure 16A)**. Two representative animals per group are shown from ventral and dorsal view, immediately before the first treatment (day 0), on day 7 and immediately before sacrificing the animals for subsequent histopathological examination (day 14) (melphalan n = 9, vehicle control n= 13, untreated control n = 14, 3 independent experiments) **(Figure 16B)**. BLI signals markedly increased in vehicle controls and untreated animals as compared to melphalan treated mice where the BLI signal intensity remained low. The signal quantification for ventral and dorsal view **(Figure 16C)** showed a significant difference between melphalan treated mice vs vehicle control or vs untreated animals starting on day 10 of treatment for both, ventral (untreated vs melphalan p<0.0001, vehicle vs melphalan p=0.0032) and dorsal (untreated vs melphalan p=0.0006, vehicle vs melphalan p=0.0024). When comparing vehicle and untreated mice no differences were found.

Besides strong local signal increase in both control groups also new skeletal tumor foci from disseminating MM cells were visible while in melphalan treated mice local signal increase as well as MM dissemination was reduced **(Figure 16B)**. Indeed, when counting visible skeletal tumor spots immediately before treatment (day of treatment 0) and on day of treatment 14, in both control groups all mice showed a considerably increased number of foci. In contrast, some melphalan treated mice showed a rather moderate increase while in others no new dissemination or even a reduction of tumor foci was found **(Figure 16D)**. Two mice from the untreated control group developed paralysis of the hind legs 30 and 32 days after injection of MOPC-315.BM luc$^+$ cells due to tumor growth in the spine which resulted in compression of nerves.
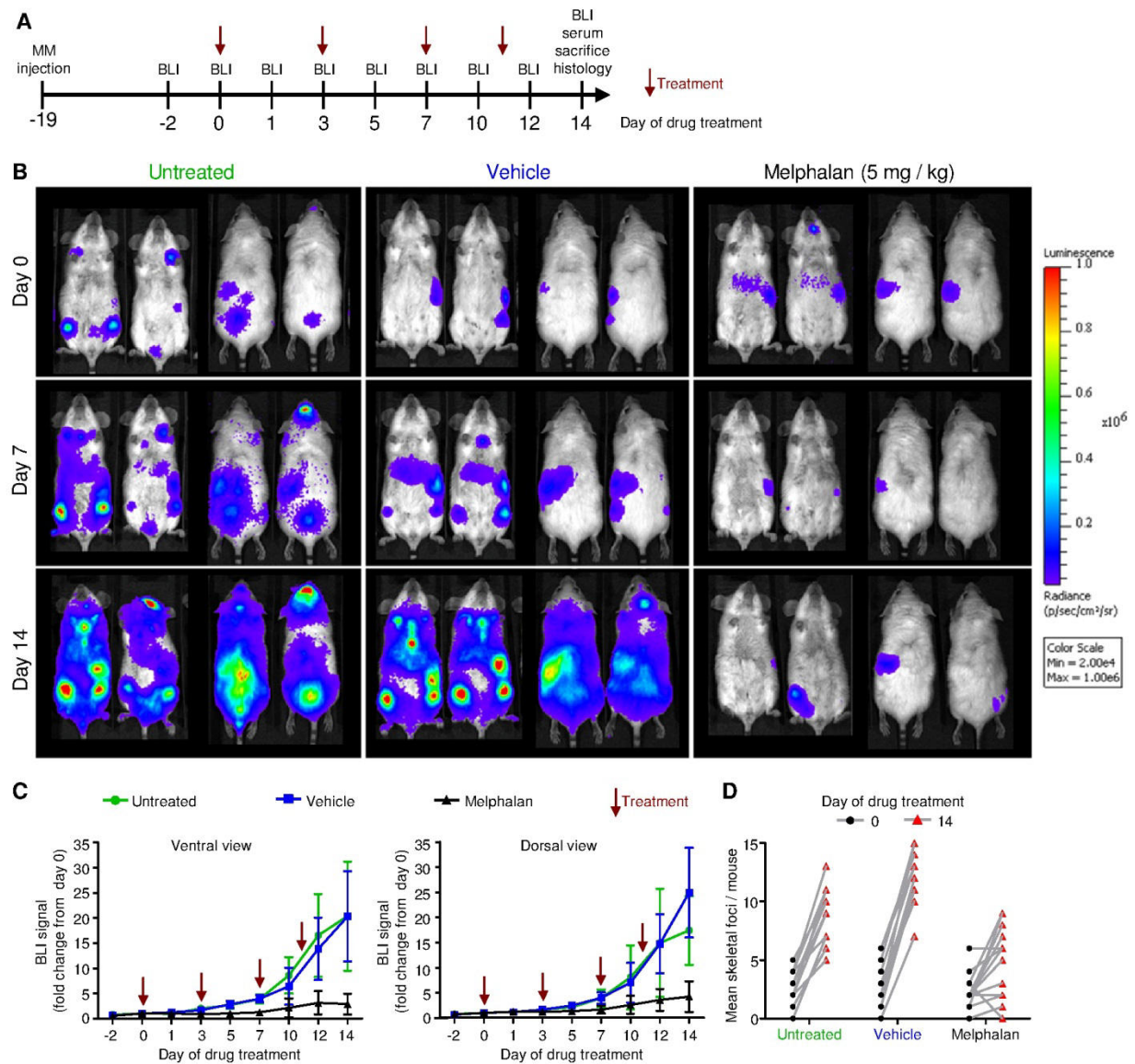
**Figure 16: Detection of residing MOPC-315.BM luc^{+} cells and *in vivo* monitoring of reduced myeloma progression due to melphalan treatment.** BALB/c wild type mice were injected with $1x10^5$ MOPC-315.BM luc^{+} cells via the tail vein. On day +19 after inoculation, tumors were established in all mice and readily detected by BLI. Then treatment was started (= day 0 of treatment). Mice received 5 mg/kg melphalan (n = 9, two independent experiments) or mock treatment (vehicle control, n = 13, three independent experiments) intraperitoneally. One control group of MOPC-315.BM luc[+] tumor bearing mice did not receive any treatment (untreated control, n = 14, three independent experiments). **(A)** Schematic study design, indicating treatment time points in respect to time after MM injection and end of experiment. Red arrows pinpoint melphalan treatment. **(B)** BLI images of two representative mice per group at selected time points in ventral (left) and dorsal (right) view. **(C)** Quantification of bioluminescence signal intensities over time from ventral or dorsal. Signals at day +19 were set as starting point and the following measurements were calculated as fold change of this initial signal intensity. Mice were treated at time points as indicated by arrows. Significant difference between melphalan treated mice vs vehicle control or vs untreated animals starting on day 10 of treatment for both, ventral (untreated vs melphalan p<0.0001, vehicle vs melphalan p=0.0032) and dorsal (untreated vs melphalan p=0.0006, vehicle vs melphalan p=0.0024). **(D)** Quantification of skeletal tumor foci in untreated, vehicle control and melphalan treated mice on day 0 and 14 of drug treatment.

Next, we confirmed the localization of the *in vivo* detected BLI signals to prove that signals allocated to organs or bones truly derived from these areas and did not originate from any surrounding tissue. To this end mice were sacrificed at day +14 for *ex vivo* imaging to separately display organs emitting *in vivo* signals (liver, spleen and femur/tibia) and organs that did not show signals *in vivo* (lungs). Consistent with *in vivo* BLI signals localizing to liver, spleen and femur/tibia we detected signals from those organs also by *ex vivo* BLI **(Figure 17A)**. In contrast, the lungs which did not exhibit any signal by *in vivo* BLI showed a detectable signal when imaged *ex vivo* **(Figure 17A)**. As already visualized before by non-invasive BLI, organs from melphalan treated mice showed less signal compared to untreated and vehicle control animals when imaged *ex vivo* **(Figure 17B)**.
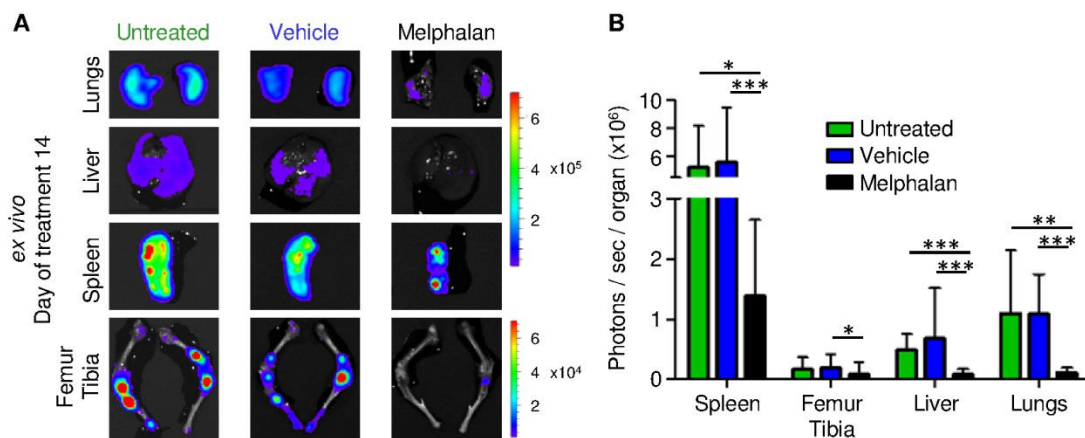


**Figure 17: Verification of *in vivo* signal localization by *ex vivo* BLI.** BALB/c wild type mice were injected with $1x10^5$ MOPC-315.BM luc$^+$ cells via the tail vein. 19 days after inoculation tumors were established in all mice and readily detected by BLI. Then treatment was started (= day 0 of treatment). Mice received 5 mg/kg melphalan or mock treatment (vehicle control) intraperitoneally. One control group of MOPC-315.BM luc$^+$ tumor bearing mice did not receive any treatment (untreated). Mice were sacrificed on day +14 of treatment and organs were prepared for *ex vivo* BLI. **(A)** Organs from one representative mouse per group are shown. *In vivo* BLI localization of signals from the liver, spleen and femur/tibia are confirmed. The signal from the lungs is only detected by *ex vivo* but not by *in vivo* BLI. Organs from the melphalan treatment group display lower signal intensities, indicating lower tumor burden when compared with untreated or vehicle controls. **(B)** Quantification of *ex vivo* signals (spleen n = 9-15, femur/tibia n = 9-15, liver n = 9-15, lungs n = 5-9; 2-3 independent experiments) shows significant differences between melphalan treated and untreated or vehicle control mice. Therefore, *ex vivo* BLI corroborates *in vivo* data as well as histopathological analysis of the response to melphalan therapy. * indicates p<0.05, ** indicates p<0.01, *** indicates p<0.001 as determined by Kruskal-Wallis test with Dunn post test.

### 4.3.4 Histological examination confirms *in vivo* BLI measurements of response to drug treatment

To resolve where MOPC-315.BM luc$^+$ cells reside exactly within organs and to confirm measured BLI signals on a cellular basis, histological sections from tumor bearing mice were evaluated by an experienced unbiased pathologist. The MOPC-315 luc$^+$ cells appeared morphologically distinct from other cell types in a hematoxylin and eosin (H&E) staining and therefore no additional specific tumor staining was needed **(Figure 18A)**. MOPC-315.BM luc$^+$

cells infiltrated spleen, femur and tibia (here referred to as BM), whereas myeloma cells in liver and lungs localized within blood vessels but did not invade tissues **(Figure 18A, magnified inserts and Figure 19A,B)**. From this we concluded that the weak *in vivo* BLI signals from the vascularized liver originated from circulating MM cells that passed through the organ during the signal acquisition. To verify the significant differences found by *in vivo* BLI between the three treatment groups single MM cells in liver and lung were counted. For spleens and BM we decided to determine the percentage infiltration of MM cells as the large amount of MM cells within these organs did not allow reliable counting of individual cells. Melphalan treated mice clearly presented less infiltration in spleen and BM as compared to both control groups **(Figure 18B)**. Counting MOPC-315.BM luc^{+} cells within the liver and lung vasculature we observed significant differences in treated mice and non-treated mice **(Figure 18C)**. This reduced circulation of MM cells in melphalan-treated mice might explain the reduced dissemination detected with *in vivo* BLI **(Figure 16D)**. The histological examination of the liver did not reveal any progressive disease in melphalan-treated mice. However, in the vehicle-treated group, liver infiltration was observed; in 2 out of 10 mice, very small tumors were found (less than 1 mm in diameter). In the untreated group, a liver tumor of 15 mm in diameter was observed in 1 of 9 animals. In quantifications of liver infiltration, histological liver data from the animals with liver tumors were excluded **(Figure 18C)**. Most likely, the melphalan treatment inhibited the formation of tumors in the liver.
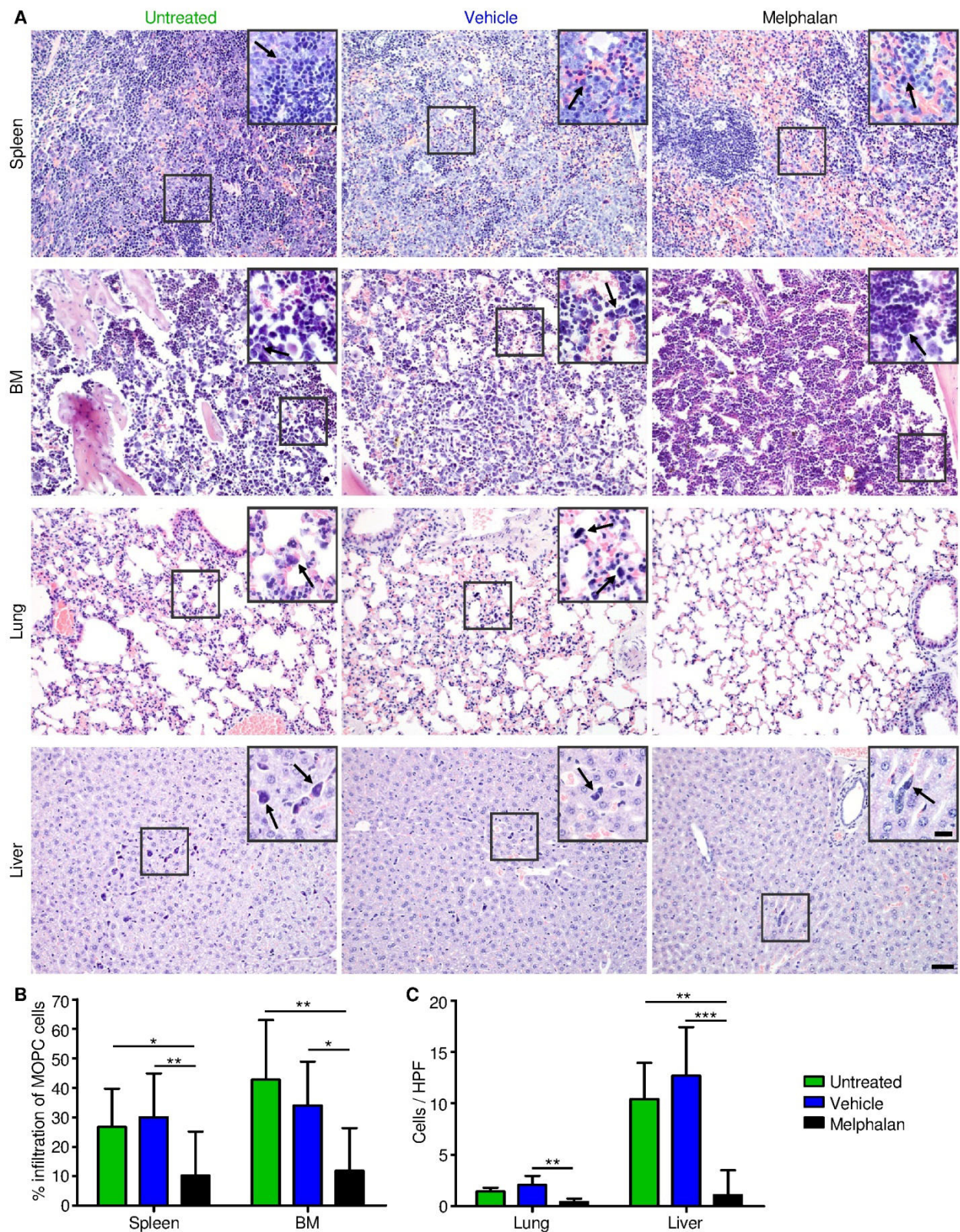
**Figure 18: Histopathological analysis of organs from melphalan, vehicle control treated and untreated mice confirms *in vivo* BLI data. (A)** Representative hematoxylin-eosin (H&E) stainings from organs harvested at day+33 after tumor inoculation from the different treatment groups. The hematopoietic compartments BM and spleen display clear infiltration of MOPC-315.BM luc^{+} cells, while MOPC-315.BM luc^{+} cells in lung and liver reside within the blood vessels as indicated by arrows. Scale bar is 50 µm for all shown sections (original magnification 200X / 0.70 NA) and 20 µm for inserts (original magnification 400X / 0.85 NA). **(B)** Determination of the percentage of MOPC-315.BM luc^{+} cells within BM and spleen and **(C)** number of cells per high power field (HPF) in lung and liver shows significant correlation with the melphalan treatment and thereby confirms *in vivo* and *ex vivo* imaging

data. * indicates p<0.05, ** indicates p<0.01, *** indicates p<0.001 as determined by Kruskal-Wallis test with Dunn post test.
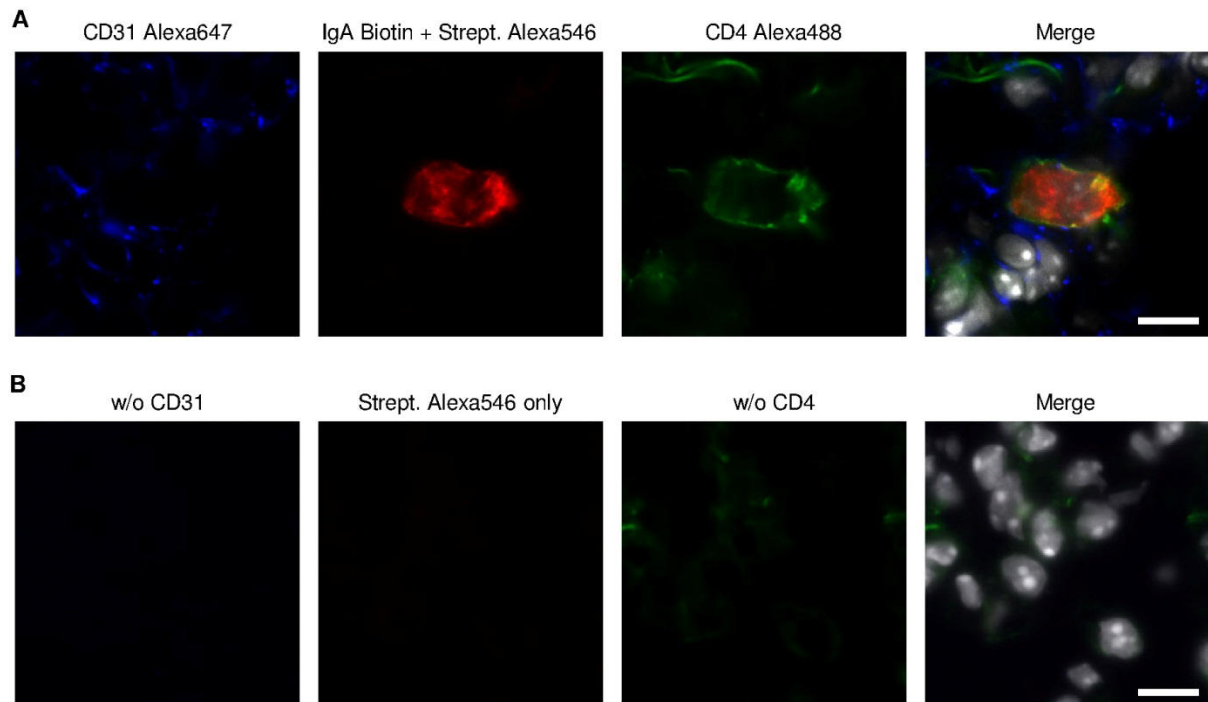


**Figure 19: CD31 staining verifies MOPC-315 localization inside blood vessels in the lung. (A)** Representative immunofluorescence staining of an IgA⁺CD4⁺ MOPC-315.BM cell within a pulmonary CD31⁺ vessel in the lung taken from untreated mice 33 days after MM injection. **(B)** Negative control staining, without CD31, IgA and CD4. Only secondary strepavidin Alexa546 and DAPI was added. Single color channels and merge including DAPI are shown. Blue – CD31, red – IgA, green – CD4, white – DAPI (nuclei). Scale bar is 10 µm. Original magnification 400x / 1.30 NA.

### 4.3.5 Serum M315 IgA levels additionally corroborate treatment response as measured by non-invasive BLI

As MOPC-315.BM luc⁺ cells secrete M315 IgA immunoglobulin[188] we decided to verify the non-invasive BLI data by ELISA. The measurement of MM derived Ig is widely used in mouse models to determine the tumor load[173,192]. We tested whether MOPC-315-idiotype-specific IgA (M315 IgA) correlated with tumor load after drug treatment. Both in vivo BLI and histology indicated significantly less tumor burden in melphalan-treated vs. vehicle-injected control mice. On day 14 of treatment, serum was collected from representative mice from the vehicle and melphalan treatment groups, and non-invasive BLI was performed in parallel **(Figure 16A)**. M315 IgA levels were significantly reduced in melphalan-treated mice (n = 5) compared to vehicle-treated control animals (n = 5) (two-tailed p-value 0.0171). This was supported by the simultaneously obtained in vivo BLI data, which showed a similar significant difference (two-tailed p-value 0.0221) **(Figure 20A)**.

We also monitored serum levels of specific M315 IgA in 5 untreated mice over an extended time period with simultaneous BLI measurements **(Figure 20B)**. In general M315 IgA correlated with BLI data as the 3 mice with higher BLI signal (ventral + dorsal) also showed higher M315 IgA levels **(Figure 20C-E)** while the two mice with lower total body BLI signal also had comparatively lower M315 IgA levels **(Figure 20F,G)**. In all 5 animals M315 IgA was clearly detectable on day +24 with steady increase until day +43 when the measurements were ended.

In mice the half-life for mainly monomeric IgA is 24 h[231] while in humans the half-life of monomeric serum IgA is considerably longer, up to 4-6 days[232]. Therefore, M315 IgA ELISA measurements might slightly overestimate the actual tumor load due to accumulation while BLI detects MM load in real time where accumulating events are abolished. Nevertheless, first BLI signals were detectable as early as day +9 after MM injection, while M315 IgA levels were still at background levels on day +9. This indicates a higher sensitivity for the detection of MM presence by BLI in this mouse model.
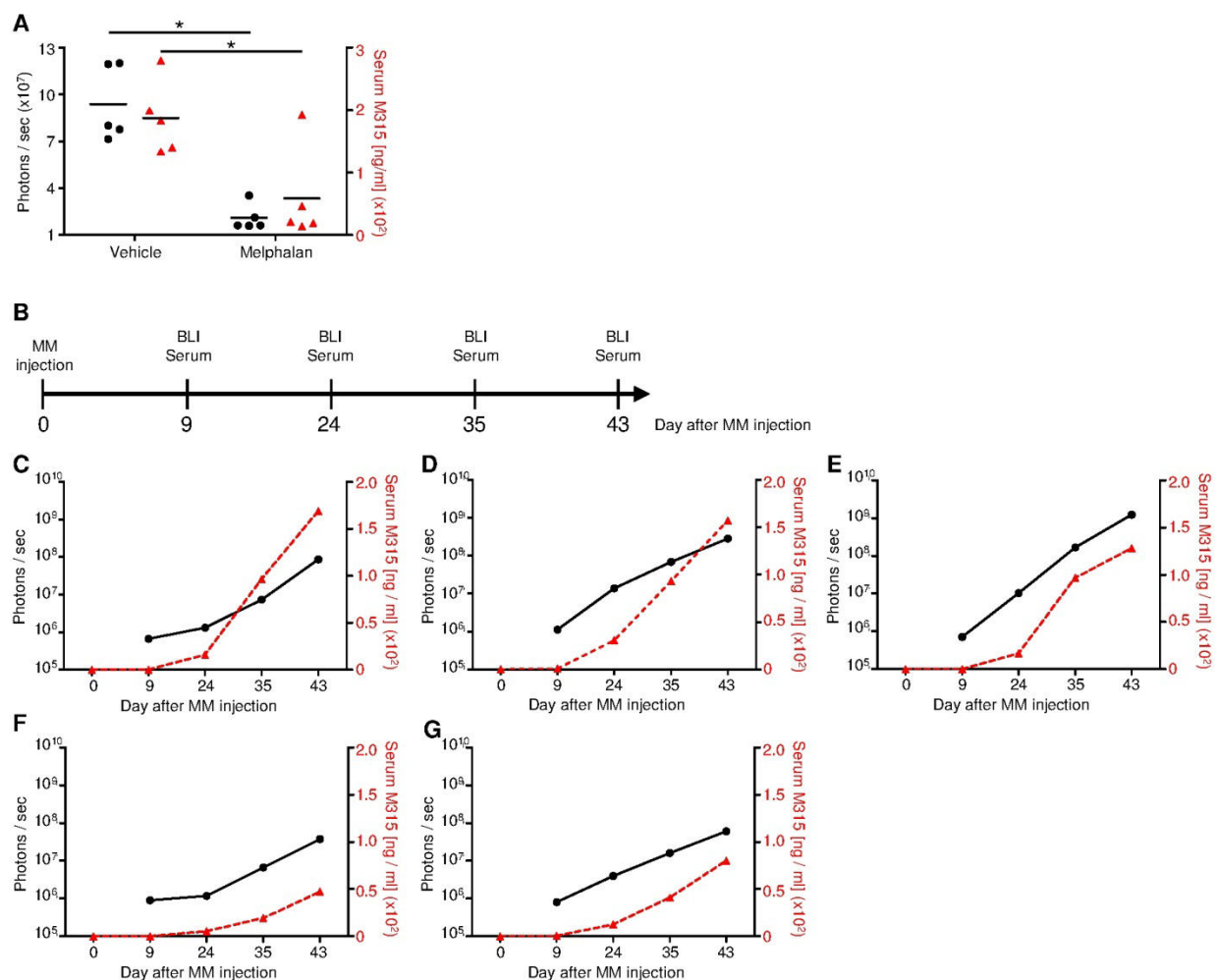


**Figure 20: Tumor detection by *in vivo* BLI correlates to M315 IgA serum measurement by ELISA.** Serum from mice was collected by bleeding. **(A)** M315 serum levels of melphalan treated (n = 5) and vehicle control (n = 5) on day 14 of treatment and simultaneous BLI measurement of the same

mice. Measurement of idiotype specific M315 IgA showed significant differences between the groups (two-tailed p value 0.0171) which was also found by BLI measurement (ventral + dorsal signal) (two-tailed p value 0.0221). **(B)** Scheme indicating time points for BLI measurement and serum collection for data presented in (C - G). **(C - G)** Idiotype specific M315 IgA serum levels of 5 untreated mice over time rises constantly with progression of tumor burden as measured by BLI (ventral + dorsal signal). Of note, BLI measurements provided signals in early disease stages starting from day +9, whereas M315 IgA levels were not detectable at this time point. BLI signal intensity (black circles, solid lines) displays to the left y-axis, serum M315 IgA (red triangles, dashed lines) displays to the right y-axis.

### 4.3.6 Flow cytometry measurements reinforce *in vivo* BLI measurements

Besides histology and M315 IgA detection we used a third independent method to verify the reliability of *in vivo* BLI data on MM tumor load. We investigated the percentage of MOPC-315.BM luc$^+$ cells in spleens and BM by flow cytometry. Subsequently, those data were correlated to the measured *in vivo* BLI signals arising from these compartments. The correlation between FACS and BLI in femur / tibia (Pearson r = 0.9817) was highly significant (p two tailed < 0.0001) as well as the correlation in the spleen (Pearson r = 0.9757, p two tailed < 0.0001).
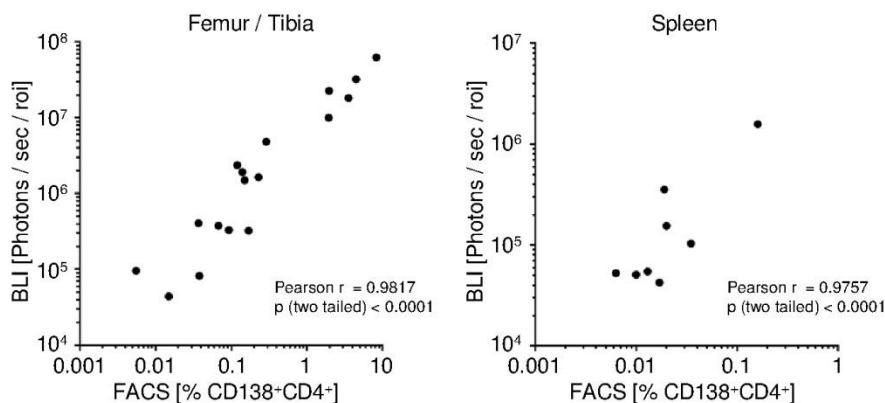


**Figure 21: *In vivo* BLI measurements strongly correlate with MM burden determined by flow cytometry in spleen and femur / tibia.** To additionally verify that non-invasive BLI data correlate with actual MM load we measured *in vivo* BLI signals from the spleen and femur / tibia and subsequently extracted cells from both organs for flow cytometry. MM cells were identified among living cells as CD4$^+$CD138$^+$. The measured percentage of MM cells in spleen or bone marrow compartments was correlated to measured BLI signals using a Pearson correlation. Femur / tibia: Pearson r = 0.9817, p (two tailed) < 0.0001; Spleen: Pearson r = 0.9757, p (two tailed) < 0.0001.

### 4.4 Advanced MM mouse model to achieve higher imaging sensitivity

### 4.4.1 MOPC-315 FUGLW cells are brighter than MOPC-315.BM luc$^+$

In order to advance the now established MOPC-315.BM luc$^+$ mouse model we generated MOPC-315 cells expressing an eGFP-luc fusion protein. Therefore, we lentiviral transduced MOPC-315 WT cells with the FUGLW vector and sorted the resulting cells twice for eGFP expression **(Figure 22A)**. The homogenous eGFP expression suggested that also the expression of luciferase is homogenous among MOPC-315 FUGLW 2x sort cells. To confirm

the expression of luciferase in those cells and to directly compare the brightness to the so far used MOPC-315.BM luc^{+} cells we titrated both cell lines in wells and measured the BLI signal intensities under equal conditions **(Figure 22B)**. For both cell numbers per well, FUGLW transduced cells emitted around 17-fold more photons per second than the MOPC-315.BM luc^{+} cells ($7.03 \times 10^7$ vs $4.11 \times 10^6$ and $3.27 \times 10^7$ vs $1.78 \times 10^6$) **(Figure 22C)**. Derived from these measurements we calculated the emitted photons per second of a single cell **(Figure 22D)**. One MOPC-315 FUGLW 2x sort cell emits 17.6 times more photons per second than one MOPC-315.BM luc^{+} cells that we had used so far. This enhanced brightness will be highly beneficial for the imaging sensitivity.
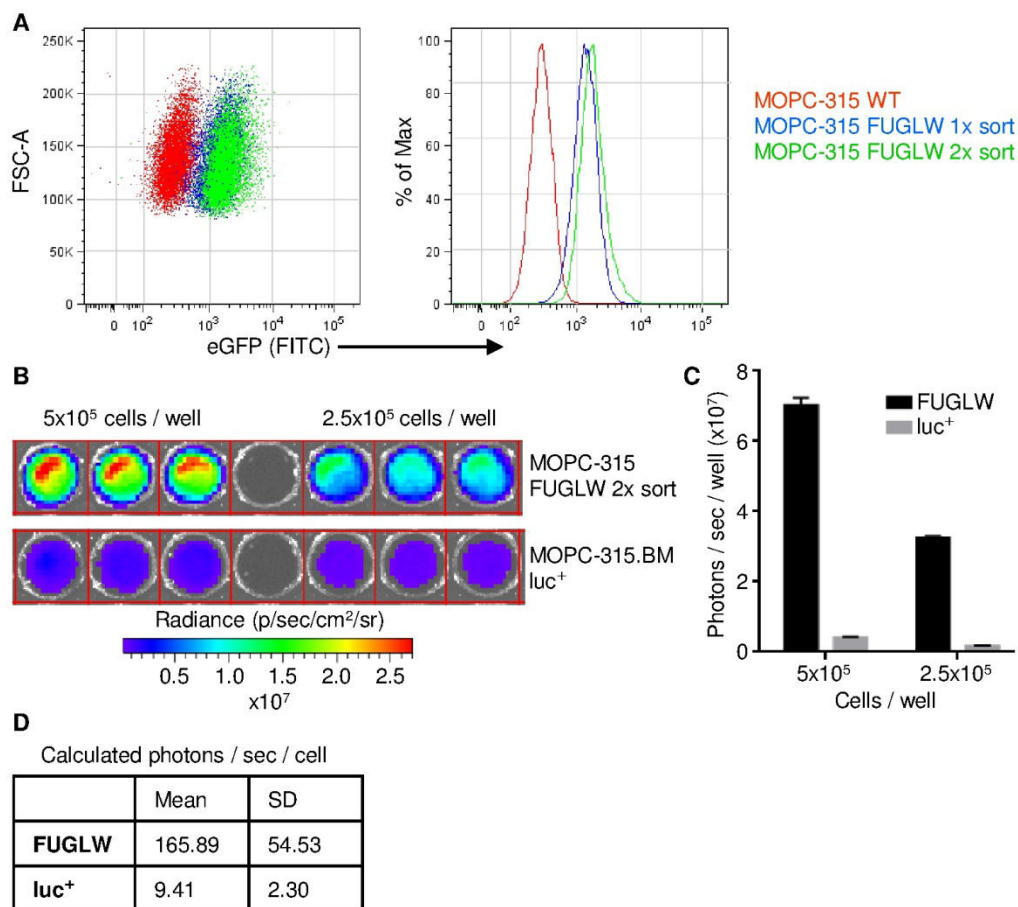


**Figure 22: Generation of the MOPC-315 FUGLW cell line.** MOPC-315 WT cells were lentivirally transduced using the FUGLW vector. The vector encodes an eGFP and firefly luciferase fusion protein. **(A)** After transduction, MOPC-315 FUGLW cells were FACS sorted twice for eGFP expression. **(B)** Comparison of luciferase expression levels of double sorted MOPC-315 FUGLW vs MOPC-315.BM luc^{+} cells. Indicated amounts of cells were plated into wells and photon emission was measured using the IVIS spectrum BLI imaging system. **(C)** Quantification of bioluminescence intensities per well. **(D)** Calculated photon emission per second per cell of MOPC-315 FUGLW and MOPC-315.BM luc^{+} cells based on measurements from B and C.

## 4.4.2   *In vivo* passaging of MOPC-315 FUGLW cells expedites MM disease progression

The twice sorted MOPC-315 FUGLW cells served as starting material for further improvements of the cell line. As the MOPC-315.BM luc$^+$ cells were established by several *in vivo* passages from the BM to ensure homogenous and efficient homing of MM cells to the BM, we also undertook this with our cell line. Therefore, MOPC-315 FUGLW cells were consecutively passaged through the BM of four host animals and designated MOPC-315 FUGLW BMP4. Next, addressed the effect of *in vivo* BM passaging and compared disease progress and MM cell homing of MOPC-315 FUGLW that had not been passaged, with MOPC-315 FUGLW BMP4 cells. To this end we injected 1x10$^5$ MOPC-315 FUGLW or MOPC-315 FUGLW BMP4 i.v. into syngeneic recipients. To additionally verify that the *in vivo* behavior of the cells was not influenced by the supplier specific BLAB/c mouse strain due to genetic drift, we also observed MOPC-315 FUGLW cells in BALB/c mice from Harlan.

11 days after MM injection both groups of mice who received non-passaged MM cells (Harlan n = 9; CR n = 10; one experiment) displayed BLI signals averaging at 3.6x10$^5$ to 4x10$^5$ photons/sec from ventral **(Figure 23A,B)** as well as dorsal **(Figure 23D,E)**. In comparison, mice who received *in vivo* passaged MM cells (n = 9; one experiment) showed a more than 30 fold higher BLI signal of around 1.3x10$^7$ photons/sec in ventral **(Figure 23C)** and dorsal view **(Figure 23F)**. In the further course of the experiment we observed in mice of both groups that had received non-passaged MM a comparatively slow MM progression in combination with reduced dissemination. There was a period without appreciable MM growth or spread for around 30 days. Between day 31 and 35 BLI signals from ventral and dorsal view started to increase and after day 42 MM growth further augmented **(Figure 23A,B,D,E)**. Notably, there were outliers in both groups of mice receiving non-passaged cells. In contrast, the group which had received the *in vivo* selected MM cells the BLI signal increased constantly and uniformly from the beginning on **(Figure 23C,F)**. This constant MM growth and subsequent spread was also reflected in the survival of the mice. The first mouse was euthanized due to paralysis 24 days after MM injection and the last one on day 35. This resulted in a median survival of 31 days for mice injected with MOPC-315 FUGLW BMP4 cells **(Figure 23G)**. However, mice injected with unselected MOPC-315 FUGLW cells had a significantly prolonged survival. 80 % of Charles River (CR) mice or 90 % of Harlan mice survived until the end of the experiment on day 83 **(Figure 23G)**.

Concerning the homing pattern, passaged as well as non-passaged cells had a strong tropism towards the hematopoietic compartment. In all three groups BLI signals from the bones such as femur/tibia and the spleen were observed. Independent of *in vivo* pasaging or not, all mice had to be humanely killed due to paralysis of the hind legs. Paralysis is a strong

indicator for MM growth in the BM compartment, in this case the spine. There, nerves were compressed by MM growth which finally lead to paralysis.

Thus, the *in vivo* passaging through the BM compartment did not lead to a different homing pattern but rather lead to faster and more aggressive progression of the disease. Especially during the first 31 days a considerably slower growth rate and less dissemination was detected in non-passaged than passaged cells. A possible explanation might be that the *in vivo* passaging selected for those cells that have high homing capacity and/or have the ability for a favorable interaction with their surrounding host cells. The difference in growth and dissemination between the passaged and no- passaged MOPC-315 cells was apparent in the early phase of the *in vivo* experiment. Therefore, it seemed likely that the intrinsic given receptor expression of the cell lines played an important role in the early phase of the disease. We compared MOPC-315 FUGLW with MOPC-315 FUGLW BMP4 and additionally MOPC-315 wt (each cell line was assayed in duplicates in two independent measurements) to identify possible influences of the lentiviral transduction process on the baseline receptor expression.

Programmed death 1 (PD-1, CD279) is an inhibitory receptor expressed on activated T cells which exerts its inhibitory function upon binding to its ligand PD-L1 (CD274) which expression is inducible on a variety of lymphoid and peripheral tissues[233]. A well known mechanism of different tumor types is the usage of this PD-1/PD-L1 axis to evade immunosurveillance. It has been shown in several mouse models, including MM, that expression of PD-L1 on tumor cells significantly enhanced tumor growth by inactivation of surrounding effector T cells[234–236] and in the case of MM also the modulation of natural killer (NK) cell mediated cytotoxicity[237]. Additionally, PD-L1 expression was found on a variety of human tumor samples and often correlated with poor clinical prognosis[233,238]. As this MM model is conducted in an immunocompetent mouse the evasion from immunosurveillance should be considered. The original wt cell line and the FUGLW transduced MOPC-315 line expressed on > 99 % of the cells PD-L1 resulting in a mean MFI of $6x10^3$ and $4.7x10^3$, respectively **(Figure 24A)**. The baseline expression of PD-L1 in MOPC-315 FUGLW BMP4 compared to wt cells was significantly lowered to a mean MFI of $3.4x10^3$. Also, it seemed that the transduction itself already negatively affected the expression **(Figure 24A)**. Markedly, the BMP4 cells with a clearly more aggressive growth pattern *in vivo* showed a reduced expression of PD-L1.

**A** MOPC-315 FUGLW (Harlan)

**B** MOPC-315 FUGLW (CR)

**C** MOPC-315 FUGLW BMP4 (CR)

**D** MOPC-315 FUGLW (Harlan)

d+14
d+31
d+54

0.2  0.4  0.6  0.8  1.0  x10$^7$

Photons / sec
10$^{11}$
10$^{10}$
10$^9$
10$^8$
10$^7$
10$^6$
10$^5$
11  14  18  21  24  27  31  35  42  54
Day after MM injection

**E** MOPC-315 FUGLW (CR)

d+14
d+31
d+54

*

0.2  0.4  0.6  0.8  1.0  x10$^7$

Photons / sec
10$^{11}$
10$^{10}$
10$^9$
10$^8$
10$^7$
10$^6$
10$^5$
11  14  18  21  24  27  31  35  42  54
Day after MM injection

**F** MOPC-315 FUGLW BMP4 (CR)

d+14
d+31     *    *         *         *
d+54  *    *    *    *    *    *    *    *    *

0.2  0.4  0.6  0.8  1.0  x10$^8$

Photons / sec
10$^{11}$
10$^{10}$
10$^9$
10$^8$
10$^7$
10$^6$
10$^5$
11  14  18  21  24  27  31  35
Day after MM injection

**Figure 23: *In vivo* bone marrow passaging of MOPC-315 FUGLW cells enhances disease progression.** BALB/c wild type mice were injected with $1x10^5$ MOPC-315 FUGLW or MOPC-315 FUGLW BMP4 cells via the tail vein. MM progression was regularly observed by BLI. To rule out influences on MM engraftment and progression caused by genetic drift of BALB/c sublines from different suppliers, mice from Charles River (CR) and Harlan were used as indicated (MOPC-315 FUGLW Harlan n = 9, MOPC-315 FUGLW CR n = 10, MOPC-315 FUGLW BMP4 CR n = 9). **(A-C)** Ventral view of all mice on timepoints after MM injection as indicated with corresponding graph of BLI signal quantification over time. **(D-F)** Dorsal view of all mice on timepoints after MM injection as indicated with corresponding graph of BLI signal quantification over time. Asterisk indicates death of animal due to paralysis. **(G)** Survival graph. Mice injected with *in vivo* passaged MOPC-315 FUGLW BMP4 show a significantly reduced survival compared to both groups where mice received non-passaged MM cells (Log-rank test with Bonferroni correction for multiple comparisons). Mice supplier origin did not influence the overall survival.

To check whether *in vivo* passaging favors cells with a high initial BM homing capacity we also observed receptors associated with this capability. As described before, CXCR4 is an important chemotactic receptor guiding cells through an BM stromal cell generated SDF-1 gradient towards the BM[225]. The original MOPC-315 ATCC (wt) cells expressed the highest amount of CXCR4 with a mean MFI of $2.8x10^3$ which was slightly, yet not significantly, lower in MOPC-315 FUGLW cells (mean MFI $2.1x10^3$). MOPC-315 FUGLW BMP4 showed the lowest CXCR4 baseline expression with a mean MFI of $1.2x10^3$ which was significantly lower compared to MOPC-315 wt cells **(Figure 24B)**. Similarly, as seen with the PD-L1 expression, the transduction of the cells seemed to have a slight effect on the receptor expression. The fact that MOPC-315 FUGLW BMP4 cells exhibited the lowest CXCR4 level but showed better growth *in vivo* **(Figure 23A-F)** fits with the previous observation that MOPC-315.BM luc$^+$ cells sorted for CXCR4$^{low}$ obviously proliferated faster after injection than CXCR4$^{high}$ sorted cells **(Figure 14F)**. We also investigated the $\alpha4\beta1$ integrin expression as this receptor can facilitate the transendothelial migration of MM cells into the BM compartment[224,225]. We found significantly more $\alpha4\beta1$ expressing MOPC-315 FUGLW BMP4 cells (mean 88 %) than MOPC-315 FUGLW (mean 70 %) while in the original wt cell line around 80 % of the cells were $\alpha4\beta1$ positive **(Figure 24C)**.
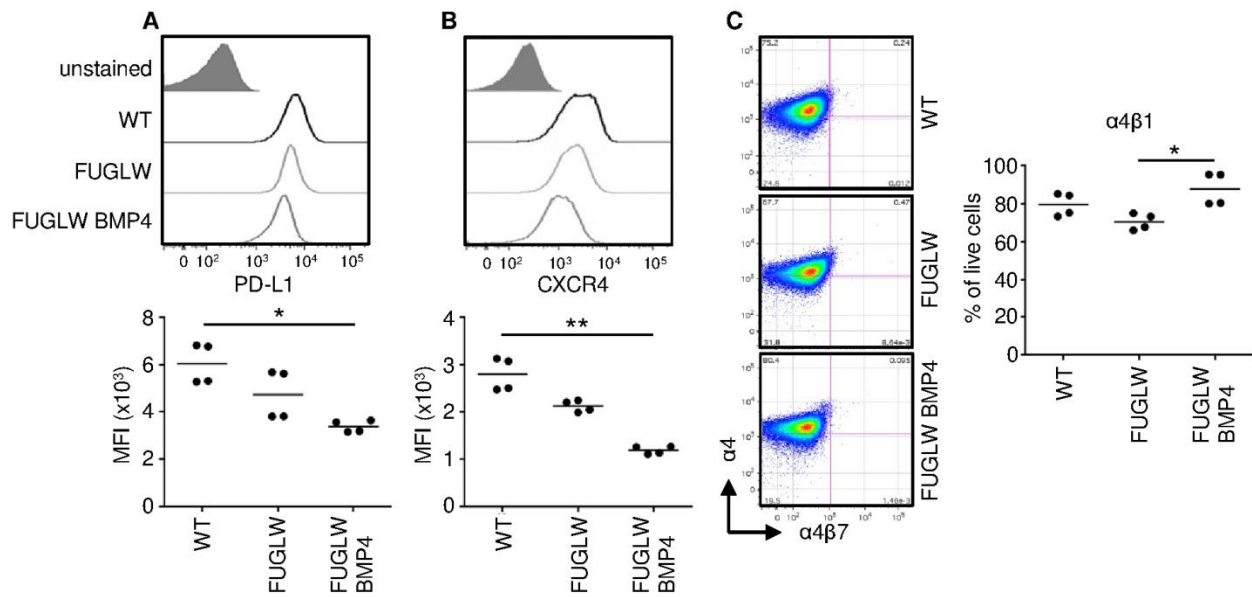
**Figure 24: Comparison of surface receptors associated with MM engraftment and immune evasion on MOPC-315 WT, FUGLW transduced and *in vivo* passaged cells.** To compare the influence of transduction and *in vivo* passaging on the expression of selected receptors, MOPC-315 wt, MOPC-315 FUGLW and MOPC-315 FUGLW BMP4 from culture were examined by flow cytometry (duplicates from two independent measurements). Dead cells were excluded by propidium iodide staining. For PD-L1 **(A)** and CXCR4 **(B)** representative histograms for each cell line including unstained fluorescence minus one (FMO) sample are displayed. Corresponding graphs below state the mean fluorescence intensity (MFI). **(C)** α4β1 integrin positive cells were identified as α4+ (CD49d+) and α4β7-. Shown are representative FACS plots and the corresponding graph stating the frequency within live cells expressing α4β1. * indicates $p<0.05$ and ** indicates $p<0.01$ as determined by Kruskal-Wallis test with Dunn post test.

### 4.4.3 Therapy with alkylating agents or a proteasome inhibitor attenuates MM progression *in vivo*

For the following experiments we used MOPC-315 FUGLW BMP4 as these cells showed a homogenous engraftment and disease progression *in vivo*. As done before with MOPC-315.BM luc+ cells, we tested the *in vivo* effects of melphalan treatment to verify the reliable detection of tumor load changes by BLI. Additionally, we expanded the treatment to another alkylating agent, cyclophosphamide, and the proteasome inhibitor bortezomib. Treatment time points and dosages were adopted from Chesi *et al.*[192], yet the melphalan dosage was kept at 5 mg / kg as in the experiments before. In these experiments we had not found differences between untreated and ethanol (vehicle) control mice **(Figure 16B,C)**. Therefore, a vehicle control group for this experiment using the MOPC-315 FUGLW BMP4 cells was omitted. 14 days after MOPC-315 FUGLW BMP4 injection the disease was fully established in all animals and we started the treatments. The treatment start was designated as day 0 and mice were treated with melphalan, bortezomib and cyclophosphamide i.p. from day 0 until day 11. One group of mice remained untreated (n = 9), melphalan (n = 5) was applied on days 0, 3, 7, 11, as well as bortezomib (n = 5), and cyclophosphamide (n = 5) on days 0, 2, 4, 8, 11 **(Figure 25A)**. After the treatment period, mice were regularly imaged for another

29 days to investigate the behavior of the recurring disease. All animals per group are shown from ventral **(Figure 25B)** and dorsal view **(Figure 25D)**, immediately before the first treatment (day 0), 2 days after the last treatment (day 13) and 10 days after treatment (day 21). Until day 13 the two alkylating agents melphalan and cyclophosphamide practically abolished further MM growth with only a mean BLI signal increase of 2 fold in ventral and dorsal view compared to day 0 **(Figure 25C,E)**. Both agents significantly inhibited MM growth compared to the untreated group from day 4 on (ventral: untreated vs melphalan $p = 0.0005$, untreated vs cyclophosphamide $p = 0.0001$; dorsal: untreated vs melphalan $p = 0.0048$, untreated vs cyclophosphamide $p = 0.0013$). Yet, 6 days after the last treatment the disease quickly reemerged in both groups and BLI signals from ventral and dorsal kept increasing until the end of the experiment **(Figure 25C,E)**. In contrast, BLI signals in bortezomib treated mice constantly increased by 112 fold from ventral and 212 fold from dorsal view until day 13. Nevertheless, at day 4 the ventral BLI signal was significantly lower than in untreated mice (untreated vs bortezomib $p = 0.0115$) and at day 10 ventral as well as dorsal signals were significantly lowered (ventral and dorsal: untreated vs bortezomib $p < 0.0001$) **(Figure 25C,E)**. The bortezomib treatment seemed to rather slow down the disease progress while melphalan and cyclophosphamide showed a significantly better therapy response at the end of the treatment period (day 10; ventral and dorsal: melphalan vs bortezomib $p < 0.0001$, cyclophosphamide vs bortezomib $p < 0.0001$). Despite this enhanced treatment response of the alkylating agents, the overall survival was not significantly prolonged to bortezomib treated mice. Melphalan and cyclophosphamide treated mice had a median survival of 46 days and bortezomib treated animals 39 days. Yet all three treatment groups had a significant survival advantage to untreated mice (median survival 31 days) **(Figure 25F)**.
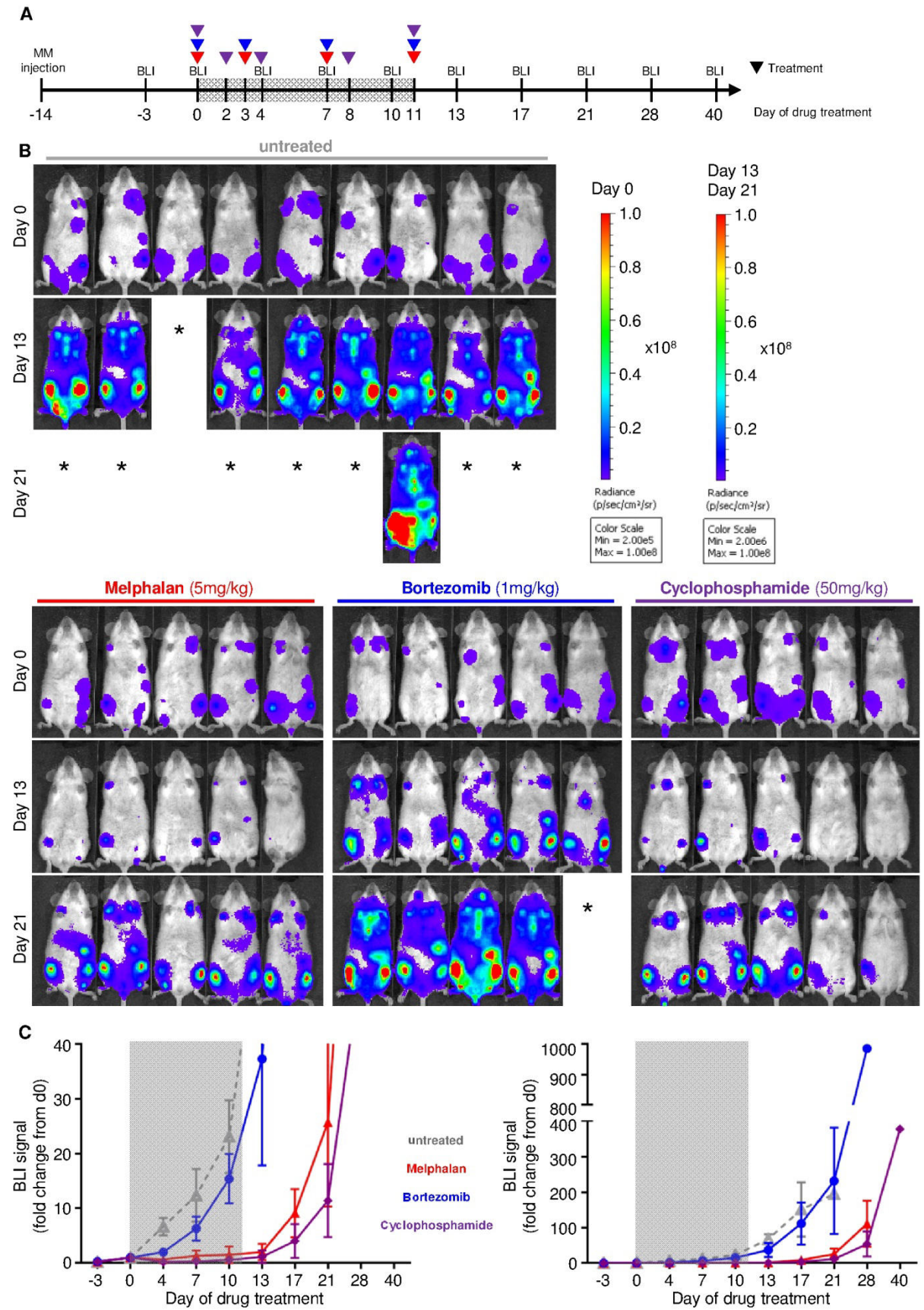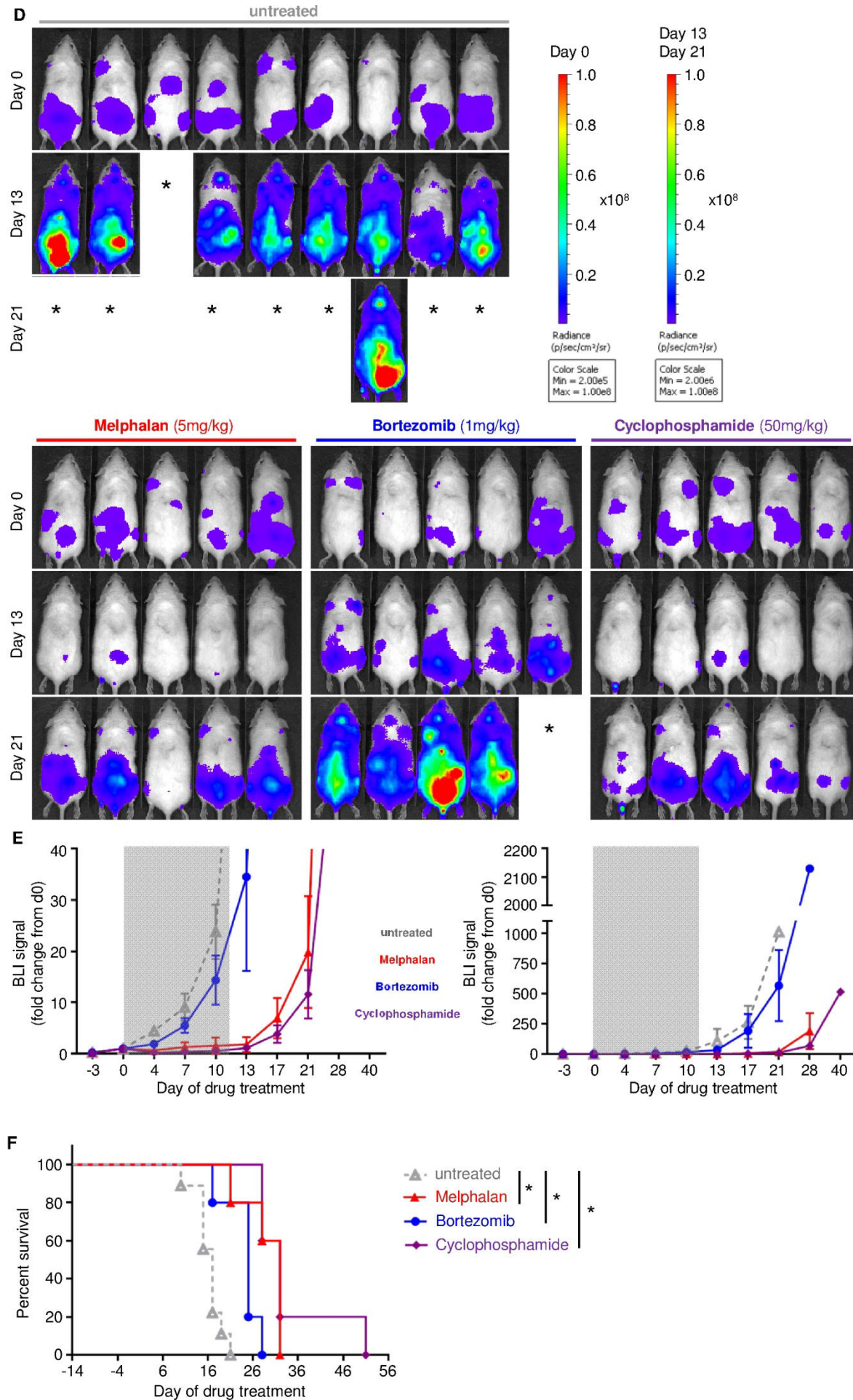
**Figure 25: Detection of residing MOPC-315 FUGLW BMP4 cells and *in vivo* monitoring of myeloma progression due to different treatment regimens.** BALB/c wild type mice were injected with $1\times10^5$ MOPC-315 FUGLW BMP4 cells via the tail vein. 14 days after inoculation, tumors were established in all mice and readily detected by BLI. Then treatment was started (= day 0 of treatment). Mice received treatments as indicated (n = 5, one experiment) intraperitoneally. One control group of MOPC-315 FUGLW BMP4 tumor bearing mice did not receive any treatment (untreated control, n = 9, one experiment). **(A)** Schematic study design, indicating treatment time points in respect to time after MM injection. Colored triangles pinpoint treatments (red = melphalan, blue = bortezomib, purple = cyclophosphamide). **(B)** BLI images of all mice per group at selected time points in ventral view. Asterisk indicates death of animal due to paralysis. **(C)** Quantification of bioluminescence signal intensities over time from ventral with smaller (left) and larger scale (right). Signals at day 14 were set as starting point (day 0) and the following measurements were calculated as fold change of this initial signal intensity. Significant difference between treated and untreated groups starts at day 4 (untreated vs melphalan p = 0.0005, untreated vs bortezomib p = 0.0115, untreated vs cyclophosphamide p = 0.0001) while between treatment groups no differences were calculated. By day 10 all treatment groups are significantly different from the untreated group (untreated vs melphalan p < 0.0001, untreated vs bortezomib p < 0.0001, untreated vs cyclophosphamide p < 0.0001). Between melphalan and cyclophosphamide treatment no difference is detected, yet both groups show a significantly better treatment result than bortezomib (melphalan vs bortezomib p < 0.0001, cyclophosphamide vs bortezomib p < 0.0001). **(D)** BLI images of all mice per group at selected time points in dorsal view. Asterisk indicates death of animal due to paralysis. **(E)** Quantification of bioluminescence signal intensities over time from dorsal with smaller (left) and larger scale (right). Signals at day 14 were set as starting point (day 0) and the following measurements were calculated as fold change of this initial signal intensity. Significant difference between treated and melphalan and cyclophosphamide groups starts at day 4 (untreated vs melphalan p = 0.0048, untreated vs cyclophosphamide p = 0.0013). By day 10 all treatment groups are significantly different from the untreated group (untreated vs melphalan p < 0.0001, untreated vs bortezomib p < 0.0001, untreated vs cyclophosphamide p < 0.0001). Between melphalan and cyclophosphamide treatment no difference is detected, yet both groups show a significantly better treatment result than bortezomib (melphalan vs bortezomib p < 0.0001, cyclophosphamide vs bortezomib p < 0.0001). **(F)** Survival graph. All three treatment groups showed significantly improved survival compared to untreated control animals (Log-rank test with Bonferroni correction for multiple comparisons). Between treatment groups no significant differences were detectable.

# 5  Discussion

## 5.1  The fluorescence protein FP635 "Katushka" for *in vivo* imaging applications

Non-invasive imaging offers the great opportunity to follow biological processes within the living organism in real-time. Yet, so far whole body FLI is limited by tissue autofluorescence and signal absorbance, especially occurring in the wavelength of commonly used FPs such as eGFP, RFP or DsRed[239–241]. To minimize those effects and thereby enhancing the imaging sensitivity many efforts have been undertaken to shift FPs beyond 600 nm where the "optical window" opens[17,18,242]. One of these FPs with an emission peak above 600 nm is FP635 "Katushka"[53]. FP635 has been described to exhibit superior brightness *in vivo* over other far-red, red and green emitting FPs such as GFP, mRFP (a DsRed variant), tdTomato, mRaspberry and mPlum[243]. These properties could make FP635 a good candidate as a single marker to combine whole body imaging with single cell microscopy. The possibility to track labeled cells in living animals over the whole spatial range from intact mice to cellular resolution can enhance the insights into the dynamics of HCT, GVHD and immune processes during GVT responses. Moreover, fluorescently labeled cells might be used in combination with luciferase tagged cells for the simultaneous detection of, for example, different immune cell populations or immune and tumor cells. Therefore, we evaluated FP635 under different conditions for its applicability in whole body imaging as well as 2-photon microscopy.

Under controlled *in vitro* conditions we challenged FP635 to DsRed-Monomer which emits in the red spectrum, and to eGFP, emitting in the green spectrum[4]. Here, we evaluated the signal attenuation caused by skin tissue and found indeed a wavelength dependency. Yet, the advantage of FP635 over the two other FPs was rather limited. A possible explanation for the only small advantage of FP635 might be found in the excitation wavelength. The excitation maximum of FP635 is at 588 nm[53] which is still in the range of strong attenuation by hemoglobin, melanin and other tissue components[4,18]. This might impede already the efficient excitation of FP635 and thus lower the advantage of an emission range beyond 600 nm. Notably, the signal of all three FPs was heavily attenuated by around 80% when covering the wells only with a thin piece of albino auricular skin and even around 90% when wells were covered with pinnae form C57BL/6 mice. These results clearly show the need for development in shifting FPs further towards the infrared spectrum such as the currently introduced FPs IFP 1.4[55] or iRFP[56].

To further investigate the applicability of FP635 for *in vivo* whole body imaging we generated a ubiquitin promoter driven FP635 tg mouse. Newborn mice exhibited clear whole body fluorescence and isolated PBMCs were detected with 2-log signal intensity above wildtype cells by flow cytometry. Notably, FP635 is not ideally detectable with standard BD Canto II

settings, nevertheless FP635 tg cells clearly separated from wt PBMCs. Similar expression levels in immune cells were reported in a previously published FP635 transgenic mouse[244]. Here, the detection of transgenic β-islets cells was possible using whole body *in vivo* FLI as well as in histology sections using a fluorescence microscope. Therefore, we believed that our FP635 transgenic mice would prove useful in whole body FLI as well as in 2P microscopy. Generally, it is believed that if the fluorescence intensity of a given cell measured by flow cytometry is around 2 units over background then cells are likely bright enough for detection by 2P microscopy[245]. So far, the *in vitro* advantage of FP635 in terms of signal attenuation was rather limited. To investigate the *in vivo* situation we challenged FP635 tg T cells against eGFP and DsRed-MST tg immune cells for 2PM detection in the spleen. This is a hemoglobin rich organ where signal attenuation is expected to be crucial. Surprisingly, FP635 had a similar performance to eGFP while DsRed-MST tagged cells showed superior detection sensitivity. Yet this result might not reflect the true physical performance of FP635. Cells for this experiment were derived from transgenic animals and eGFP as well as DsRed-MST tg cells showed a considerably higher relative brightness than FP635 tg cells. This very likely strongly biased the experimental findings.

Single cell detection of FP635 tg cells by 2P microscopy proved challenging, therefore we addressed the usability of those cells in whole body FLI of aGVHD. It is known that in this model, allogeneic T cells will accumulate and heavily proliferate in secondary lymphoid organs during initialization phase[24]. If a large amount of cells accumulate in one confined area, the fluorescence signals of the cells might add up and the individual cell brightness might become less important. As hair is known to heavily attenuate FP signals[60,246], we used nude mice for whole body imaging. Besides FP635 tg splenocytes we also transplanted DsRed-MST luc[+] double positive splenocytes. Whole body BLI of luc[+] tg immune cells was already shown to provide real-time information on aGVHD progression *in vivo*[24]. The detection of DsRed-MST splenocytes was possible only in LNs at timepoints where immune cells had undergone massive proliferation and accumulated at these sites. FP635 tg splenocytes on the contrary, were almost not detectable neither *in vivo* nor *ex vivo* during the whole experiment. Similarly, as seen in the 2p microscopy experiment, DsRed-MST tg cells were better detectable than the more red-shifted FP635 tg cells. Again, the lower relative brightness of FP635 tg immune cells is the major cause and shows, that the intrinsic brightness of the cells outcompetes possible advantages by FP wavelength. Overall, whole body FLI of both FPs clearly showed the limitations of fluorescence imaging in comparison to BLI. When imaging the double tg immune cells by BLI, we were able to detect transplanted splenocytes *in vivo* and *ex vivo* from day 2 on after transplantation. A major drawback for all experiments involving cells derived from the FP635 tg mouse line clearly is the missing relative brightness compared to other available FP transgenic mice. During breeding we

realized that the initial FP635 expression level of founder 3855 was not inherited in the same way to the offspring. Very likely the nonuniform inheritance of FP635 transgenes is a result of our strategy of lentiviral random insertion of the fluorescent transgene to generate these reporter mice. An unknown number of transgenes integrated into unknown DNA regions of the founder animals. Thus we screened the PBMCs of each individual offspring and chose stronger expressing animals for subsequent breeding. Yet, even after more than one year of breeding this did not result in a stable FP635 expressing mouse line. Breeding hemizygous FP635 transgenic with C57BL/6 wt mice for several generations did also not result in a stable mouse line but rather in decreased FP635 expression levels. Therefore, only a limited number of transgenic animals with acceptable FP635 expression was available for experiments. To avoid inhomogeneous inheritance, future transgenic mice should be generated by targeted insertion, for example into the ROSA26 locus. In combination with the CAG promoter this could also enhance the transgene expression level[247]. To overcome the limited brightness of transgenic immune cells, we generated FP635 tg MOSEC cells. Those cells grow rather superficially on the inside of the peritoneum and form solid tumor nodules. Those cells showed strong FP635 expression and thus were indeed detectable by non-invasive FLI. Yet, the sensitivity was limited to larger accumulations of tumor nodules and hairless areas only.

Altogether, it seems that FP635 presents slight advantages in terms of signal attenuation compared to eGFP and DsRed-Monomer and several publications report high brightness compared to other FPs *in vivo* at least partly owing to its far-red emission[53,68,243]. It remains arguable how the small differences in signal attenuation that we measured affect the detection sensitivity of FP635. Yet, the fast photobleaching of FP635 compared to the broadly established FPs DsRed and eGFP may be disadvantageous for long term microscopic tracking of cells. Our data show clearly that BLI remains by far superior over FLI in sensitivity and tissue penetration for whole body imaging of immune cells. BLI detection of luciferase tagged cells currently should be the first choice for non-invasive whole body imaging. The favorably good signal-to-background ratio allows sensitive detection of cells in the living organism, while whole body FLI often suffers from high unspecific autofluorescence due to the necessity of external excitation light[7,8]. Therefore, rather spectrally distinct luciferases should be employed to track different immune cell populations within the same animal. Such luciferases are available and have been shown to simultaneously distinguish at least two cell populations[22]. To additionally facilitate single cell resolution using microscopy techniques, cells may express a selected FP besides the luciferase. With such an "dual approach", the advantages of whole body BLI and single cell fluorescence microscopy techniques are combined. However, FLI of red or far-red clonally selectable tumor cell lines

may provide a welcome color addition to study immune cell-tumor interactions in combined HCT models of BLI and FLI.

## 5.2 The MOPC-315 based syngeneic MM mouse model for non-invasive imaging

We present a reliable and highly reproducible orthotopic *in vivo* multiple myeloma mouse model that can facilitate preclinical drug testing. Moreover, due to hosts with a complete and unmanipulated immune system, we believe that in the future this model will be also suitable for the study of immune cell – tumor cell interactions in various settings such as graft-versus-myeloma effects after allogeneic stem cell transplantation. In order to accomplish sensitive and non-invasive monitoring of tumor growth and localization we established the model by intravenous injection of luciferase labeled MOPC-315 cells into syngeneic recipients. Based on our previous experiments on the application of FP tagged cells for whole body FLI we decided to use luciferase tagged cells for this mouse model. The non-invasive detection of luc^{+} cells by BLI proved superior in terms of sensitivity compared to any FP tagged cell. Moreover, several studies have already demonstrated the strong correlation between the non-invasively detected BLI signal and the actual tumor load as specified by traditional methods such as serum markers or histopathology[35,36]. To verify that *in vivo* BLI is a reliable method also in this MM mouse model we treated MM bearing mice with melphalan. This alkylating agent is the treatment of choice for MM patients and has been in use for decades. Additionally, a clear single-agent activity has been shown for melphalan[115,116,121]. We showed, that *in vivo* BLI measurements differ between treated and non treated groups. Non-invasive BLI data were validated by *ex vivo* BLI, histology, serum M315 levels and flow cytometry. Through the usage of bioluminescence imaging we were able to visualize emerging tumor foci with the possibility to quantify the growth of single spots within the whole mouse. This aspect is important as this technique allows not only to measure the impact of a therapy on the overall tumor burden but also allows to detect the effect on single foci which can differ in size and tumor mass.

The presented MM mouse model reflects several key features of the human disease including osteolytic lesions, typical localization in the hematopoietic compartment, multifocal growth, active dissemination and immunoglobulin secretion. Such features may qualify this model for the evaluation of drugs targeting either MM cells directly or modulate their microenvironment. These include hypoxia, where the blockade of the hypoxia-inducible transcription factor-1 (HIF-1α) showed promising anti-MM effects[248] or the promising interference of angiogenesis in the BM environment[143]. Additionally, our results strongly implied that MOPC-315 cells retained plasticity. They could react to outside stimuli such as interaction with surrounding host cells and respond with dynamic receptor regulation. Several

receptors expressed by MOPC-315 cells are highly relevant in the human disease and are targeted by currently approved drugs. One example presents the CXCR4 inhibitor AMD3100[249,250]. These data indicate that MOPC-315 cells likely use similar receptors and pathways for BM infiltration, retention and dissemination as seen in the human disease. Yet further characterization of the cell line should be considered. Human MM shows a high heterogeneity with numerous immunoglobulin gene translocations, hyperdiploidy, mutations of RAS, p53, the NFKB pathway and very frequently, MYC rearrangements. This heterogeneity is not only seen between patients but also occurs during disease progression, resulting in constantly evolving MM cells[103,251]. The classification of the cell line to a certain subtype of human MM would clearly enhance the reliability of the model. If certain drugs, targeted at selected pathways or molecules, might lack response in this model it is important to know if the cause might be the specific MM subtype, not the drug itself. Clearly, neither MOPC-315 cells nor any other cell line can reflect the true human MM diversity[252], on the other hand the controlled and steady state of the cell line enhances reproducibility and provides standardized experimental conditions. Furthermore, this orthotopic model uses syngeneic MM cells in fully immunocompetent hosts. This setting reflects the human situation and highly enables the mouse model for the evaluation of immune system based anti-MM effects. It is known, that murine MM cells, including MOPC-315, express PD-L1 which is thought to downmodulate immune responses via interaction with PD-1 and render MM cells less susceptible to cytotoxic T-cells[235,236,253]. Also, the expression of PD-L1 in active human MM and various other cancer types has been associated with poor prognosis[233,238] and currently 6 experimental drugs targeting the PD-1/PD-L1 pathway are in clinical evaluation[254] (www.clinicaltrials.gov). Obviously, MM shares immune evasion characteristics with a variety of other tumors and insights found in this MM model might also be applied to other cancer types. Additionally, ongoing research in graft-versus-tumor effects after allogeneic HCT or the dysfunction of dendritic cells and other immune cell types in MM[255] will certainly benefit from this mouse model. Recently, MM has even been proposed as the ideal model to study the general mechanisms of cell trafficking and tumor metastasis[256] which would enhance the versatility of the MOPC-315 model beyond oncology research.

According to BLI and ELISA data, BM selected MOPC-315 cells quickly engraft within 7 – 9 days after i.v. injection and show fast proliferation and dissemination *in vivo*. Additionally, we observed sporadic extramedullary manifestation in the liver, lymph node or ther peritoneal cavity leading to ascites. These features prevalently mimic relapsed refractory or late stage human MM as observed in the clinics[257–259]. The aggressive disease phenotype was also emphasized by the fast MM recurrence of only around 4 days after alkylating drug treatment. In comparison, MOPC-315 cells that were not BM selected showed a slower *in vivo* proliferation and reduced dissemination which would rather resemble early MM stages. So

far, we have no explanation why and how the *in vivo* BM propagation of MOPC-315 cells leads to an enhanced aggressiveness. Yet, a similar phenomenon was observed by Chesi *et al.*[192] while probing their very elegant transgenic MYC MM mouse model for pre-clinical evaluation of drug activity. Mice spontaneously developing MM showed a disease progression, spread and drug response similar to early human MM stages. Although when they isolated the BM MM cells and reinjected them into syngeneic healthy recipients, the disease progression was strongly exacerbated including the occurrence of extramedullary manifestation and an altered drug response. Their conclusion was to use both models, to investigate the potential of drugs in both settings as some might be more beneficial in late stage/relapsed refractory disease and others may have their full potential in front-line therapy[192]. As an example they showed that vincristine and doxorubicin were able to stabilize disease in the more aggressive MM setting while in the less aggressive setting the drugs failed to show activity. Indeed, both drugs showed good clinical activity in relapsed refractory patients[260] while a conclusive effect in early MM treatment is missing[192]. So far the tested drugs on *in vivo* selected MOPC-315.BM luc$^+$ and MOPC-315 FUGLW BMP4 showed a strong anti MM response to the alkylating drugs melphalan and cyclophosphamide including prolonged survival in comparison to control mice. Both, melphalan and cyclophosphamide reportedly have a strong single agent activity[115,117] which is truthfully reflected by this model, nevertheless no lasting remission was induced. The treatment with the proteasome inhibitor bortezomib in turn showed rather modest response where the first two treatments slowed down MM progression and following treatments seemed without response. Yet, the survival of treated mice was slightly enhanced. These results hint to the proposed late MM stage behavior of selected MOPC-315 cells. Bortezomib as single agent was reported to induce a response rate of 35%[157] in patients with relapsed refractory MM but an even higher response rate of 77%[158] in newly diagnosed patients. Similarly, Chesi *et al.* reported a strong anti MM effect of single agent bortezomib in their transgenic MM mouse model, while in mice with transplanted MM cells (mimicking relapsed refractory MM) the effect was rather a slowdown of disease progression[192]. To confer this to the existing MOPC-315 model further experiments with the unselected and *in vivo* selected cells seem necessary to prove the idea of representing different stages of MM. This could include bortezomib treatment of mice bearing unselected MOPC-315 FUGLW cells to investigate whether in this setting the anti MM effect is truly enhanced. Additionally, treatments with MM drugs without proven clinical activity might be of importance. The model should carefully reflect the activity or inactivity of known MM drugs. This would be important, to consolidate the predictive value and clinical translation of experimental results for future new compounds.

Another interesting aspect is the elucidation of the effect on MOPC-315 cells during *in vivo* BM selection leading to the enhanced disease aggressiveness. We found on two different

occasions that a lowered CXCR4 expression level seems to enhance *in vivo* proliferation without affecting the BM homing capacity. Generally, high CXCR4 expression is linked with increased cell survival and proliferation[261,262]. Therefore, it might be interesting to investigate the status of known downstream signaling involved in CXCR4/SDF-1 binding such as mitogen-activated protein kinase kinase 1/2 (MEK1/2), p42/44 mitogen-activated protein kinase (MAPK) and Akt[249,261]. Another rather counterintuitive finding was the downregulation of PD-L1 expression levels in the more aggressive *in vivo* selected MOPC-315 cell line. It has been reported that PD-L1 expression on tumor cells can act positively on their growth by inactivating surrounding immune cells[234–236]. Yet, it is so far not clear whether the downregulation in this model might be just a bystander effect without true impact on *in vivo* proliferation. To elucidate this further experiments are needed to evaluate the importance of PD-L1/PD-1 interaction in this model. As currently several drugs targeting this pathway are in clinical trials[254], it might be worthwhile to test their effects in unselected as well as *in vivo* selected cells if there might be different outcomes and compare it to the clinical data.

Among the variety of available MM mouse models each model offers pros and cons depending on the research area and scientific question to be elucidated. In terms of pre-clinical drug testing it is of importance being able to introduce the tumor at the same time to a large number of experimental mice to gain meaningful statistical analysis. This holds a great benefit for a mouse model when the efficacy of a drug is being tested. This is rather difficult to achieve with xenograft models requiring primary human MM samples or spontaneously occurring MM models. Primary patient material is very likely limited and in transgenic MM models the time of disease onset is difficult to predict and in most also the exact disease subtype[201]. Additionally, xenograft models always rely on immunocompromised hosts and are often challenging in their setup[165,252]. Additionally, for pre-clinical drug testing the non-invasive detection of the MM cells can provide extensive spatiotemporal information on MM location and dissemination in the anatomical context and is therefore highly desirable. This feature clearly hints at the usage of a cell line based MM mouse model as cell lines can be readily labeled with luciferase or FPs with subsequent sorting or limited dilution methods in order to reach a homogeneously expressing cell population. These methods usually require *in vitro* culturing methods and are thus only limited applicable to primary material.

The MOPC-315 dependent MM mouse model presents a versatile platform for pre-clinical drug testing with reliable detection of disease progression and dissemination. The detection of MOPC-315.BM luc⁺ cells by BLI proved to be more sensitive than the widespread measurement of serum immunoglobulin. The detection sensitivity was further increased with MOPC-315 FUGLW cells which will be important for the assessment of minimal residual disease. Additionally, presumably unselected MOPC-315 FUGLW and *in vivo* BM selected MOPC-315 FUGLW BMP4 cells represent different stages of MM disease, thereby

enhancing testing capabilities for potentially new compounds. MOPC-315 cells are also applicable in a non-orthotopic subcutaneous model, where they recently helped to verify the *in viv*o activity of the potentially new target in MM treatment, namely the heat shock transcription factor 1[263].

Overall the presented MM mouse model is highly versatile, reliable, conveniently set up, mimics important features of the human disease, and provides real-time spatiotemporal information on disease progression and dissemination.

# 6 <u>References</u>

1.  Contag, C. H. & Bachmann, M. H. Advances in in vivo bioluminescence imaging of gene expression. *Annu Rev Biomed Eng* **4**, 235–60 (2002).

2.  Hillman, E. M. C. *et al.* In vivo optical imaging and dynamic contrast methods for biomedical research. *Philos Transact A Math Phys Eng Sci* **369**, 4620–43 (2011).

3.  Negrin, R. S. & Contag, C. H. In vivo imaging using bioluminescence: a tool for probing graft-versus-host disease. *Nat Rev Immunol* **6**, 484–90 (2006).

4.  Rice, B. W., Cable, M. D. & Nelson, M. B. In vivo imaging of light-emitting probes. *J Biomed Opt* **6**, 432–40 (2001).

5.  Troy, T., Jekic-McMullen, D., Sambucetti, L. & Rice, B. Quantitative comparison of the sensitivity of detection of fluorescent and bioluminescent reporters in animal models. *Mol Imaging* **3**, 9–23 (2004).

6.  Nakatsu, T. *et al.* Structural basis for the spectral difference in luciferase bioluminescence. *Nature* **440**, 372–6 (2006).

7.  Thorne, N., Inglese, J. & Auld, D. S. Illuminating insights into firefly luciferase and other bioluminescent reporters used in chemical biology. *Chem Biol* **17**, 646–57 (2010).

8.  De Wet, J. R., Wood, K. V, DeLuca, M., Helinski, D. R. & Subramani, S. Firefly luciferase gene : structure and expression in mammalian cells. *Mol Cell Biol* **7**, 725–37 (1987).

9.  Badr, C. E. & Tannous, B. A. Bioluminescence imaging: progress and applications. *Trends Biotechnol* **29**, 624–33 (2011).

10. Neill, K. O., Lyons, S. K., Gallagher, W. M., Curran, K. M. & Byrne, A. T. Bioluminescent imaging : a critical tool in pre-clinical oncology research. *J Pathol* **220**, 317–27 (2010).

11. Donat, S. *et al.* Surface display of Gaussia princeps luciferase allows sensitive fungal pathogen detection during cutaneous aspergillosis. *Virulence* **3**, 51–61 (2012).

12. Tannous, B. A. Gaussia luciferase reporter assay for monitoring biological processes in culture and in vivo. *Nat Protoc* **4**, 582–91 (2009).

13. Wurdinger, T. *et al.* A secreted luciferase for ex vivo monitoring of in vivo processes. *Nat Methods* **5**, 171–3 (2008).

14. Chung, E. *et al.* Secreted Gaussia luciferase as a biomarker for monitoring tumor progression and treatment response of systemic metastases. *PLOS ONE* **4**, e8316 (2009).

15. Bhaumik, S. & Gambhir, S. S. Optical imaging of Renilla luciferase reporter gene. *Proc Natl Acad Sci U S A* **99**, 377–82 (2002).

16. Bhaumik, S., Lewis, X. Z. & Gambhir, S. S. Optical imaging of Renilla luciferase, synthetic Renilla luciferase, and firefly luciferase reporter gene expression in living mice. *J Biomed Opt* **9**, 578–86 (2004).

17. Cheong, W. F., Prahl, S. A. & Welch, A. J. A review of the optical properties of biological tissues. *IEEE J Quantum Electron* **26**, 2166–85 (1990).

18. Weissleder, R. A clearer vision for in vivo imaging. *Nat Biotechnol* **19**, 316 – 317 (2001).

19. De Wet, J. R., Wood, K. V, Helinski, D. R. & DeLuca, M. Cloning of firefly luciferase cDNA and the expression of active luciferase in Escherichia coli. *Proc Natl Acad Sci U S A* **82**, 7870–3 (1985).

20. Sherf, B. A. & Wood, K. V Firefly luciferase engineered for improved genetic reporting. *Promega Notes* **49**, 14–21 (1994).

21. Zhao, H. *et al.* Emission spectra of bioluminescent reporters and interaction with mammalian tissue determine the sensitivity of detection in vivo. *J Biomed Opt* **10**, 41210 (2005).

22. Mezzanotte, L. *et al.* Sensitive dual color in vivo bioluminescence imaging using a new red codon optimized firefly luciferase and a green click beetle luciferase. *PLOS ONE* **6**, e19277 (2011).

23. Branchini, B. R., Magyar, R. A., Murtiashaw, M. H. & Portier, N. C. The role of active site residue arginine 218 in firefly luciferase. *Biochemistry* **40**, 2410–8 (2001).

24. Beilhack, A. *et al.* In vivo analyses of early events in acute graft-versus-host disease reveal sequential infiltration of T-cell subsets. *Blood* **106**, 1113–22 (2005).

25. Na, I.-K. *et al.* Concurrent visualization of trafficking, expansion, and activation of T lymphocytes and T-cell precursors in vivo. *Blood* **116**, e18–25 (2010).

26. Cao, Y.-A. *et al.* Shifting foci of hematopoiesis during reconstitution from single stem cells. *Proc Natl Acad Sci U S A* **101**, 221–6 (2004).

27. Pribaz, J. R. *et al.* Mouse model of chronic post-arthroplasty infection: noninvasive in vivo bioluminescence imaging to monitor bacterial burden for long-term study. *J Orthop Res* **30**, 335–40 (2012).

28. Burke, C. W. *et al.* Illumination of parainfluenza virus infection and transmission in living animals reveals a tissue-specific dichotomy. *PLOS Pathog* **7**, e1002134 (2011).

29. Jenkins, D. E. *et al.* Bioluminescent imaging (BLI) to improve and refine traditional murine models of tumor growth and metastasis. *Clin Exp Metastasis* **20**, 733–44 (2003).

30. Edinger, M. *et al.* Revealing lymphoma growth and the efficacy of immune cell therapies using in vivo bioluminescence imaging. *Blood* **101**, 640–8 (2003).

31. Nishimura, R. *et al.* In vivo trafficking and survival of cytokine-induced killer cells resulting in minimal GVHD with retention of antitumor activity. *Blood* **112**, 2563–74 (2008).

32.    Tuli, R. *et al.* Development of a novel preclinical pancreatic cancer research model : bioluminescence image – guided focal irradiation and tumor monitoring of orthotopic xenografts. *Transl Oncol* **5**, 77–84 (2012).

33.    Bolin, C. M., Sutherland, C., Tawara, K., Moselhy, J. & Jorcyk, C. L. Novel mouse mammary cell lines for in vivo bioluminescence imaging (BLI) of bone metastasis. *Biol Proced Online* **14**, 6 (2012).

34.    Bladé, J. *et al.* Soft-tissue plasmacytomas in multiple myeloma: incidence, mechanisms of extramedullary spread, and treatment approach. *J Clin Oncol* **29**, 3805–12 (2011).

35.    Poeschinger, T., Renner, A., Weber, T. & Scheuer, W. Bioluminescence imaging correlates with tumor serum marker, organ weights, histology, and human DNA levels during treatment of orthotopic tumor xenografts with antibodies. *Mol Imaging Biol* **ePub**, (2012).

36.    Klerk, C. *et al.* Validity of bioluminescence measurements for noninvasive in vivo imaging of tumor load in small animals. *Biotechniques* **43**, S7–S30 (2007).

37.    Prasher, D. C., Eckenrode, V. K., Ward, W. W., Prendergast, F. G. & Cormier, M. J. Primary structure of the Aequorea victoria green-fluorescent protein. *Gene* **111**, 229–233 (1992).

38.    Chalfie, M., Tu, Y., Euskirchen, G., Ward, W. W. & Prashert, D. C. Green fluorescent protein as a marker for gene expression. *Science* **263**, 802–5 (1994).

39.    Zhang, G., Gurtu, V. & Kain, S. R. An enhanced green fluorescent protein allows sensitive detection of gene transfer in mammalian cells. *Biochem Biophys Res Commun* **227**, 707–11 (1996).

40.    Heim, R., Prasher, D. C. & Tsien, R. Y. Wavelength mutations and posttranslational autoxidation of green fluorescent protein. *Proc Natl Acad Sci U S A* **91**, 12501–4 (1994).

41.    Ormö, M. *et al.* Crystal structure of the Aequorea victoria green fluorescent protein. *Science* **273**, 1392–5 (1996).

42.    Tsien, R. Y. The green fluorescent protein. *Annu Rev Biochem* **67**, 509–44 (1998).

43.    Matz, M. V *et al.* Fluorescent proteins from nonbioluminescent Anthozoa species. *Nat Biotechnol* **17**, 969–73 (1999).

44.    Baird, G. S., Zacharias, D. A. & Tsien, R. Y. Biochemistry, mutagenesis, and oligomerization of DsRed, a red fluorescent protein from coral. *Proc Natl Acad Sci U S A* **97**, 11984–9 (2000).

45.    Campbell, R. E. *et al.* A monomeric red fluorescent protein. *Proc Natl Acad Sci U S A* **99**, 7877–82 (2002).

46.    Living Colors™ DsRed2. *Clontechniques* **XVI**, 2–3 (2001).

47.    Bevis, B. J. & Glick, B. S. Rapidly maturing variants of the Discosoma red fluorescent protein (DsRed). *Nat Biotechnol* **20**, 83–7 (2002).

48. Shaner, N. C. *et al.* Improved monomeric red, orange and yellow fluorescent proteins derived from Discosoma sp. red fluorescent protein. *Nat Biotechnol* **22**, 1567–72 (2004).

49. Wang, L., Jackson, W. C., Steinbach, P. A. & Tsien, R. Y. Evolution of new nonantibody proteins via iterative somatic hypermutation. *Proc Natl Acad Sci U S A* **101**, 16745–9 (2004).

50. Vintersten, K. *et al.* Mouse in red: red fluorescent protein expression in mouse ES cells, embryos, and adult animals. *Genesis* **40**, 241–6 (2004).

51. Strongin, D. E. *et al.* Structural rearrangements near the chromophore influence the maturation speed and brightness of DsRed variants. *Protein Eng Des Sel* **20**, 525–34 (2007).

52. Merzlyak, E. M. *et al.* Bright monomeric red fluorescent protein with an extended fluorescence lifetime. *Nat Methods* **4**, 555–557 (2007).

53. Shcherbo, D. *et al.* Bright far-red fluorescent protein for whole-body imaging. *Nat Methods* **4**, 741–6 (2007).

54. Shcherbo, D. *et al.* Near-infrared fluorescent proteins. *Nat Methods* **7**, 827–9 (2010).

55. Shu, X. *et al.* Mammalian expression of infrared fluorescent proteins engineered from a bacterial phytochrome. *Science* **324**, 804–7 (2009).

56. Filonov, G. S. *et al.* Bright and stable near-infrared fluorescent protein for in vivo imaging. *Nat Biotechnol* **29**, 757–61 (2011).

57. Lin, M. Z. Beyond the rainbow: new fluorescent proteins brighten the infrared scene. *Nat Methods* **8**, 726–8 (2011).

58. Shaner, N. C., Steinbach, P. A. & Tsien, R. Y. A guide to choosing fluorescent proteins. *Nat Methods* **2**, 905–9 (2005).

59. Panoskaltsis-Mortari, A. *et al.* In vivo imaging of graft-versus-host-disease in mice. *Blood* **103**, 3590–8 (2004).

60. Yamazaki, T. *et al.* Real-time in vivo cellular imaging of graft-versus-host disease and its reaction to immunomodulatory reagents. *Immunol Lett* **144**, 33–40 (2012).

61. Yamauchi, K. *et al.* Induction of cancer metastasis by cyclophosphamide pretreatment of host mice: an opposite effect of chemotherapy. *Cancer Res* **68**, 516–20 (2008).

62. Yang, M. *et al.* Dual-color fluorescence imaging distinguishes tumor cells from induced host angiogenic vessels and stromal cells. *Proc Natl Acad Sci U S A* **100**, 14259–62 (2003).

63. Katz, M. H. *et al.* A novel red fluorescent protein orthotopic pancreatic cancer model for the preclinical evaluation of chemotherapeutics. *J Surg Res* **113**, 151–160 (2003).

64. Verreault, M. *et al.* Development of glioblastoma cell lines expressing red fluorescence for non-invasive live imaging of intracranial tumors. *Anticancer Res* **31**, 2161–71 (2011).

65. Pardo, A. *et al.* In vivo imaging of immunotoxin treatment using Katushka-transfected A-431 cells in a murine xenograft tumour model. *Cancer Immunol Immunother* (2012).

66. Yang, M. *et al.* Whole-body optical imaging of green fluorescent protein-expressing tumors and metastases. *Proc Natl Acad Sci U S A* **97**, 1206–11 (2000).

67. Yang, M., Baranov, E., Moossa, a R., Penman, S. & Hoffman, R. M. Visualizing gene expression by whole-body fluorescence imaging. *Proc Natl Acad Sci U S A* **97**, 12278–82 (2000).

68. Hojman, P., Eriksen, J. & Gehl, J. In vivo imaging of far-red fluorescent proteins after DNA electrotransfer to muscle tissue. *Biol Proced Online* **11**, 253–62 (2009).

69. Gothelf, A., Eriksen, J., Hojman, P. & Gehl, J. Duration and level of transgene expression after gene electrotransfer to skin in mice. *Gene Ther* **17**, 839–45 (2010).

70. Helmchen, F. & Denk, W. Deep tissue two-photon microscopy. *Nat Methods* **2**, 932–40 (2005).

71. Denk, W., Strickler, J. H. & Webb, W. W. Two-photon laser scanning fluorescence microscopy. *Science* **6**, 73–6 (1990).

72. Goeppert-Mayer, M. Elementarakte mit zwei Quantensprüngen (On elementary processes with two quantum steps). *Ann Phys* **9**, 273–294 (1931).

73. Fife, B. T. *et al.* Interactions between PD-1 and PD-L1 promote tolerance by blocking the TCR-induced stop signal. *Nat Immunol* **10**, 1185–92 (2009).

74. Cahalan, M. D., Parker, I., Wei, S. H. & Miller, M. J. Real-time imaging of lymphocytes in vivo. *Curr Opin Immunol* **15**, 372–7 (2003).

75. Miller, M. J., Wei, S. H., Parker, I. & Cahalan, M. D. Two-photon imaging of lymphocyte motility and antigen response in intact lymph node. *Science* **296**, 1869–73 (2002).

76. Bousso, P. & Robey, E. A. Dynamic behavior of T cells and thymocytes in lymphoid organs as revealed by two-photon microscopy. *Immunity* **21**, 349–55 (2004).

77. Stoll, S., Delon, J., Brotz, T. M. & Germain, R. N. Dynamic imaging of T cell-dendritic cell interactions in lymph nodes. *Science* **296**, 1873–6 (2002).

78. Molitoris, B. A. & Sandoval, R. M. Intravital multiphoton microscopy of dynamic renal processes. *Am J Physiol Renal Physiol* **288**, F1084–9 (2005).

79. Camirand, G. *et al.* Multiphoton intravital microscopy of the transplanted mouse kidney. *Am J Transplant* **11**, 2067–74 (2011).

80. Rubart, M. Two-photon microscopy of cells and tissue. *Circ Res* **95**, 1154–66 (2004).

81. Scherschel, J. A. & Rubart, M. Cardiovascular imaging using two-photon microscopy. *Microsc Microanal* **14**, 492–506 (2008).

82. Skoch, J., Hickey, G. A., Kajdasz, S. T., Hyman, B. T. & Bacskai, B. J. In vivo imaging of amyloid-beta deposits in mouse brain with multiphoton microscopy. *Methods Mol Biol* **299**, 349–63 (2005).

83.     Fumagalli, S. *et al.* In vivo real-time multiphoton imaging of T lymphocytes in the mouse brain after experimental stroke. *Stroke* **42**, 1429–36 (2011).

84.     Theer, P., Hasan, M. T. & Denk, W. Two-photon imaging to a depth of 1000 microm in living brains by use of a Ti:Al2O3 regenerative amplifier. *Opt Lett* **28**, 1022–4 (2003).

85.     Wang, B.-G., König, K. & Halbhuber, K.-J. Two-photon microscopy of deep intravital tissues and its merits in clinical research. *J Microsc* **238**, 1–20 (2010).

86.     Jain, R. K., Munn, L. L. & Fukumura, D. Dissecting tumour pathophysiology using intravital microscopy. *Nat Rev Cancer* **2**, 266–76 (2002).

87.     McKenna, R. W. *et al.* Plasma cell neoplasms. *WHO classification of tumours of haematopoietic and lymphoid tissues* (2008).

88.     Howlander, N. *et al. SEER cancer statistics review, 1975-2009 (Vintage 2009 Populations)*. (National Cancer Institute: Bethesda, MD, http://seer.cancer.gov/csr/1975_2009_pops09/, based on November 2011 SEER data submission, posted to the SEER web site, April 2012, ).

89.     Siegel, R., Naishadham, D. & Jemal, A. Cancer Statistics, 2012. *CA Cancer J Clin* **62**, 10–29 (2012).

90.     Ferlay, J., Parkin, D. M. & Steliarova-Foucher, E. Estimates of cancer incidence and mortality in Europe in 2008. *Eur J Cancer* **46**, 765–81 (2010).

91.     Clark, M. R., Cooper, A. B., Wang, L. D. & Aifantis, I. The pre-B cell receptor in B cell development: recent advances, persistent questions and conserved mechanisms. *Curr Top Microbiol Immunol* **290**, 87–103 (2005).

92.     Fairfax, K. A., Kallies, A., Nutt, S. L. & Tarlinton, D. M. Plasma cell development: from B-cell subsets to long-term survival niches. *Semin Immunol* **20**, 49–58 (2008).

93.     Shapiro-Shelef, M. & Calame, K. Regulation of plasma-cell development. *Nat Rev Immunol* **5**, 230–42 (2005).

94.     Anderson, K. C. & Carrasco, R. D. Pathogenesis of myeloma. *Annu Rev Pathol* **6**, 249–74 (2011).

95.     McHeyzer-Williams, L. J., Driver, D. J. & McHeyzer-Williams, M. G. Germinal center reaction. *Curr Opin Hematol* **8**, 52–9 (2001).

96.     Laubach, J., Richardson, P. G. & Anderson, K. C. Multiple myeloma. *Annu Rev Med* **62**, 249–64 (2011).

97.     Sze, D. M., Toellner, K. M., García de Vinuesa, C., Taylor, D. R. & MacLennan, I. C. Intrinsic constraint on plasmablast growth and extrinsic limits of plasma cell survival. *J Exp Med* **192**, 813–21 (2000).

98.     Kuehl, W. M. & Bergsagel, P. L. Multiple myeloma: evolving genetic events and host interactions. *Nat Rev Cancer* **2**, 175–87 (2002).

99.     Sahota, S. S., Leo, R., Hamblin, T. J. & Stevenson, F. K. Myeloma VL and VH gene sequences reveal a complementary imprint of antigen selection in tumor cells. *Blood* **89**, 219–26 (1997).

100. Fonseca, R. *et al.* Genetics and cytogenetics of multiple myeloma: a workshop report. *Cancer Res* **64**, 1546–58 (2004).

101. Bergsagel, P. L. & Kuehl, W. M. Chromosome translocations in multiple myeloma. *Oncogene* **20**, 5611–22 (2001).

102. Bergsagel, P. L. *et al.* Promiscuous translocations into immunoglobulin heavy chain switch regions in multiple myeloma. *Proc Natl Acad Sci U S A* **93**, 13931–6 (1996).

103. Gabrea, A., Bergsagel, P. L. & Kuehl, W. M. Distinguishing primary and secondary translocations in multiple myeloma. *DNA Repair* **5**, 1225–33 (2006).

104. Landgren, O. *et al.* Monoclonal gammopathy of undetermined significance (MGUS) consistently precedes multiple myeloma: a prospective study. *Blood* **113**, 5412–7 (2009).

105. Kyle, R. A. *et al.* Prevalence of monoclonal gammopathy of undetermined significance. *N Engl J Med* **354**, 1362–9 (2006).

106. Bird, J. M. *et al.* Guidelines for the diagnosis and management of multiple myeloma 2011. *Br J Haematol* **154**, 32–75 (2011).

107. Kyle, R. A. & Greipp, P. R. Smoldering multiple myeloma. *N Engl J Med* **302**, 1347–9 (1980).

108. Rajkumar, S. V. Preventive strategies in monoclonal gammopathy of undetermined significance and smoldering multiple myeloma. *Am J Hematol* **87**, 453–4 (2012).

109. Landgren, O. & Waxman, A. J. Multiple myeloma precursor disease. *JAMA* **304**, 2397–404 (2010).

110. López-Corral, L. *et al.* The progression from MGUS to smoldering myeloma and eventually to multiple myeloma involves a clonal expansion of genetically abnormal plasma cells. *Clin Cancer Res* **17**, 1692–700 (2011).

111. Bezieau, S. *et al.* High incidence of N and K-Ras activating mutations in multiple myeloma and primary plasma cell leukemia at diagnosis. *Hum Mutat* **18**, 212–24 (2001).

112. Rundles, R. W., Dillon, M. L. & Dillon, E. S. Multiple myeloma. III. Effect of urethane therapy on plasma cell growth, abnormal serum protein components and Bence Jones proteinuria. *J Clin Invest* **29**, 1243–60 (1950).

113. Weder, C. Urethane in multiple myeloma. *Cand Med Assoc J* **62**, 589–90 (1950).

114. Holland, J. F. *et al.* A controlled trial of urethane treatment in multiple myeloma. *Blood* **27**, 328–42 (1966).

115. Bergsagel, D. E., Sprague, C. C., Austin, C. & Griffith, K. M. Evaluation of new chemotherapeutic agents in the treatment of multiple myeloma. IV. L-Phenylalanine mustard (NSC-8806). *Cancer Chemother Rep* **21**, 87–99 (1962).

116. Hoogstraten, B. *et al.* Melphalan in multiple myeloma. *Blood* **30**, 74–83 (1967).

117. Korst, D. R. *et al.* Multiple myeloma. II. Analysis of cyclophosphamide therapy in 165 patients. *JAMA* **189**, 758–62 (1964).

118. Tourtellotte, C. R. & Call, M. K. Prolonged remission of myeloma with cyclophosphamide. *Arch Intern Med* **113**, 758–63 (1964).

119. Mass, R. E. A comparison of the effect of prednisone and a placebo in the treatment of multiple myeloma. *Cancer Chemother Rep* **16**, 257–9 (1962).

120. Alexanian, R., Dimopoulos, M. A., Delasalle, K. & Barlogie, B. Primary dexamethasone treatment of multiple myeloma. *Blood* **80**, 887–90 (1992).

121. Laubach, J. P., Richardson, P. G. & Anderson, K. C. The evolution and impact of therapy in multiple myeloma. *Med Oncol* **27**, 1–6 (2010).

122. Alexanian, R. *et al.* Treatment for multiple myeloma. Combination chemotherapy with different melphalan dose regimens. *JAMA* **208**, 1680–5 (1969).

123. Lee, B. J., Sahakian, G., Clarkson, B. D. & Krakoff, I. H. Proceedings: Combination chemotherapy of multiple myeloma with alkeran, cytoxan, vincristine, prednisone, and BCNU. *Cancer* **33**, 533–8 (1974).

124. Cooper, M. R. *et al.* Single, sequential, and multiple alkylating agent therapy for multiple myeloma: a CALGB Study. *J Clin Oncol* **4**, 1331–9 (1986).

125. Samson, D. *et al.* Infusion of vincristine and doxorubicin with oral dexamethasone as first-line therapy for multiple myeloma. *Lancet* **2**, 882–5 (1989).

126. Bladé, J. *et al.* Increased conventional chemotherapy does not improve survival in multiple myeloma: long-term results of two PETHEMA trials including 914 patients. *Hematol J* **2**, 272–8 (2001).

127. McElwain, T. J. & Powles, R. L. High-dose intravenous melphalan for plasma-cell leukaemia and myeloma. *Lancet* **2**, 822–4 (1983).

128. Barlogie, B., Hall, R., Zander, A., Dicke, K. & Alexanian, R. High-dose melphalan with autologous bone marrow transplantation for multiple myeloma. *Blood* **67**, 1298–301 (1986).

129. Attal, M. *et al.* A prospective, randomized trial of autologous bonemarrow transplantation and chemotherapy in multiple myeloma. Intergroupe Francais du Myélome. *N Engl J Med* **335**, 91–7 (1996).

130. Child, J. A. *et al.* High-dose cheotherapy with hematopoietic stem-cell rescue for multiple myeloma. *N Engl J Med* **348**, 1875–83 (2003).

131. Attal, M. *et al.* Single versus double autologous stem-cell transplantation for multiple myeloma. *N Engl J Med* **349**, 2495–502 (2003).

132. Salmon, S. E. *et al.* Interferon versus interferon plus prednisone remission maintenance therapy for multiple myeloma: a Southwest Oncology Group Study. *J Clin Oncol* **16**, 890–6 (1998).

133. Barlogie, B. *et al.* Incorporating bortezomib into upfront treatment for multiple myeloma: early results of total therapy 3. *Br J Haematol* **138**, 176–85 (2007).

134. Björkstrand, B. B. *et al.* Allogeneic bone marrow transplantation versus autologous stem cell transplantation in multiple myeloma: a retrospective case-matched study from the European Group for Blood and Marrow Transplantation. *Blood* **88**, 4711–8 (1996).

135. Maloney, D. G. *et al.* Allografting with nonmyeloablative conditioning following cytoreductive autografts for the treatment of patients with multiple myeloma. *Blood* **102**, 3447–54 (2003).

136. Ludwig, H. *et al.* Multiple myeloma treatment strategies with novel agents in 2011: a European perspective. *Oncologist* **16**, 388–403 (2011).

137. Rosiñol, L. *et al.* A prospective PETHEMA study of tandem autologous transplantation versus autograft followed by reduced-intensity conditioning allogeneic transplantation in newly diagnosed multiple myeloma. *Blood* **112**, 3591–3 (2008).

138. Bruno, B. *et al.* Nonmyeloablative allografting for newly diagnosed multiple myeloma: the experience of the Gruppo Italiano Trapianti di Midollo. *Blood* **113**, 3375–82 (2009).

139. Rotta, M. *et al.* Long-term outcome of patients with multiple myeloma after autologous hematopoietic cell transplantation and nonmyeloablative allografting. *Blood* **113**, 3383–91 (2009).

140. Kumar, S. K. *et al.* Improved survival in multiple myeloma and the impact of novel therapies. *Blood* **111**, 2516–20 (2008).

141. Richardson, P., Hideshima, T. & Anderson, K. C. Thalidomide: emerging role in cancer medicine. *Annu Rev Med* **53**, 629–57 (2002).

142. Quach, H. *et al.* Mechanism of action of immunomodulatory drugs (IMiDS) in multiple myeloma. *Leukemia* **24**, 22–32 (2010).

143. Ria, R. *et al.* Bone marrow angiogenesis and progression in multiple myeloma. *Am J Blood Res* **1**, 76–89 (2011).

144. Barlogie, B. *et al.* Extended survival in advanced and refractory multiple myeloma after single-agent thalidomide: identification of prognostic factors in a phase 2 study of 169 patients. *Blood* **98**, 492–4 (2001).

145. Van Rhee, F. *et al.* First thalidomide clinical trial in multiple myeloma: a decade. *Blood* **112**, 1035–8 (2008).

146. Rajkumar, S. V. *et al.* Combination therapy with thalidomide plus dexamethasone for newly diagnosed myeloma. *J Clin Oncol* **20**, 4319–23 (2002).

147. Weber, D., Rankin, K., Gavino, M., Delasalle, K. & Alexanian, R. Thalidomide alone or with dexamethasone for previously untreated multiple myeloma. *J Clin Oncol* **21**, 16–9 (2003).

148. Hideshima, T. *et al.* Thalidomide and its analogs overcome drug resistance of human multiple myeloma cells to conventional therapy. *Blood* **96**, 2943–50 (2000).

149. Dimopoulos, M. A. *et al.* Thalidomide and dexamethasone combination for refractory multiple myeloma. *Ann Oncol* **12**, 991–5 (2001).

150. Dimopoulos, M. *et al.* Lenalidomide plus dexamethasone for relapsed or refractory multiple myeloma. *N* **357**, 2123–32 (2007).

151. Weber, D. M. *et al.* Lenalidomide plus dexamethasone for relapsed multiple myeloma in North America. *N Engl J Med* **357**, 2133–42 (2007).

152. Kisselev, A. F. & Goldberg, A. L. Proteasome inhibitors: from research tools to drug candidates. *Chem Biol* **8**, 739–58 (2001).

153. Adams, J. *et al.* Proteasome inhibitors : a novel class of potent and effective antitumor agents. *Cancer Res* **59**, 2615–22 (1999).

154. Hideshima, T. *et al.* The proteasome inhibitor PS-341 inhibits growth , induces apoptosis , and overcomes drug resistance in human multiple myeloma cells. *Cancer Res* **61**, 3071–6 (2001).

155. LeBlanc, R. *et al.* Proteasome inhibitor PS-341 inhibits human myeloma cell growth in vivo and prolongs survival in a murine model. *Cancer Res* **62**, 4996–5000 (2002).

156. Orlowski, R. Z. *et al.* Phase I trial of the proteasome inhibitor PS-341 in patients with refractory hematologic malignancies. *J Clin Oncol* **20**, 4420–7 (2002).

157. Richardson, P. G. *et al.* A phase 2 study of rortezomib in relapsed, refractory ryeloma. *N Engl J Med* **348**, 2609–17 (2003).

158. Kropff, M. *et al.* DSMM XI study: dose definition for intravenous cyclophosphamide in combination with bortezomib/dexamethasone for remission induction in patients with newly diagnosed myeloma. *Ann Hematol* **88**, 1125–30 (2009).

159. Moreau, P. *et al.* Proteasome inhibitors in multiple myeloma: ten years later. *Blood* **May 29**, Epub ahead of print (2012).

160. Hideshima, T. & Anderson, K. C. Novel therapies in MM: from the aspect of preclinical studies. *Int J Hematol* **94**, 344–54 (2011).

161. Richardson, P., Hideshima, T. & Anderson, K. C. An update of novel therapeutic approaches for multiple myeloma. *Curr Treat Options Oncol* **5**, 227–38 (2004).

162. Anderson, K. C. New insights into therapeutic targets in myeloma. *Hematology Am Soc Hematol Educ Program* **2011**, 184–90 (2011).

163. Kyoizumi, S. *et al.* Implantation and maintenance of functional human bone marrow in SCID-hu mice. *Blood* **79**, 1704–11 (1992).

164. Yaccoby, S., Barlogie, B. & Epstein, J. Primary myeloma cells growing in SCID-hu mice: a model for studying the biology and treatment of myeloma and its manifestations. *Blood* **92**, 2908–13 (1998).

165. Yata, K. & Yaccoby, S. The SCID-rab model: a novel in vivo system for primary human myeloma demonstrating growth of CD138-expressing malignant cells. *Leukemia* **18**, 1891–7 (2004).

166. Groen, R. W. J. *et al.* Reconstructing the human hematopoietic niche in immune deficient mice, opportunities for studying primary multiple myeloma. *Blood* **May 31**, Epub ahead of print (2012).

167. Rozemuller, H. *et al.* A bioluminescence imaging based in vivo model for preclinical testing of novel cellular immunotherapy strategies to improve the graft-versus-myeloma effect. *Haematologica* **93**, 1049–57 (2008).

168. Freeman, L. M. *et al.* Myeloma-Induced Alloreactive T Cells Arising in Myeloma-Infiltrated Bones Include Double-Positive CD8+CD4+ T Cells: Evidence from Myeloma-Bearing Mouse Model. *J Immunol* **187**, 3987–96 (2011).

169. Radl, J., De Glopper, E., Schuit, H. R. & Zurcher, C. Idiopathic paraproteinemia. II. Transplantation of the paraprotein-producing clone from old to young C57BL/KaLwRij mice. *J Immunol* **122**, 609–13 (1979).

170. Radl, J., Croese, J. W., Zurcher, C., Van den Enden-Vieveen, M. H. & De Leeuw, A. M. Animal model of human disease. Multiple myeloma. *Am J Pathol* **132**, 593–7 (1988).

171. Asosingh, K., Radl, J., Van Riet, I., Van Camp, B. & Vanderkerken, K. The 5TMM series: a useful in vivo mouse model of human multiple myeloma. *Hematol J* **1**, 351–6 (2000).

172. Vanderkerken, K. *et al.* Organ involvement and phenotypic adhesion profile of 5T2 and 5T33 myeloma cells in the C57BL/KaLwRij mouse. *Br J Cancer* **76**, 451–60 (1997).

173. Fowler, J. A., Mundy, G. R., Lwin, S. T., Lynch, C. C. & Edwards, C. M. A murine model of myeloma that allows genetic manipulation of the host microenvironment. *Dis Model Mech* **2**, 604–11 (2009).

174. Menu, E. *et al.* Myeloma cells (5TMM) and their interactions with the marrow microenvironment. *Blood Cells Mol Dis* **33**, 111–9 (2004).

175. Vanderkerken, K. *et al.* Selective initial in vivo homing pattern of 5T2 multiple myeloma cells in the C57BL/KalwRij mouse. *Br J Cancer* **82**, 953–9 (2000).

176. Deleu, S. *et al.* The effects of JNJ-26481585 , a novel hydroxamate-based histone deacetylase inhibitor , on the development of multiple myeloma in the 5T2MM and 5T33MM murine models. *Leukemia* **23**, 1894–1903 (2009).

177. Dairaghi, D. J. *et al.* CCR1 blockade reduces tumor burden and osteolysis in vivo in a mouse model of myeloma bone disease. *Blood* **May 22**, Epub ahead of print (2012).

178. Deleu, S. *et al.* Bortezomib alone or in combination with the histone deacetylase inhibitor JNJ-26481585: effect on myeloma bone disease in the 5T2MM murine model of myeloma. *Cancer Res* **69**, 5307–11 (2009).

179. Van Valckenborgh, E. *et al.* Tumor-initiating capacity of CD138- and CD138+ tumor cells in the 5T33 multiple myeloma model. *Leukemia* **26**, 1436–9 (2012).

180. Oyajobi, B. O. *et al.* Detection of myeloma in skeleton of mice by whole-body optical fluorescence imaging. *Mol Cancer Ther* **6**, 1701–8 (2007).

181. Murillo, O. *et al.* Therapeutic antitumor efficacy of anti-CD137 agonistic monoclonal antibody in mouse models of myeloma. *Clin Cancer Res* **14**, 6895–906 (2008).

182. Vanderkerken, K. *et al.* The 5T2MM murine model of multiple myeloma: maintenance and analysis. *Methods Mol Med* 191–205 (2005).

183. Eisen, H. N., Simms, E. S. & Potter, M. Mouse myeloma proteins with antihapten antibody acitivity. The protein produced by plasma cell tumor MOPC-315. *Biochemistry* **7**, 4126–34 (1968).

184. Mokyr, M. B., Place, A. T., Artwohl, J. E. & Valli, V. E. T. Importance of signaling via the IFN-alpha/beta receptor on host cells for the realization of the therapeutic benefits of cyclophosphamide for mice bearing a large MOPC-315 tumor. *Cancer Immunol Immunother* **55**, 459–68 (2006).

185. Hengst, J. C. D., Mokyr, M. B. & Dray, S. Importance of timing in Cyclophosphamide therapy of MOPC-315 tumor-bearing mice. *Cancer Res* **40**, 2135–2141 (1980).

186. Jovasevic, V. M., Gorelik, L., Bluestone, J. A. & Mokyr, M. B. Importance of IL-10 for CTLA-4-mediated inhibition of tumor-eradicating immunity. *J Immunol* **172**, 1449–54 (2004).

187. Mittelman, M., Neumann, D., Peled, A., Kanter, P. & Haran-Ghera, N. Erythropoietin induces tumor regression and antitumor immune responses in murine myeloma models. *Proc Natl Acad Sci U S A* **98**, 5181–6 (2001).

188. Bogen, B. Peripheral T cell tolerance as a tumor escape mechanism: deletion of CD4+ T cells specific for a monoclonal immunoglobulin idiotype secreted by a plasmacytoma. *Eur J Immunol* **26**, 2671–9 (1996).

189. Rohrer, J. W. & Lynch, R. G. Immunoregulation of localized and disseminated murine myeloma: Antigen-specific regulation of MOPC-315 stem cell proliferation and secretory cell differentiation. *J Immunol* **123**, 1083–7 (1979).

190. Valeriote, F., Lynch, R., Berger, N. A., White, E. & Coulter, D. Growth characteristics of MOPC-315 plasmacytoma and response to anticancer agents. *J Natl Cancer Inst* **66**, 1083–8 (1981).

191. Chesi, M. *et al.* AID-dependent activation of a MYC transgene induces multiple myeloma in a conditional mouse model of post-germinal center malignancies. *Cancer Cell* **13**, 167–80 (2008).

192. Chesi, M. *et al.* Drug response in a genetically engineered mouse model of multiple myeloma is predictive of clinical efficacy. *Blood* **120**, 376–385 (2012).

193. Kuehl, W. M. Modeling multiple myeloma by AID-dependent conditional activation of MYC. *Cancer Cell* **13**, 85–7 (2008).

194. Carrasco, D. R. *et al.* The differentiation and stress response factor XBP-1 drives multiple myeloma pathogenesis. *Cancer Cell* **11**, 349–60 (2007).

195. Chiarle, R. *et al.* NPM-ALK transgenic mice spontaneously develop T-cell lymphomas and plasma cell tumors. *Blood* **101**, 1919–27 (2003).

196. Silva, S., Kovalchuk, A. L., Kim, J. S., Klein, G. & Janz, S. BCL2 accelerates inflammation-induced BALB/c plasmacytomas and promotes novel tumors with coexisting T(12;15) and T(6;15) translocations. *Cancer Res* **63**, 8656–63 (2003).

197. Takizawa, M. *et al.* AID expression levels determine the extent of cMyc oncogenic translocations and the incidence of B cell tumor development. *J Exp Med* **205**, 1949–57 (2008).

198. Linden, M., Kirchhof, N., Carlson, C. & Van Ness, B. Targeted overexpression of Bcl-XL in B-lymphoid cells results in lymphoproliferative disease and plasma cell malignancies. *Blood* **103**, 2779–86 (2004).

199. Rutsch, S. *et al.* IL-6 and MYC collaborate in plasma cell tumor formation in mice. *Blood* **115**, 1746–54 (2010).

200. Rosenbaum, H. *et al.* An E mu-v-abl transgene elicits plasmacytomas in concert with an activated myc gene. *EMBO* **9**, 897–905 (1990).

201. Park, S. S. *et al.* Insertion of c-Myc into Igh induces B-cell and plasma-cell neoplasms in mice. *Cancer Res* **65**, 1306–15 (2005).

202. Truffinet, V. *et al.* The 3' IgH locus control region is sufficient to deregulate a c-myc transgene and promote mature B cell malignancies with a predominant Burkitt-like phenotype. *J Immunol* **179**, 6033–42 (2007).

203. Gladden, A. B., Woolery, R., Aggarwal, P., Wasik, M. A. & Diehl, J. A. Expression of constitutively nuclear cyclin D1 in murine lymphocytes induces B-cell lymphoma. *Oncogene* **25**, 998–1007 (2006).

204. Cheung, W. C. *et al.* Novel targeted deregulation of c-Myc cooperates with Bcl-X L to cause plasma cell neoplasms in mice. *J Clin Invest* **113**, 1763–73 (2004).

205. Boylan, K. L. M. *et al.* A transgenic mouse model of plasma cell malignancy shows phenotypic, cytogenetic, and gene expression heterogeneity similar to human multiple myeloma. *Cancer Res* **67**, 4069–78 (2007).

206. Takizawa, M. *et al.* Genetic reporter system for oncogenic Igh-Myc translocations in mice. *Oncogene* **29**, 4113–20 (2010).

207. Lois, C., Hong, E. J., Pease, S., Brown, E. J. & Baltimore, D. Germline transmission and tissue-specific expression of transgenes delivered by lentiviral vectors. *Science* **295**, 868–72 (2002).

208. Dull, T. *et al.* A third-generation lentivirus vector with a conditional packaging system. *J Virol* **72**, 8463–71 (1998).

209. Lauritzsen, G. F. & Bogen, B. The role of idiotype-specific, CD4+ T cells in tumor resistance against major histocompatibility complex class II molecule negative plasmacytoma cells. *Cell Immunol* **148**, 177–88 (1993).

210. Jodal, H. C., Hofgaard, P. O., Dembic, Z. & Bogen, B. A new mouse model for multiple myeloma. *Scand J Immunol* **73**, 346–398 (2011).

211. Hofgaard, P. O. *et al.* A Novel Mouse Model for Multiple Myeloma (MOPC315.BM) That Allows Noninvasive Spatiotemporal Detection of Osteolytic Disease. *PLOS ONE* **7**, e51892 (2012).

212. Kingston, R., Chen, C. & Okayama, H. Calcium phosphate transfection. *Curr Protoc Immunol* Unit 10.13 (2001).

213. Ramezani, A. & Hawley, R. G. Generation of HIV-1-based lentiviral vector. *Curr Protoc Mol Biol* **Chapter 16**, Unit 16.22 (2002).

214. Ramezani, A. & Hawley, R. G. Overview of the HIV-1 lentiviral vector system. *Curr Protoc Mol Biol* **Chapter 16**, Unit 16.21 (2002).

215. Mombaerts, P. *et al.* RAG-1-deficient mice have no mature B and T lymphocytes. *Cell* **68**, 869–77 (1992).

216. Jenkinson, E. J., Van Ewijik, W. & Owen, J. J. Major histocompatibility complex antigen expression on the epithelium of the developing thymus in normal and nude mice. *J Exp Med* **153**, 280–292 (1981).

217. Shultz, L. D. *et al.* Human lymphoid and myeloid cell development in NOD/LtSz-scid IL2R gamma null mice engrafted with mobilized human hemopoietic stem cells. *J Immunol* **174**, 6477–89 (2005).

218. Olson, J. A., Zeiser, R., Beilhack, A., Goldman, J. J. & Negrin, R. S. Tissue-specific homing and expansion of donor NK cells in allogeneic bone marrow transplantation. *J Immunol* **183**, 3219–28 (2009).

219. Friedl, P., Wolf, K., Von Andrian, U. H. & Harms, G. Biological second and third harmonic generation microscopy. *Curr Protoc Cell Biol* **Chapter 4**, Unit 4.15 (2007).

220. Herzenberg, L. A., Tung, J., Moore, W. A., Herzenberg, L. A. & Parks, D. R. Interpreting flow cytometry data: a guide for the perplexed. *Nat Immunol* **7**, 681–5 (2006).

221. Ferguson, A. R. & Engelhard, V. H. CD8 T cells activated in distinct lymphoid organs differentially express adhesion proteins and coexpress multiple chemokine receptors. *J Immunol* **184**, 4079–86 (2010).

222. Millar, J. L., Hudspith, B. N., J, M. T. & Phelps, T. A. Effect of high-dose melphalan on marrow and intestinal epithelium in mice pretreated with cyclophosphamide. *Br J Cancer* **38**, 137–42 (1978).

223. Ogawa, M., Bergsagel, D. E. & Mcculloch, E. A. Differential effects of melphalan on mouse myeloma (Adj. PC-5) and hemopoietic stem cells. *Cancer Res* **31**, 2116–19 (1971).

224. Parmo-Cabañas, M. *et al.* Integrin alpha4beta1 involvement in stromal cell-derived factor-1alpha-promoted myeloma cell transendothelial migration and adhesion: role of cAMP and the actin cytoskeleton in adhesion. *Exp Cell Res* **294**, 571–80 (2004).

225. Aggarwal, R., Ghobrial, I. M. & Roodman, G. D. Chemokines in multiple myeloma. *Exp Hematol* **34**, 1289–95 (2006).

226. Van Riet, I., Vanderkerken, K., De Greef, C. & Van Camp, B. Homing behaviour of the malignant cell clone in multiple myeloma. *Med Oncol* **15**, 154–64 (1998).

227. Okada, T., Hawley, R. G., Kodaka, M. & Okuno, H. Significance of VLA-4-VCAM-1 interaction and CD44 for transendothelial invasion in a bone marrow metastatic myeloma model. *Clin Exp Metastasis* **17**, 623–9 (1999).

228. Pellegrino, A. *et al.* CXCR3-binding chemokines in multiple myeloma. *Cancer Lett* **207**, 221–7 (2004).

229. Vande Broek, I. *et al.* Chemokine receptor CCR2 is expressed by human multiple myeloma cells and mediates migration to bone marrow stromal cell-produced monocyte chemotactic proteins MCP-1, -2 and -3. *Br J Cancer* **88**, 855–62 (2003).

230. Selby, P. J. *et al.* Multiple myeloma treated with high dose intravenous melphalan. *Br J Haematol* **66**, 55–62 (1987).

231. Rifai, A. & Mannik, M. Clearance kinetics and fate of mouse IgA immune complexes prepared with monomeric or dimeric IgA. *J Immunol* **130**, 1826–32 (1983).

232. Morell, A., Skvaril, F., Noseda, G. & Brandun, S. Metabolic properties of human IgA subclasses. *Clin Exp Immunol* **12**, 521–528 (1973).

233. Flies, D. B., Sandler, B. J., Sznol, M. & Chen, L. Blockade of the B7-H1/PD-1 pathway for cancer immunotherapy. *Yale J Biol Med* **84**, 409–21 (2011).

234. Hallett, W. H. D., Jing, W., Drobyski, W. R. & Johnson, B. D. Immunosuppressive effects of multiple myeloma are overcome by PD-L1 blockade. *Biol Blood Marrow Transplant* **17**, 1133–45 (2011).

235. Norde, W. J. *et al.* PD-1/PD-L1 interactions contribute to functional T-cell impairment in patients who relapse with cancer after allogeneic stem cell transplantation. *Cancer Res* **71**, 5111–22 (2011).

236. Iwai, Y. *et al.* Involvement of PD-L1 on tumor cells in the escape from host immune system and tumor immunotherapy by PD-L1 blockade. *Proc Natl Acad Sci U S A* **99**, 12293–7 (2002).

237. Benson, D. M. *et al.* The PD-1/PD-L1 axis modulates the natural killer cell versus multiple myeloma effect: a therapeutic target for CT-011, a novel monoclonal anti-PD-1 antibody. *Blood* **116**, 2286–94 (2010).

238. Zou, W. & Chen, L. Inhibitory B7-family molecules in the tumour microenvironment. *Nat Rev Immunol* **8**, 467–77 (2008).

239. Hilderbrand, S. A. & Weissleder, R. Near-infrared fluorescence: application to in vivo molecular imaging. *Curr Opin Chem Biol* **14**, 71–9 (2010).

240. Chudakov, D. M., Matz, M. V, Lukyanov, S. & Lukyanov, K. A. Fluorescent proteins and their applications in imaging living cells and tissues. *Physiol Rev* **90**, 1103–1163 (2010).

241. Hoffman, R. M. The multiple uses of fluorescent proteins to visualize cancer in vivo. *Nat Rev Cancer* **5**, 796–806 (2005).

242. Shaner, N. C., Patterson, G. H. & Davidson, M. W. Advances in fluorescent protein technology. *J Cell Sci* **120**, 4247–60 (2007).

243. Deliolanis, N. C. *et al.* Performance of the red-shifted fluorescent proteins in deep-tissue molecular imaging applications. *J Biomed Opt* **13**, 1–19 (2009).

244. Diéguez-Hurtado, R. *et al.* A Cre-reporter transgenic mouse expressing the far-red fluorescent protein Katushka. *Genesis* **49**, 36–45 (2011).

245. Zinselmeyer, B. H. *et al.* Two-photon microscopy and multidimensional analysis of cell dynamics. *Methods iEnzymol* **461**, 349–78 (2009).

246. Hoffman, R. M. & Yang, M. Whole-body imaging with fluorescent proteins. *Nat Protoc* **1**, 1429–38 (2006).

247. Chen, C., Krohn, J., Bhattacharya, S. & Davies, B. A comparison of exogenous promoter activity at the ROSA26 locus using a ΦiC31 integrase mediated cassette exchange approach in mouse ES cells. *PLOS ONE* **6**, e23376 (2011).

248. Storti, P. *et al.* Hypoxia-inducible factor (hif)-1α suppression in myeloma cells blocks tumoral growth in vivo inhibiting angiogenesis and bone destruction. *Leukemia* **doi: 10.10**, (2013).

249. Azab, A. K. *et al.* CXCR4 inhibitor AMD3100 disrupts the interaction of multiple myeloma cells with the bone marrow microenvironment and enhances their sensitivity to therapy. *Blood* **113**, 4341–51 (2009).

250. Alsayed, Y. *et al.* Mechanisms of regulation of CXCR4/SDF-1 (CXCL12)-dependent migration and homing in multiple myeloma. *Blood* **109**, 2708–17 (2007).

251. Morgan, G. J., Walker, B. A. & Davies, F. E. The genetic architecture of multiple myeloma. *Nat Rev Cancer* **12**, 335–48 (2012).

252. Kuehl, W. M. Mouse models can predict cancer therapy. *Blood* **120**, 238–40 (2012).

253. Karwacz, K., Arce, F., Bricogne, C., Kochan, G. & Escors, D. PD-L1 co-stimulation, ligand-induced down-modulation and anti-tumor immunotherapy. *Oncoimmunology* **1**, 86–88 (2012).

254. Zitvogel, L. & Kroemer, G. Targeting PD-1 / PD-L1 interactions for cancer immunotherapy. *Oncoimmunology* **1**, 1223–25 (2012).

255. Rutella, S. & Locatelli, F. Targeting multiple-myeloma-induced immune dysfunction to improve immunotherapy outcomes. *Clin Dev Immunol* **2012**, (2012).

256. Ghobrial, I. M. Myeloma as a model for the process of metastasis: implications for therapy. *Blood* (2012).

257. Bladé, J. *et al.* Soft-tissue plasmacytomas in multiple myeloma: incidence, mechanisms of extramedullary spread, and treatment approach. *J Clin Oncol* **29**, 3805–12 (2011).

258. Short, K. D. *et al.* Incidence of extramedullary disease in patients with multiple myeloma in the era of novel therapy, and the activity of pomalidomide on extramedullary myeloma. *Leukemia* **25**, 906–8 (2011).

259. Witzig, T. E. *et al.* Peripheral blood B cell labeling indices are a measure of disease activity in patients with monoclonal gammopathies. *J Clin Oncol* **6**, 1041–6 (1988).

260. Barlogie, B., Smith, L. & Alexanian, R. Effective treatment of advanced multiple myeloma refreactory to alkylating agents. *N Engl J Med* **21**, 1353–6 (1984).

261. Hideshima, T. *et al.* The biological sequelae of stromal cell-derived factor-1α in multiple myeloma. *Mol Cancer Ther* **1**, 539–44 (2002).

262. Kahn, J. *et al.* Overexpression of CXCR4 on human CD34+ progenitors increases their proliferation, migration, and NOD/SCID repopulation. *Blood* **103**, 2942–9 (2004).

263. Heimberger, T. *et al.* The heat shock transcription factor 1 as a potential new therapeutic target in multiple myeloma. *Br J Haematol* **160**, 465–476 (2012).

# Abbreviations

| | |
|---|---|
| µl | microliter |
| µm | micrometer |
| 2PM | two-photon microscopy |
| aLN | axillary lymph node |
| ASCT | autologous stem cell transplantation |
| BLI | bioluminescene imaging |
| BM | bone marrow |
| CCR2 | CC chemokine receptor 2 |
| CCR7 | CC chemokine receptor 7 |
| cLN | cervical lymph node |
| CXCR3 | CXC chemokine receptor 3 |
| CXCR4 | CXC chemokine receptor 4 |
| eGFP | enhanced green fluorescent protein |
| d | day |
| ELISA | Enzyme-linked immunosorbent assay |
| em | emission |
| ex | excitation |
| FACS | fluorescence activated cell sorting |
| FLI | fluorescence imaging |
| Fluc | Photinus pyralis (firefly) luciferase |
| FMO | fluorescence minus one |
| FP | fluorescence protein |
| FSC | forward scatter |
| GFP | green fluorescent protein |
| Gluc | Gaussia princeps luciferase |
| GVHD | graft-versus-host disease |
| h | hour |
| i.p. | intraperitoneal |

| | |
|---|---|
| i.v. | intravenous |
| Ig | immunoglobulin |
| IgH | immunoglobulin heavy chain |
| iLN | inguinal lymph node |
| IU | infectious unit |
| kg | kilogram |
| LN | lymph node |
| luc | luciferase |
| MFI | mean fluorescence intensity |
| mg | milligram |
| MGUS | monoclonal gammopathy of undetermined significance |
| min | minute |
| ml | milliliter |
| mLN | mesenteric lymph node |
| MM | multiple myeloma |
| MOSEC | mouse ovarian surface epithelial cells |
| MSC | mesenchymal stem cell |
| NK | natural killer |
| nm | nanometer |
| NOD | non-obese diabetic |
| OS | overall survival |
| PBMC | peripheral blood mononuclear cell |
| PBS | phosphate buffered saline |
| PC | plasma cell |
| PD-1 | programmed death 1 |
| PD-L1 | programmed death ligand 1 |
| PP | Peyer's patch |
| RFP | red fluorescent protein |
| Rluc | Renilla reniformis luciferase |

| | |
|---|---|
| rpm | revolutions per minute |
| s.c. | subcutaneous |
| SCID | severe combined immunodeficiency |
| SD | standard deviation |
| SMM | smoldering myeloma |
| SSC | side scatter |
| tg | transgenic |
| wt | wildtype |

# Curriculum Vitae

## PERSONAL DATA

Name:                        Simone Stefanie Riedel

Date and place of birth:     27.11.1982, Ulm, Germany

Nationality:                 German

## EDUCATION

**Wuerzburg University**
PhD (Dr. rer. nat.)                                          since
Dissertation (Department of Medicine II):                   April 2008
Thesis title: Characterization of the fluorescence protein FP635
for in vivo imaging and establishment of a murine multiple myeloma
model for non-invasive imaging of disease progression and
response to therapy

**Kaiserslautern Technical University**
M.S. (Diplom), Biology                                      June 2007
Thesis (Department of Plant Ecology and Systematics):
"Genetic biodiversity of cyanobacteria from biological soil crusts
in differently grazed areas in a Savannah ecosystem, Namibia"

**Kaiserslautern Technical University**
B.S. (Vordiplom), Biology                                   October 2004

## PUBLICATIONS

**SS Riedel**, A Mottok, C Brede, CA Bäuerlein, AL Jordán Garrote, M Ritz, K Mattenheimer, A Rosenwald, H Einsele, B Bogen, A Beilhack. *Non-invasive imaging provides spatiotemporal information on disease progression and response to therapy in a murine model of multiple myeloma*. PLoS ONE, 2012;7(12):e52398

T Heimberger, M Andrulis, **S Riedel**, T Stühmer, H Schraud, A Beilhack, T Bumm, B Bogen, H Einsele, R Bargou, M Chatterjee. *The heat shock transcription factor 1 as a potential new therapeutic target in multiple myeloma*. British Journal of Haematology, 2012 Dec 18. doi: 10.1111/bjh.12164. [Epub ahead of print]

C Brede, M Friedrich, AL Jordán Garrote, **SS Riedel**, CA Bäuerlein, KG Heinze, T Bopp, S Schulz, A Mottok, C Kiesel, K Mattenheimer, M Ritz, V von Krosigk, A Rosenwald, H Einsele, RS Negrin, GS Harms, A Beilhack. *Mapping immune processes in intact tissues at cellular resolution*. Journal of Clinical Investigation 2012;122(12):4439-46

## ORAL PRESENTATIONS

*In vivo Imaging of Multiple Myeloma using a Syngeneic Mouse Model.* Retreat Clinical Research Unit 216, Wuerzburg, January 2012

*Establishment of a Plasmacytoma Model for in vivo Bioluminescence Imaging.* Retreat Clinical Research Unit 216, Wuerzburg, January 2011

*How T lymphocytes infiltrate target tissues in acute graft-versus-host disease.* 5th International Symposium organized by the students of the GSLS, Wuerzburg, October 2010

*In vivo Imaging of T cell Subpopulations.* Transregio 52 Meeting, Berlin, June 2009

## MEETING ABSTRACTS

A Bäuerlein, **S Riedel**, C Brede, AL Jordan Garrote, M Ritz, M Chopra, R Negrin, H Einsele, A Beilhack. *Distinct Receptor Profile Defines Alloreactive T Cells Before GvHD Onset.* EHA 17th Congress, Amsterdam, Netherlands, June 2012

M Chopra, **S Riedel**, V Raab, S Donat, A Jordan-Garotte, C Bäuerlein, M Ritz, H Einsele, H Wajant, A Beilhack. *Employing in vivo Bioluminescence Imaging for Assessing the Contribution of TNF-TNFR Interactions to Tumour Metastasis in a Syngenic Mouse Model.* 37th Annual Meeting of the European Group for Blood and Marrow Transplantation, Paris, France, April 2011

C Bäuerlein, **S Riedel**, C Brede, AL Jordán Garrote, C Kiesel, M Ritz, S Schulz, M Grether, G Beilhack, R Negrin, H Einsele, A Beilhack. *Differences in Alloreactive T Cell Migration in MHC Matched Versus MHC Mismatched HCT are Caused by Waves of T Cell Expansion.* EHA 15th Congress, Barcelona, Spain, June 2010

**SS Riedel**, M Herold, M Hirschberg, C Brede, CA Baeuerlein, AL Jordán-Garrote, C Kiesel, M Ritz, J Baker, RS Negrin, H Einsele, A Beilhack. *Assessment of the Near-Infrared Fluorescent Protein FP635 for Dynamic in vivo Imaging in Models of Adaptive Immune Responses.* 51st ASH Annual Meeting and Exposition, New Orleans, LA, USA, December 2009

# Affidavit

I hereby confirm that my thesis entitled Characterization of the fluorescence protein FP635 for in vivo imaging and establishment of a murine multiple myeloma model for non-invasive imaging of disease progression and response to therapy is the result of my own work. I did not receive any help or support from commercial consultants. All sources and / or materials applied are listed and specified in the thesis.

Furthermore, I confirm that this thesis has not yet been submitted as part of another examination process neither in identical nor in similar form.


Place, Date                                                                                    Signature


# Eidesstattliche Erklärung

Hiermit erkläre ich an Eides statt, die Dissertation Charakterisierung des Fluoreszenzproteins FP635 für die in vivo Bildgebung und Etablierung eines Maus Modells für die nicht invasive Bildgebung des Krankheitsverlaufes und Ansprechen auf Therapien im Multiplen Myelom eigenständig, d.h. insbesondere selbständig und ohne Hilfe eines kommerziellen Promotionsberaters, angefertigt und keine anderen als die von mir angegebenen Quellen und Hilfsmittel verwendet zu haben.

Ich erkläre außerdem, dass die Dissertation weder in gleicher noch in ähnlicher Form bereits in einem anderen Prüfungsverfahren vorgelegen hat.


Ort, Datum                                                                                     Unterschrift